

## ABSTRACT

Title of Dissertation:      PHONON      MEDIATED      THERMAL  
TRANSPORT   IN   TRANSITION   METAL  
DICHALCOGENIDES

Jie Peng, Doctor of Philosophy, 2020

Dissertation directed by:      Associate Professor, Peter W Chung,  
Department of Mechanical Engineering

Transition metal dichalcogenides (TMDCs) have attracted extensive interests due to outstanding electronic, optical, and mechanical properties, thus are highly promising in nanoelectronic device applications. However, comprehensive understanding of phonon mediated thermal transport in TMDCs is still lacking despite the important roles they play in determining the device performance. The topics requiring further explorations include the full Brillouin zone (BZ) phonons, temperature dependence of thermal properties, and

structural-thermal relations of TMDCs. In determining above phonon transport characteristics, the anharmonic effect plays a central role.

In this thesis, we present studies on the phonon properties of two TMDC materials, namely MoS<sub>2</sub> and HfS<sub>2</sub>. In the first study, effect of folding on the electronic and phonon transport properties of single-layer MoS<sub>2</sub> are investigated. The atomic structure, ground state electronic, and phonon transport properties of folded SLMoS<sub>2</sub> as a function of wrapping length are determined. The folded structure is found to be largely insensitive to the wrapping length. The electronic band gap varies significantly as a function of the wrapping length, while the phonon properties are insensitive to the wrapping length. The possibility of modulating the gap values while keeping the thermal properties unchanged opens up new exciting avenues for further applications of MoS<sub>2</sub>.

In the second study, we show that anharmonic phonon scattering in HfS<sub>2</sub> leads to a structural phase transition. For the first time, we discover the 3R phase above 300 K. In experiments, we observe a change in the first-order temperature coefficients of A<sub>1g</sub> and E<sub>g</sub> mode frequencies, and lattice parameters  $a$  and  $c$  at room temperature. Moreover, an anomalous phonon stiffening of A<sub>1g</sub> mode below 300 K is also observed. The first-principle simulations find a phase transition at 300 K which is characterized by a change in the stacking order from AAA to ABC. The simulations are validated by good agreements with experimental measurements on all the above temperature coefficients. By comparing DFT calculations under harmonic and anharmonic phonon approximation, we attribute the phase change to be due to phonon anharmonicity. The anomalous A<sub>1g</sub> phonon stiffening is due to decrease of the intralayer thickness of the HfS<sub>2</sub> trailayer, as temperature increases.



PHONON MEDIATED THERMAL TRANSPORT IN TRANSITION  
METAL DICHALCOGENIDES

by

Jie Peng

Dissertation submitted to the Faculty of the Graduate School of the  
University of Maryland, College Park, in partial fulfillment  
of the requirements for the degree of  
Doctor of Philosophy

2020

Advisory Committee:

Associate Professor Peter W Chung, Chair

Professor Bao Yang

Professor Abhijit Dasgupta

Professor Patrick McCluskey

Professor Agis Iliadis, Dean's Representative

Dr Sina Najmaei, Special Member Graduate Faculty

© Copyright by

Jie Peng

2020

## **Acknowledgements**

Past five years of my PhD life has been the most important time period in my life so far. It was tough but also rewarding. I have had times when I achieved great accomplishments, but also times when I felt extremely confused and failed to make any progress. But I have made it. I could not have made it without the support from the people around me.

The person that has affected me the most during my life in US, is my advisor, Dr. Peter W Chung. He is an incredible person. He not only helps me to grow into a mature researcher, but also teaches me how to be a self-disciplined individual in life. For every manuscript, he would spend hours and hours commenting on how to revise it, even starting from a terrible draft I gave to him. He teaches me how to be a successful professional in academia on a daily basis. He also gives a lot of freedom to me that helped a lot when I felt I had to slow down for a while to sort everything in my life. Here, I would thank my advisor for his support during my pursuit of the PhD degree.

The faculty members I have met in University of Maryland are all great people. They are nice to students and willing to answer questions I had when I took their courses. As I have worked as TA under couple of professors, they also showed me how a professional managed the balance between one's teaching duty and research work effectively. My thanks to Prof. Abhijit Dasgupta from the Mechanical Engineering department for his support and understanding to release me from some TA works during the time I wrote this thesis. I would like to thank Dr. Sina Najmaei from the Army Research

Lab for his brilliant ideas and suggestions provided, during our collaboration on the  $\text{HfS}_2$  research.

My family and my friends all have been a great source of support for me for the past few years. Living in a foreign country is difficult, both for me and my parents. I am very grateful for their understanding on me that I chose to look for a career thousands of miles away from my home. I have enjoyed the time here with my friends, Hao, Guang, Rujun, Liping, Yao, and so on. My lab mates, Frank, Gaurav, Rose, Eunjeong, and so on, are all excellent persons who I can discuss academic problems with and also share feelings about life with. Sorry I cannot put all your names here. I love you all!

Last, I would gratefully acknowledge ARO support under Award W911NF-14-1-0330, the support from the Center for Engineering Concepts Development and the Department of Mechanical Engineering at the University of Maryland, and the Army Research Laboratory Open Campus Initiative through the Oak Ridge Institute for Science and Education supported by the Computational Sciences Division of the Computational and Information Sciences Directorate and hosted by the RF-Division of the Sensors and Electron Devices Directorate. The supercomputing resources, made available in part from the University of Maryland (<http://hpcc.umd.edu>), are gratefully acknowledged.

# Table of Contents

Acknowledgements .....	ii
Table of Contents .....	iv
List of Tables .....	viii
List of Figures .....	xi
List of Abbreviations .....	xix
Chapter 1 Introduction.....	1
1.1 Literature review .....	1
1.2 Challenges in thermal transport modeling .....	8
1.3 Objectives and outline.....	11
Chapter 2 Theory of phonons and computational approach.....	14
2.1 Theory of phonon.....	14
2.1.1 Harmonic phonon.....	14
2.1.2 Quasi-harmonic phonons .....	19
2.1.3 Anharmonic phonons .....	21
2.2 Computational approaches.....	22
2.2.1 Molecular dynamics.....	24
2.2.2 Density functional theory.....	26
2.2.3 Car-Parrinello Molecular Dynamics .....	29
2.3 Thermal transport calculations.....	33
2.3.1 Phonon dispersion relation.....	33

2.3.2	Phonon relaxation time .....	34
Chapter 3	Phonon and electronic properties of folded single-layer molybdenum disulfide	
	39	
3.1	Introduction.....	40
3.2	Computational details .....	41
3.3	Results and discussion .....	49
3.3.1	Folded structure .....	49
3.3.2	Electronic band structure. ....	54
3.3.3	Thermal conductivity and Phonons. ....	56
3.4	Summary .....	60
Chapter 4	Temperature-dependent phonons in 1T-HfS <sub>2</sub> : a first-principle study under quasi-harmonic approximation .....	62
4.1	Introduction.....	62
4.2	Computational Methods.....	65
4.2.1	DFT calculations .....	65
4.2.2	The Grüneisen parameters .....	66
4.2.3	Thermal expansion coefficients .....	67
4.2.4	Phonon mean free paths, relaxation times, and thermal conductivities	
	68	
4.3	Results and discussion .....	69
4.3.1	Lattice structure of bulk HfS <sub>2</sub> .....	69
4.3.2	Phonons, phonon normal modes, and LO-TO splitting .....	70

4.4	Phonon properties of HfS <sub>2</sub> at 300K .....	78
4.4.1	Group velocity and specific heat.....	78
4.4.2	Grüneisen parameters.....	79
4.4.3	Phonon relaxation time, mean free path, and thermal conductivity .	81
4.4.4	Temperature effect .....	86
4.5	Summary .....	90
Chapter 5	Structural phase change and phonon stiffening in HfS <sub>2</sub> .....	92
5.1	Introduction.....	93
5.2	Experiments .....	94
5.3	Theoretical calculations .....	97
5.3.1	QHA .....	98
5.3.2	CPMD .....	98
5.4	Results and discussion .....	99
5.4.1	Structural phase transition.....	99
5.4.2	Lattice anharmonicity .....	103
5.4.3	Phonon stiffening and bonding length .....	104
5.5	Summary .....	105
Chapter 6	Conclusions and outlook.....	107
6.1	Summary and contributions .....	107
6.2	Future works .....	111
6.2.1	Temperature dependence and anharmonicity of phonons .....	111
6.2.2	Thermal transport in HfS <sub>2</sub> .....	112

6.2.3	Folded MoS <sub>2</sub> and origami nanostructures .....	113
	Bibliography .....	115

## List of Tables

Table 1.1. Summary of studies on TMDCs thermal transport properties. “Exp.” and “Theo.” represent experimental and theoretical studies, respectively. In the “number of layers” column, “ $\infty$ ” represents bulk. In the “thermal conductivity” column, room-temperature values are given if no specification is indicated. We limit our literature search mostly to the past decade in order to examine the most recent development in the research field of TMDCs. Representative works for each kind of experimental or computational method have been collected.....	7
Table 3.1. Electronic band gap (eV) for bulk MoS <sub>2</sub> , bilayer MoS <sub>2</sub> and SLMoS <sub>2</sub> . .....	54
Table 3.2. Specific heat, phonon relaxation time, phonon group velocity, phonon mean free path and thermal conductivities. ....	58
Table 3.3. Thermal conductivity (Wm <sup>-1</sup> K <sup>-1</sup> ) of bulk MoS <sub>2</sub> , bilayer MoS <sub>2</sub> , SLMoS <sub>2</sub> and folded SLMoS <sub>2</sub> . ....	59
Table 4.1. Lattice parameter $a$ and $c$ from experiments, numerical simulations, and this work. $d_{\text{Hf-S}}$ represents the bond length between Hf atom and its nearest neighbor S atom.....	70
Table 4.2. Comparison between $\Gamma$ phonon frequencies calculated in present work and the ones from literature.....	72
Table 4.3. Phonon frequencies calculated from force constants representing the phonon perturbations $[\Phi b\alpha, b' \beta an(\mathbf{q} = 0)]$ and electric field perturbations	

associated with phonons with $\mathbf{q}$ approaching $\Gamma$ from in-plane [ $\Phi b\alpha, b' \beta nan(\mathbf{q}in - \mathbf{plane} \rightarrow 0)$ ] and c-axis [ $\Phi b\alpha, b' \beta nan(\mathbf{q}c -$ $\mathbf{axis} \rightarrow 0)$ ] directions. The frequencies are in unit $\text{cm}^{-1}$ . Visualizations of the phonon modes are shown in the right column where the red arrows indicate the atomic displacements.....	75
Table 4.4. ZO mode frequencies in bulk and SL 2D TMDC materials and <i>RVDW</i> calculated from Eq. (4.9). In the schematic of the ZO mode, the red circles represent the atoms, the blue arrows represent the atomic displacements, the springs represent the effective VDW and in-plane interactions. (We note that the ZO mode frequency of a $3\pm 1$ -layer $\text{ZrS}_2$ sample are taken as the $\omega_{SLZO}$ value here [178]. However, we consider the difference between the $A_{1g}$ frequencies of 3-layer and SL $\text{ZrS}_2$ negligible since the frequency shows weak layer number dependence (going from $331.9 \text{ cm}^{-1}$ for a 3-layer sample to $332.45 \text{ cm}^{-1}$ for a 42-layer sample))......	77
Table 4.5. Calculated Phonon branch (ZA, LA, TA, and optical) contributions to total thermal conductivity of $\text{HfS}_2$ at 300K with analogous literature values for graphene and $\text{SLMoS}_2$ . .....	84
Table 4.6. In-plane and c-axis thermal conductivities of $\text{HfS}_2$ and other 2D materials. The anisotropy ratio $R_{an} = \kappa c - axis / \kappa in - plane$ . The unit for thermal conductivities is $\text{W/m/K}$ . .....	85
Table 4.7. Elastic constants and bulk modulus of $\text{HfS}_2$ . All values are in GPa.....	87

Table 5.1. Temperature coefficients of lattice parameters ( $\alpha_a$  and  $\alpha_c$ ) and phonon frequencies ( $\chi_A$  and  $\chi_E$ ). The frequencies are fitted to a linear equation  $\omega T = \omega_0 + \chi T$  where  $\omega_0$  is the frequency at ground state and  $\chi$  is the temperature coefficient. The lattice parameters are fitted to a linear equation  $g T = g_0(1 + \alpha)T$  where  $g_0$  is the lattice parameter at ground state and  $\alpha$  is the temperature coefficient. The percentage difference between experimental and simulation data, calculated as  $\frac{sim - exp}{exp} \times 100\%$ , are shown in the square. .... 102

## List of Figures

Figure 1.1. (a) Atomic structure of SL TMDCs in trigonal prismatic (2H), distorted octahedral (1T) and dimerized (1T') phases. The arrows denote the unit cell vectors. (b) Electronic band structure of bulk, quadrilayer, bilayer, and SL MoS<sub>2</sub>. The valance band and conduction band are represented by solid blue and red lines, respectively. The arrow indicates the lowest energy transition. With decreasing number of layers, the indirect bandgap in bulk gradually becomes the direct bandgap in SL. (c) Cross section of a WS<sub>2</sub>-based FET. Thin flakes of WS<sub>2</sub> coupled with an ionic liquid dielectric are placed between the gate electrode and substrate. (d) Schematic of SLMoS<sub>2</sub>-based FET. Figures are adapted with permissions from: (a) [20] © 2017 Springer Nature (b) [21] © 2010 American Chemical Society (c) [22] © 2012 American Chemical Society (d) [14] © 2011 Springer Nature. .... 3

Figure 2.1. Schematic for range of length and time scale applicability of different phonon computational approaches (see Ref. [82]).  $\lambda$  is the phonon wavelength,  $\tau c$  is the phonon collision time. The figure is adapted with permission from [82] © 2018 Springer Nature..... 23

Figure 2.2. Flow chart of the MD simulations using the Velocity Verlet algorithm. Here,  $T$  represents the total simulation time. Notice that the velocities are updated after positions, in contrast to the intuitive thinking that one should update atomic velocities first before positions. The latter case will accumulate numerical

errors in the integration scheme by integrating twice. Making use of the cancelation between Taylor expansion terms, the Velocity Verlet algorithm has higher order of accuracy than the integration by Taylor expansion alone. ... 25

Figure 3.1. Dimensions of folded SLMoS<sub>2</sub> for variational mechanics solution. Left figure is the original flat sheet and right figure is of the folded sheet..... 43

Figure 3.2. Strain energy VS curvature of SLMoS<sub>2</sub> nanotube. Open circles represent the strain energy obtained from molecular simulations and the line is the best fit used to estimate bending stiffness. Curvature  $p = 1/R$  where  $R$  is the radius of SLMoS<sub>2</sub> nanotube which is defined as distance from center to middle Mo atomic layer. .... 45

Figure 3.3. The  $10 \times 1 \times 1$  supercell of dual fold SLMoS<sub>2</sub> (wrap length 192.76 Å) in DFT simulations. (a) Side view. (b) Top view. Vacuum layers of >10 nm are used in the lateral directions..... 47

Figure 3.4. Side views of (a) single layer of MoS<sub>2</sub>, (b) two layers of bulk MoS<sub>2</sub>, and (c) Top view along c-axis. The top view for both SL and bulk appear identical. The primitive unit cells are shown in red line boxes. The rectangular unit cell is shown in the black line boxes. .... 50

Figure 3.5. (a) Side view of equilibrium folded SLMoS<sub>2</sub> with  $2L = 192.8$  Å from DFT simulation. (b) Equilibrium configuration of folded SLMoS<sub>2</sub> ( $2L = 235.6$  Å) showing atomic coordinates from variational mechanics, molecular, and DFT methods. (c) Average atomic distance between folded SLMoS<sub>2</sub> nanostructure obtained from MD and DFT as functions of wrap length ( $2L$ ). The distances

are divided by the single layer lattice constant $a_0$ . (d) Equilibrated lengths of flat and folded regions as a function of original sheet length. (e) Strain energy per unit length of fold versus wrap length. ....	51
Figure 3.6. Electronic band structure of (a) Bulk MoS <sub>2</sub> . (b) Bilayer MoS <sub>2</sub> . (c) SLMoS <sub>2</sub> . Conduction bands (Red) and valance bands (Blue) and band gap (solid line arrow) are shown in the figure. The zero of the energy spectrum has been set to the valence band maximum (VBM) which is denoted by the horizontal dashed line. The conduction-band-minimum (CBM) is denoted as $\Sigma$ . ....	54
Figure 3.7. Electronic band structure of folded SLMoS <sub>2</sub> . (a) $2L = 149.9 \text{ \AA}$ . (b) $2L = 192.8 \text{ \AA}$ . (c) $2L = 235.6 \text{ \AA}$ . (d) $2L = 278.4 \text{ \AA}$ . (e) $2L = 310.6 \text{ \AA}$ . The high symmetry direction $\Gamma \rightarrow K$ corresponds to the zigzag direction in real space. ....	55
Figure 3.8. Calculated electronic band gap as a function of wrap length of folded SLMoS <sub>2</sub> . The value for the infinite bilayer is shown as a horizontal line. ....	56
Figure 3.9. Phonon dispersion curves and densities of states of (a) bulk MoS <sub>2</sub> . (b) bilayer MoS <sub>2</sub> . (c) SLMoS <sub>2</sub> . ....	57
Figure 3.10. Phonon dispersion curves and densities of states of folded SLMoS <sub>2</sub> . (a) $2L = 149.94 \text{ \AA}$ . (b) $2L = 192.76 \text{ \AA}$ . (c) $2L = 235.6 \text{ \AA}$ . (d) $2L = 278.44 \text{ \AA}$ . (e) $2L = 310.58 \text{ \AA}$ . ....	58

Figure 3.11. Thermal conductivity of folded SLMoS<sub>2</sub> at T=300 K calculated by Green-

Kubo method. Thermal conductivity of folded SLMoS<sub>2</sub> is considerably smaller than thermal conductivity of SLMoS<sub>2</sub>. ..... 60

Figure 4.1. (a) Top view and (b) side view of the HfS<sub>2</sub> lattice structure. Each HfS<sub>2</sub> unit cell,

represented by the black boxes, consists of one Hf atom and two S atoms. The figures are generated using the XCRYSDEN [168] program. .... 69

Figure 4.2. Phonon dispersion curves and density of states (DOS) of bulk HfS<sub>2</sub> calculated

using the PBE and PBE+VDW DFT models. The experimentally measured A<sub>1g</sub> and E<sub>g</sub> frequencies [52, 174] are marked by star symbols with a cyan color at  $\Gamma$ . DOS calculated by the PBE+VDW model is shown on the right as solid red lines. The high symmetry path  $\Gamma - M - K - \Gamma$  is in the xy plane, while  $\Gamma - A$  is along the c-axis in the reciprocal space. The nine phonon branches are represented by longitudinal acoustic (LA) and optical (LO), transverse acoustic (TA) and optical (TO), and out-of-plane acoustic (ZA) and optical (ZO) symbols. The subscripts “1” and “2” represent R-active and IR-active modes, respectively. The absence of a gap in the phonon spectrum, as shown in the phonon DOS, implies frequent scattering among the acoustic and optical branches and, consequently, a low thermal conductivity of HfS<sub>2</sub>. .... 71

Figure 4.3. (a) Mode-dependent phonon group velocities along ***qx***, ***qy*** and ***qz*** directions.

For the in-plane group velocities,  $v_x \approx v_y$  for almost all the phonon modes, so that the circle (red) dots are nearly all covered by the diamond (blue) dots, whereas the square (black) dots representing  $v_z$  have significantly smaller

values (b) Magnitude of phonon group velocity VS frequency in the full BZ.  
(c) Specific heat VS temperature of HfS<sub>2</sub>. The inset shows the branch-wise phonon specific heats. The acoustic branches have a larger contribution to the total specific heat than the optical branches at low T. As T increases, equipartition is gradually recovered. .... 79

Figure 4.4. Gruneisen parameters (a)  $\gamma a$  (b)  $\gamma c$  (c)  $\gamma V$  along high symmetry paths. (d)  $\gamma V$  of all phonon modes in the BZ as a function of frequency. The volumetric Gruneisen parameter  $\gamma V$  is used for subsequent calculations of RTs..... 81

Figure 4.5. Mode-dependent phonon RTs for ZA, LA, TA, and optical modes (a) along the high symmetry paths (b) in the full BZ and phonon MFPs along (c) x- (d) y- (e) z-directions of HfS<sub>2</sub> at 300K. The dash line represents the lattice parameter  $a$  of HfS<sub>2</sub>. Despite the unrealistically small MFP ( $\approx 10 - 15$  nm) for some optical modes, our results show that most of the optical modes have MFP smaller than the lattice parameter, thus having negligible contribution (<1%) to the total thermal conductivity. Therefore, we replace the MFPs of these modes by the lattice parameter  $a$  for a more reasonable estimate of thermal conductivity. .... 83

Figure 4.6. Mode-dependent thermal conductivities in (a) x-, (b) y-, and (c) z-direction of HfS<sub>2</sub> at 300K. There is no substantial difference among the thermal conductivity distributions along different lattice directions. The thermal conductivity decreases with increasing frequency, suggesting that the largest

contribution towards the total thermal conductivity comes from the lowest frequency ZA modes..... 84

Figure 4.7. (a) TECs along  $a$  and  $c$  directions, lattice parameter (b)  $a$  and (c)  $c$  VS temperature of  $\text{HfS}_2$ . The XRD experiment showed that  $\text{HfS}_2$  decomposes to form  $\text{HfO}_2$  at  $735^\circ\text{C}$  [194], therefore we limited the temperature to 1010K. In order to compare the temperature dependence rather than the absolute values, the experimentally measured lattice parameters have all been subtracted by a constant value which enforces them to agree with results of this work at room temperature. .... 87

Figure 4.8. Temperature-dependent average (a) RT, three-dimensional (b) MFP, and (c) thermal conductivity. (d) Contribution from the ZA branch toward the total thermal conductivity of  $\text{HfS}_2$ . In (c) and (d), the results calculated using Eq. (9) are marked with (v), while the ones from Eq. (10) are marked with (vq,j ). .... 89

Figure 5.1. Measurements on phonon frequencies and lattice parameters of  $\text{HfS}_2$ . The scatters represent experimental data while the dash lines represent the linearly fitted curve. Temperature dependent Raman peaks of (a)  $E_g$  and (b)  $A_{1g}$  modes for  $\text{HfS}_2$  samples with different thickness, in the temperature range [77, 300] K. Approximately linear dependence on temperature is observed. Considering the lattice parameter  $c$  of  $\text{HfS}_2$  is around 0.583-0.88 nm [53, 169], the thinnest sample in the experiments contains over 10 layers. Therefore, all the samples are deemed to be bulk  $\text{HfS}_2$ . XRD measured lattice parameters (c)  $a$  and (d)  $c$

of HfS<sub>2</sub> samples with 300nm thickness. The TEC of lattice parameter  $a$  is calculated as  $\alpha a = d\epsilon a/dt$ . The strain is calculated as  $\epsilon a = aT - a(0)a(0)$  with  $a_0 = 3.622 \text{ \AA}$  (interception of the fitted curve with y axis, which is considered as lattice parameter  $a$  at 0K). The TEC of lattice parameter  $c$  is calculated using the same approach. Temperature dependent Raman peaks of (e) E<sub>g</sub> and (f) A<sub>1g</sub> modes for HfS<sub>2</sub> sample with thickness 300 nm in the temperature range [77 500] K..... 96

Figure 5.2. Equilibrium lattice configurations of HfS<sub>2</sub> supercells at different temperature.

The structural phase transition is characterized by a change in the stacking order between adjacent trilayers, as is denoted by the dash red lines..... 101

Figure 5.3. Temperature dependent (a) in-plane lattice parameter  $a$ , (b) c-axis lattice

parameter  $c$ , (c) A<sub>1g</sub> phonon frequency  $\omega A$ , and (d) E<sub>g</sub> phonon frequency obtained from theoretical calculations and experimental measurements. In all the figures, the simulation data has been subtracted by a constant number to match with experimental data at 120K, in order to compare the temperature dependence rather than absolute values. In (b), the lattice parameter  $c$  of ABC-HfS<sub>2</sub> is obtained by taking one third of the supercell dimension along c-axis, since one supercell contains three unit cells along the c-axis direction. .... 101

Figure 5.4. Temperature dependent intralayer distance  $h$  (vertical distance between S layers

in a trilayer) and interlayer distance  $h_{VDW}$  (vertical distance between adjacent S layers) of HfS<sub>2</sub>. The effective interaction dominating out-of-plane vibrational mode A<sub>1g</sub> is represented by  $CVDW$  and  $Cintra$ , respectively. .... 105

Figure 6.1. Schematics of proposed study on folding along different lattice orientations.

Due to the hexagonal closed pack lattice structure, the angle between wrap axis and armchair orientation can vary between  $0^\circ$  to  $30^\circ$  to create different folds.

..... 113

## List of Abbreviations

AIMD	<i>Ab initio</i> molecular dynamics
AN	anharmonic
BTE	Boltzmann transport equation
CPMD	Car-Parrinello molecular dynamics
CDW	charge density wave
DFPT	density functional perturbation theory
DFT	density functional theory
DOF	degrees of freedom
DOS	densities of states
EOM	equation of motion
FEL	free energy landscape
FET	field effect transistors
GGA	generalized-gradient approximation
PBE	Perdew-Burke-Enzerhof
HA	harmonic approximation
LD	lattice dynamics
LDA	local density approximations
MD	molecular dynamics
MFP	mean free path
NEGF	non-equilibrium Green's function

NEMD	non-equilibrium molecular dynamics
PW91	Perdew and Wang
QHA	quasi-harmonic approximation
RHS	right-hand-side
RT	relaxation time
SE	Schrödinger's Equation
SED	spectral energy density
SL	single-layer
SMRTA	single-mode relaxation time approximation
TEC	thermal expansion coefficient
TMDCs	transition metal dichalcogenides
VDW	van der Waals
NEGF	non-equilibrium Green's function
XRD	X-ray diffraction

# Chapter 1 Introduction

Transition metal dichalcogenides (TMDCs) have attracted overwhelming interests due to their potential applications in next-generation electronic, optoelectronic, and thermoelectric devices [1]. In all these applications, a comprehensive understanding of heat transfer is important as it is related to heat dissipation, energy conversion, and thermal management at a system or device level [2, 3]. In electronic and optoelectronic devices, the heat generation can significantly raise the operating temperature, which limits the device performance or even leads to device failure. Owing to the atomic thickness of two-dimensional (2D) TMDCs, heat dissipation is even more challenging in TMDC-based devices. In thermoelectric devices, on the other hand, low thermal conductivity materials are preferred. This is because the efficiency of thermoelectricity is inversely related to the thermal conductivity. To design devices with desired thermal properties, it is essential to understand thermal transport in TMDCs.

## 1.1 Literature review

The growing interests on TMDCs can be traced back to the wide application of graphene. Ever since the discovery of atomically thin graphene in 2004 [4], the research filed on graphene took off rapidly. With its unique electronic band structure [5], high carrier mobility [6], and superior thermal conductivity [7], graphene is highly promising in the application of electronic devices. However, due to its zero-bandgap or semi-metal nature, field effect transistors (FET) and optoelectronic devices built from graphene exhibit

very small on/off ratio. Various bandgap engineering approaches including nanostructuring [8], hydrogen adsorption [9], and applying high electric field [10] have been proposed to create a sizeable bandgap in graphene. Nevertheless, these approaches add to the device design complexity and often result in a decrease in the mobility. On the contrary, TMDCs such as MoS<sub>2</sub> (1.29 eV) [11], WS<sub>2</sub> (1.35 eV) [12], and HfS<sub>2</sub> (1.2 eV) [13] have finite bandgap and promise to be a better candidate than graphene in electronic devices [14, 15]. Moreover, TMDCs have long been shown to possess a wide range of electronic, thermal, and optical properties [16]. Together with recent developments in sample preparation [17, 18] and device fabrication [19], there has been a resurgent of research interests in TMDCs over the past decade.

TMDCs are a class of materials with formula MX<sub>2</sub>, where M is a transition metal element (Mo, Hf, Ti, Zr and so on) and X is a chalcogen element (S, Se and so on). They share common layered structures where one layer of M atoms is sandwiched by two layers of X atoms, as shown in Figure 1.1(a). Known structures of TMDCs are characterized by trigonal prismatic (2H), octahedral (1T), or dermized 1T (1T') coordination of the metal atom. The in-plane atoms are connected by strong covalent bonds while adjacent layers are held together by weak interlayer van der Waals (VDW) interactions.

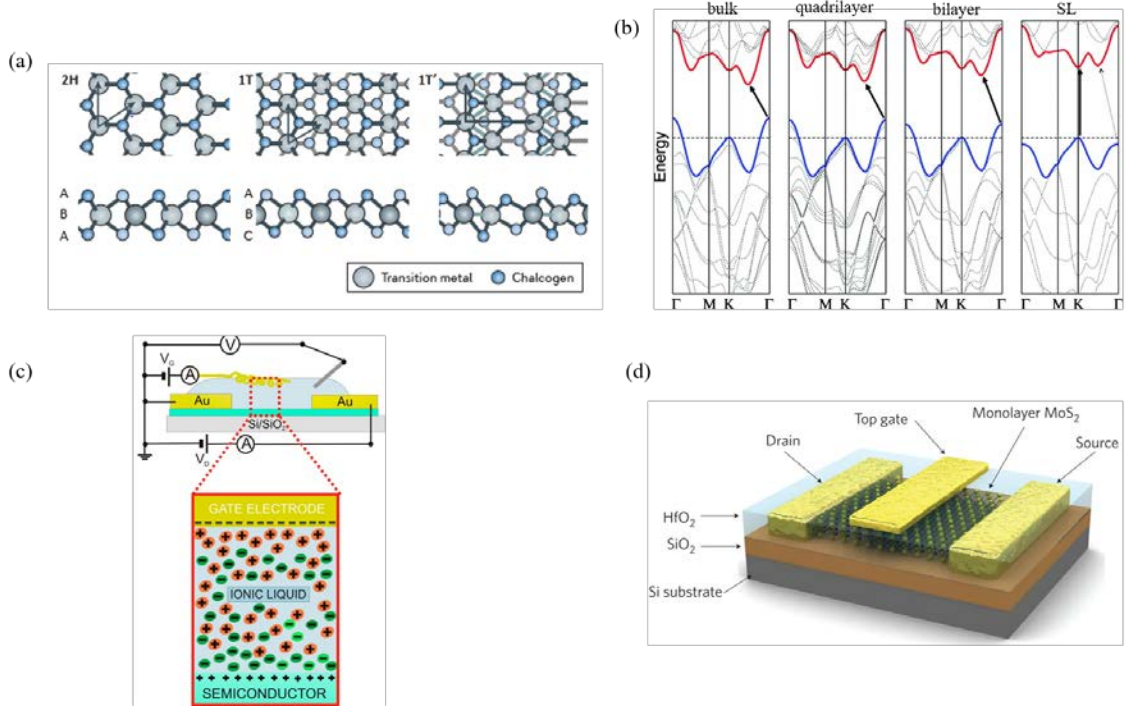


Figure 1.1. (a) Atomic structure of SL TMDCs in trigonal prismatic (2H), distorted octahedral (1T) and dimerized (1T') phases. The arrows denote the unit cell vectors. (b) Electronic band structure of bulk, quadrilayer, bilayer, and SL MoS<sub>2</sub>. The valence band and conduction band are represented by solid blue and red lines, respectively. The arrow indicates the lowest energy transition. With decreasing number of layers, the indirect bandgap in bulk gradually becomes the direct bandgap in SL. (c) Cross section of a WS<sub>2</sub>-based FET. Thin flakes of WS<sub>2</sub> coupled with an ionic liquid dielectric are placed between the gate electrode and substrate. (d) Schematic of SLMoS<sub>2</sub>-based FET. Figures are adapted with permissions from: (a) [20] © 2017 Springer Nature (b) [21] © 2010 American Chemical Society (c) [22] © 2012 American Chemical Society (d) [14] © 2011 Springer Nature.

Numerous works have studied the electronic and optical properties of TMDCs. The electronic band structure of TMDCs can be semiconducting (MoS<sub>2</sub>, WS<sub>2</sub>) [11, 12] or metallic (NbSe<sub>2</sub>) [23]. At  $\Gamma$  point, the bandgap generally undergoes a transition from indirect to direct when exfoliated into 2D form [21, 24], as is shown in Figure 1.1(b). The finite bandgap and ultrathin thickness of single-layer (SL) TMDCs has enabled fabrication of FET with high on/off ratio and mobility [14, 22] [see Figure 1.1(c) and (d) for examples]. The electronic band structure can also affect optical properties of TMDCs. For example, in

MoS<sub>2</sub>, an increase in bandgap energy leads to improvements in photoconductivity, absorption spectra, and photoluminescence [21, 24]. As SLMoS<sub>2</sub> has a larger bandgap than bulk MoS<sub>2</sub>, stronger photoluminescence of SLMoS<sub>2</sub> enables its application in photostable sensors which can be used to probe nanoscale dimensions. Charge density wave (CDW), a phenomenon where lattice distortions lead to modulation of electron charge density, has also been discovered in TMDCs [25]. Another commonly seen state in bulk TMDCs is the superconductivity phase, which can either compete or coexist with CDW phase [26, 27]. These findings have evoked a renewed interest in the theory behind CDW and superconductivity [25, 28].

Due to its importance in the design and application of electronic devices, thermal transport in TMDCs has also been intensively investigated over the past few years. MoS<sub>2</sub> has received most attentions due to its promising electronic [24], optical [29], and catalytic [30] properties. Different experimental techniques have been applied to measure the thermal conductivity ( $\kappa$ ) of MoS<sub>2</sub>. Using Raman method, the room-temperature  $\kappa$  in SL and 11-layer MoS<sub>2</sub> was measured to be  $34.5 \pm 4$  W/m/K [31] and 52 W/m/K [32], respectively. These values are significantly smaller than that of graphene. Another experiment using the same method shows that  $\kappa$  is 62.2 W/m/K at room-temperature which decreases to 7.45 W/m/K at 450K [33]. They attribute this temperature-dependence of thermal conductivity to increasing anharmonic phonon scattering as temperature is raised. The thermal bridge method has also been used to determine the room temperature  $\kappa$  of 4-layer and 7-layer MoS<sub>2</sub> to be 44-50 W/m/K and 48-52 W/m/K, respectively [34].  $\kappa$  of bulk MoS<sub>2</sub> has also been measured using time-domain thermoreflectance (TDTR) method to be

$80 \pm 22$  W/m/K [35]. Although the experimental data are fairly consistent, the theoretical calculations of MoS<sub>2</sub>  $\kappa$  scatter over almost one order of magnitude. A variety of computational approaches has been adopted in the theoretical calculations. Combining the non-equilibrium Green's function (NEGF) and density functional theory (DFT) method, the calculated room-temperature  $\kappa$  of MoS<sub>2</sub> nanoribbons is  $\sim 674$  W/m/K (armchair) and  $\sim 841$  W/m/K (zigzag), which serve as the upper limits of  $\kappa$  [36]. The anisotropy in the in-plane  $\kappa$  is attributed to different numbers of available channels for phonon transport along armchair and zigzag direction, in the frequency range  $[150, 200]$  cm<sup>-1</sup>. Another calculation estimates room-temperature  $\kappa$  to be  $\sim 300$  W/m/K by employing a variational approach for solving the linearized phonon Boltzmann transport equation (BTE) [37]. It is found that for phonons in MoS<sub>2</sub>, the Normal scattering dominates over Umklapp scattering up to room-temperature. On the other hand, several other calculations suggest a much lower  $\kappa$  at room-temperature. Iterative solution of the phonon BTE shows that the room-temperature  $\kappa$  of bulk MoS<sub>2</sub> is 98 W/m/K [38]. In this work, the MoS<sub>2</sub>  $\kappa$  changes from 98 W/m/K for bulk to 138 W/m/K for SL, exhibiting strong thickness dependence. Such increase in  $\kappa$  is a result of changes in phonon dispersion and anharmonicity induced by the change in thickness. Applying the single-mode relaxation time approximation (SMRTA) to solve the phonon BTE, a value of 83 W/m/K is obtained for  $\kappa$  of a typical sample size of  $1 \mu\text{m}$  at room temperature [39]. When the relaxation times (RTs) are estimated using the Klemens' theory rather than phonon BTE,  $\kappa$  at room-temperature of SLMoS<sub>2</sub> is calculated to be 26 W/m/K [40]. A similar value of 23.2 W/m/K for  $\kappa$  at room-temperature of SLMoS<sub>2</sub> is obtained using the NEGF method [41]. The much lower  $\kappa$  compared to graphene is explained by

showing that the dominant phonon mean free path (MFP) is 30-fold smaller than that of graphene. The deviation among results of different theoretical calculations are attributed to different approximations and force fields adopted.

Except MoS<sub>2</sub>, thermal properties of some other TMDCs have also been examined by experimental or theoretical methods. For Mo and W-based TMDCs, the in-plane and c-axis  $\kappa$  have been calculated by adopting SMRTA to solve phonon BTE [42]. The result shows that the in-plane  $\kappa$  is always larger than the c-axis  $\kappa$  at all temperature. The reason is attributed to the weak interlayer VDW interactions. In WS<sub>2</sub>,  $\kappa$  at room-temperature of SL and bilayer are measured by Raman method to be 32 and 53 W/m/K, respectively [43]. This result agrees well with another DFT calculation that produces a value of 31.8 W/m/K for  $\kappa$  of SL [44]. In MoSe<sub>2</sub>, optothermal measurements obtain  $59 \pm 18$  and  $42 \pm 13$  W/m/K for the  $\kappa$  of SL and bilayer sample [45]. Another experiment using TDTR method gives a value of 35 W/m/K for  $\kappa$  of bulk MoSe<sub>2</sub> [35]. These experimental data are consistent with theoretical calculations using non-equilibrium MD (NEMD) simulations that obtain  $43.88 \pm 1.33$  (armchair) and  $41.63 \pm 2.5$  (zigzag) W/m/K for SLMoSe<sub>2</sub> [46]. The room-temperature  $\kappa$  for SLWSe<sub>2</sub> with a typical sample size  $1 \mu m$  was found to be 3.935 W/m/K by solving phonon BTE, which is lower compared to other TMDCs [47]. The ultralow  $\kappa$  is attributed to the ultralow Debye frequency and heavy atom mass of WSe<sub>2</sub>. The  $\kappa$  of HfS<sub>2</sub> was calculated by solving phonon BTE, of which the results are  $\sim 9$  W/m/K for bulk [48] and  $\sim 14$  W/m/K for SL [49]. To date, no experimental measurement data of HfS<sub>2</sub>  $\kappa$  is available.

Above published results on the thermal properties of TMDCs are summarized in

Table 1.1. Various experimental and theoretical methods have been used to examine thermal transport in 2D TMDCs.

Table 1.1. Summary of studies on TMDCs thermal transport properties. “Exp.” and “Theo.” represent experimental and theoretical studies, respectively. In the “number of layers” column, “ $\infty$ ” represents bulk. In the “thermal conductivity” column, room-temperature values are given if no specification is indicated. We limit our literature search mostly to the past decade in order to examine the most recent development in the research field of TMDCs. Representative works for each kind of experimental or computational method have been collected.

		Ref.	Method	Number of layers	Thermal conductivity (W/m/K)
MoS <sub>2</sub>	Exp.	[31]	Raman spectroscopy	1	34.5 $\pm$ 4
		[32]	Raman spectroscopy	11	52
		[33]	Raman spectroscopy	1	62.2 at 300K 7.45 at 450K
		[34]	Thermal bridge	4	44-50
				7	48-52
		[35]	TDTR	$\infty$	80 $\pm$ 22
	Theo.	[36]	NEGF + DFT	1	~674 (armchair) ~841 (zigzag)
		[37]	BTE	$\infty$	~300
		[38]	BTE	$\infty$	98
				1	138
		[39]	BTE	1	83
		[40]	Klemens' theory	1	26
		[41]	NEGF	1	23.2
WS <sub>2</sub>	Exp.	[43]	Raman spectroscopy	1	32
				2	53
	Theo.	[44]	Slack theory	1	31.8
MoSe <sub>2</sub>	Exp.	[45]	Optothermal Raman	1	59 $\pm$ 18
				2	42 $\pm$ 13
		[35]	TDTR	$\infty$	35
	Theo.	[46]	NEMD	1	43.88 $\pm$ 1.33 (armchair) 41.63 $\pm$ 2.5 (zigzag)
WSe <sub>2</sub>	Theo.	[47]	BTE	1	3.935
HfS <sub>2</sub>	Theo.	[48]	BTE	$\infty$	~9
		[49]	BTE	1	~14

In summary, electronic and thermal transport properties of TMDCs have been widely studied in the past decade. The large and tunable bandgap, strong photoluminescence, and novel physics (CDW, superconductivity) of TMDCs suggest promising applications in nanoelectronics and optoelectronics. Thermal properties of TMDCs have been studied both experimentally and theoretically, where some general features such as low thermal conductivity and highly orientation anisotropic phonon properties are discovered. From a theoretical perspective, various computational approaches including molecular dynamics (MD), DFT and phonon BTE have been adopted to study thermal transport in TMDCs.

## **1.2 Challenges in thermal transport modeling**

Despite the great progress made in understanding thermal properties of TMDCs, there are still many questions remaining to be answered. In this thesis, we will focus on the challenges in modeling thermal transport of TMDCs.

First, an understanding of phonon properties in the full Brillouin zone (BZ) is lacking for some TMDCs. Phonons, the quantized collective modes of lattice vibrations, are the main heat carriers in non-metal crystals. Thermal transport properties of TMDCs are dictated by phonons. Full characterization of phonon properties includes phonon dispersion relation, group velocity, specific heat, and anharmonicity (RTs, MFPs, and so on) [50, 51]. To gain comprehensive knowledge of thermal transport in TMDCs, it is essential to examine the full BZ phonon properties. However, available data of the full BZ phonon dispersion relation and anharmonicity is still very limited for some TMDCs. For

instance, in  $\text{HfS}_2$ , previous studies primarily focus on properties of phonons at the BZ center  $\Gamma$  [52, 53, 54, 55] whereas an understanding of phonons away from  $\Gamma$  is lacking, despite their relevance in determining the material thermal properties [56].

The second challenge lies in determining the temperature-dependent phonon properties of TMDCs. Experimentally, it has already been shown that the thermal properties of TMDCs have a strong temperature-dependence [33, 57]. However, only few theoretical calculations have been performed to investigate the temperature dependence of phonon properties. Gu and Yang calculated temperature dependent thermal conductivity of SL  $\text{MX}_2$  ( $\text{M}=\text{Mo}, \text{W}, \text{Zr}, \text{and Hf}$ ,  $\text{X}=\text{S and Se}$ ) by solving phonon BTE, which only includes three-phonon scattering processes [49]. But four-phonon scattering has been shown to contribute a significant portion to the thermal conductivity of solids [58]. It remains unclear whether the four-phonon and higher order scattering processes in thermal transport of TMDCs can be neglected. The ultralow thermal conductivity of TMDCs implies strong phonon anharmonicity and considerable contribution from higher order scattering processes, thus further questioning the validity of widely used BTE approach. On the other hand, the spectral energy density (SED) method includes anharmonic scattering to all orders. Only very recently, researchers have started to apply SED method to study thermal transport in TMDCs [59, 60, 61]. Nevertheless, these works are all MD simulation-based. Thus, quality of their results is limited by the accuracy of the empirical potentials used in MD. It is still challenging to examine the effect of temperature on thermal properties of TMDCs.

Third, c-axis thermal transport in TMDCs remains relatively unexplored, in contrast to the widely studied in-plane thermal transport. Most of the attention is paid to the in-plane thermal transport of TMDCs to explore their applications in heat spreading. This is because the in-plane thermal conductivity is significantly higher than the c-axis thermal conductivity [62, 63]. However, recent studies have suggested that the c-axis thermal transport plays a central role in determining the performance of TMDC-based devices [64, 65, 14]. It is important to study the c-axis thermal transport in TMDCs. Currently, understanding of the c-axis thermal properties is lacking. Several studies have calculated the c-axis thermal conductivity of TMDCs including MoS<sub>2</sub>, WSe<sub>2</sub>, and MoTe<sub>2</sub>, by solving phonon BTE under the SMRTA [42]. This result contains intrinsic error because it has been shown that thermal conductivity of TMDCs obtained from the SMRTA solution of BTE differs from the full iterative solution, which is more accurate, by 14%~54% [49]. A very recent experiment on MoS<sub>2</sub> shows that the c-axis phonon mean free paths (MFPs) are at least ~10 nm, significantly larger than the kinetic theory estimate of 1.5-4 nm [66]. The existence of long c-axis MFP phonons have also been predicted by first-principle calculations in WS<sub>2</sub> and WSe<sub>2</sub> [49]. More theoretical investigations on the c-axis phonon characteristics such as RTs and MFPs are needed.

Last, artificial structures enabled by twisting, stacking, or folding the flexible layered structure of 2D TMDCs have been shown to possess interesting electronic and optoelectronic properties [67, 68, 69]. However, thermal properties of these novel nanostructures have largely been unexplored. For instance, for MoS<sub>2</sub>, folding its SL flakes leads to a decrease in the interlayer coupling and an enhancement of the photoluminescence

emission yield [70]. Tuning the stacking pattern between the bilayers in the folded structure can evoke strong valley and spin polarizations [71]. These distinct properties of folded MoS<sub>2</sub> are favored by valley-tronics and optoelectronics [72]. Nevertheless, the phonons and thermal properties of folded MoS<sub>2</sub> are not fully understood yet.

### 1.3 Objectives and outline

The objective of this thesis is to provide insights into full BZ phonon properties, anisotropic thermal transport, and relation between temperature and phonon anharmonicity of TMDCs, as discussed in the previous section. This work focuses on modeling phononic thermal transport in MoS<sub>2</sub> and HfS<sub>2</sub>. A variety of computational techniques including MD (see Sec. 2.2.1), DFT (see Sec. 2.2.2), and Car-Parrinello Molecular Dynamics (CPMD) (see Sec. 2.2.3) are used. The outline is as follows:

In Chapter 2, the theory of phonons and an overview of various computational approaches are presented. The harmonic phonon properties including dispersion relation, group velocity, and specific heat are determined by the 2<sup>nd</sup> order terms in the Hamiltonian while the anharmonic phonon properties including RTs and MFPs are dominated by the higher order terms in the Hamiltonian. The methodologies of calculating the lattice Hamiltonian using MD, DFT, and CPMD approaches are presented.

In Chapter 3, electronic and phonon properties of SL, bilayer, bulk, and folded MoS<sub>2</sub> are examined. We create folded MoS<sub>2</sub> by folding a SLMoS<sub>2</sub> sheet onto itself, resulting in a racket-shape like edge and a bilayer region (see Figure 3.5). The equilibrium

atomic structure of fold MoS<sub>2</sub> is obtained using a combination of classical and quantum methods. By varying wrapping length, we study how folding alters the configuration of MoS<sub>2</sub>. Subsequently, the electronic bandgap and phonon dispersion relation as a function of the wrapping length is determined. Thermal conductivity of folded MoS<sub>2</sub> are calculated and compared with those of SL, bilayer, and bulk MoS<sub>2</sub>.

In Chapter 4, we present a DFT study of temperature-dependent phonon properties of HfS<sub>2</sub> based on the quasi-harmonic approximation (QHA) (see Sec. 2.1.2). Phonon dispersion relation, group velocity, and specific heat of full BZ phonons are calculated. The Grüneisen parameters, derivative of phonon frequency with respect to lattice volume, are determined by a series of phonon calculations in deformed HfS<sub>2</sub> lattice. The phonon RTs are estimated under the Klemens' theory (see Sec. 2.3.2.1). Temperature effect on phonon RTs, phonon MFPs and  $\kappa$  are discussed. In addition, the characteristics of LO-TO splitting – coupling effect between optical  $\Gamma$  phonons and the electric field generated by the atomic displacements of the  $\Gamma$  phonons – are also examined.

In Chapter 5, a structural phase change of HfS<sub>2</sub> at around room-temperature is discovered. Such structural change is verified by both experiments and theoretical calculations. Raman spectroscopy and X-ray diffraction (XRD) experiments measure temperature-dependent  $\Gamma$  phonon frequency and lattice parameters of HfS<sub>2</sub>, respectively. Most notably, a change of temperature coefficient at 300 K is observed in phonon frequencies and lattice parameters. Moreover, an anomalous phonon stiffening was observed in c-axis phonon mode A<sub>1g</sub> below 300 K. Phonon frequencies calculated under QHA disagree with experimental data. Such disagreement is due to the simplification made

on phonon anharmonicity. Using CPMD simulations that consider anharmonicity to all orders, agreement between theory and experiments on phonon frequencies and lattice parameters are both achieved.

In Chapter 6, the major contributions of this work are presented. Suggestions for possible future work are discussed.

## Chapter 2 Theory of phonons and computational approach

A Phonon is a quantum description of atomic vibrations. For a crystalline solid, its phonon properties are determined by the interatomic potential or the Hamiltonian of the lattice. The harmonic terms in the Hamiltonian give rise to harmonic phonon properties while the anharmonic terms dominates the anharmonic phonon properties. Therefore, the determination of the lattice Hamiltonian and its derivatives plays a central role in examining phonon properties. This can be accomplished using a variety of computational approaches, which are categorized by their assumptions made on atomic interactions. Using a properly defined Hamiltonian, phonon properties including the dispersion relation, group velocity, specific heat, RT and thermal conductivity can be computed.

### 2.1 Theory of phonon

#### 2.1.1 Harmonic phonon

In this section, the theory of lattice dynamics (LD) under the harmonic approximation (HA) will be introduced. The HA assumes that atoms perform small oscillations about their equilibrium positions, which is generally true for temperature well below the melting temperature of the crystal.

A crystalline solid is often described by lattice, which is the periodic repetition of a unit cell in the real space. A unit cell is defined by three non-coplanar vectors:  $\mathbf{x}_1$ ,  $\mathbf{x}_2$ , and  $\mathbf{x}_3$ . Consider a crystal with a total number of  $N = N_1 N_2 N_3$  unit cells and periodic boundary conditions. Each unit cell has  $n_a$  atoms inside. Therefore the total number of

atoms is  $N_a = n_a N$ . We index the unit cells with a triplet of integers  $l = (l_1, l_2, l_3)$  where  $l_\alpha \in [1, N_\alpha]$  ( $\alpha = 1, 3$ ). The equilibrium position of the origin of each unit cell can be specified by  $\mathbf{r}_l = \sum_{\alpha=1}^3 l_\alpha \mathbf{x}_\alpha$ . Let us index the atoms in each unit cell with  $b \in [1, n_a]$  and represent the vector between origin of the unit cell and the atom by  $\mathbf{r}_b$ , so the position of the  $b$ th atom in the  $l$ th unit cell is given by  $\mathbf{r}(lb) = \mathbf{r}_l + \mathbf{r}_b + \mathbf{u}(lb)$  where  $\mathbf{u}(lb)$  is the displacement of this atom from its equilibrium position. Only the atom displacement is time dependent, therefore we have  $\dot{\mathbf{r}}(lb) = \dot{\mathbf{u}}(lb)$ .

The harmonic phonon theory can be easily derived using the LD method. We start by deriving the equation of motion (EOM) of all atoms in the lattice using the Lagrangian's method. Choosing the coordinates of all atoms as the generalized coordinates, the Lagrangian of a crystal is given by

$$\mathcal{L} = \sum_{lb\alpha} \frac{m_b \dot{r}_\alpha(lb)^2}{2} - U \quad (2.1)$$

where  $m_b$  is the atom mass,  $U$  is the potential energy of the crystal. Replacing  $\dot{\mathbf{r}}(lb)$  with  $\dot{\mathbf{u}}(lb)$  and imposing the HA that assumes small atom displacements, the potential energy can be expanded into a Taylor series around the equilibrium coordinates as

$$U = U_0 + \sum_{lb\alpha} \left. \frac{\partial U}{\partial u_\alpha(lb)} \right|_0 u_\alpha(lb) + \frac{1}{2} \sum_{lb\alpha, l'b'\beta} \Phi_{\alpha\beta}(lb, l'b') u_\alpha(lb) u_\beta(l'b') + O(u_\alpha(lb) u_\beta(l'b') u_\gamma(l''b'')) \quad (2.2)$$

The first term is a constant energy. The second term has to vanish since we are expanding about the equilibrium position, the gradients of the potential energy that appear in the coefficients are all zeros. The second term is the summation of 2<sup>nd</sup> order derivatives of the

potential energy with respect to the displacements of pairs of atoms, multiplied by the displacements of the atoms. The coefficient  $\Phi_{\alpha\beta}(lb, l'b')$  is a  $3N_a \times 3N_a$  matrix which is usually referred to as the force constant matrix

$$\Phi_{\alpha\beta}(lb, l'b') = \frac{\partial^2 U}{\partial u_\alpha(lb) \partial u_\beta(l'b')} \quad (2.3)$$

. The higher than 2<sup>nd</sup> order terms in Eq. (2.2) are neglected under the HA.

Taking Eq. (2.2) back into Eq. (2.1), we have

$$\mathcal{L} = \sum_{lb\alpha} \frac{m_b \dot{u}_\alpha(lb)^2}{2} - \frac{1}{2} \sum_{lb\alpha, l'b'\beta} \Phi_{\alpha\beta}(lb, l'b') u_\alpha(lb) u_\beta(l'b') \quad (2.4)$$

Using Eq. (2.4), we arrive at the Euler-Lagrangian EOM of the atoms

$$m_b \ddot{u}_\alpha(lb) = - \sum_{l'b'\beta} \Phi_{\alpha\beta}(lb, l'b') u_\beta(l'b') \quad (2.5)$$

Next, we assume a plane-wave solution that incorporates periodicity of the lattice as

$$u_\alpha(lb) = \frac{1}{\sqrt{m_b}} A_\alpha(\mathbf{q}; b) e^{i\mathbf{q} \cdot \mathbf{r}_l - i\omega(\mathbf{q})t} \quad (2.6)$$

where  $\mathbf{q}$  is the wavevector,  $A_\alpha(\mathbf{q}; b)$  is the eigenvector,  $\omega(\mathbf{q})$  is the frequency. The wavevector  $\mathbf{q}$  is restricted by the size of the lattice through the Born-von Karman boundary conditions [73]. Here we introduce the reciprocal lattice vectors  $\mathbf{y}_\alpha$  ( $\alpha = 1, 3$ ) that satisfy relation with the real-space lattice vectors  $\mathbf{x}_\alpha \mathbf{y}_\beta = 2\pi \delta_{\alpha\beta}$ . The allowed wavevector is given in terms of the reciprocal lattice vector as

$$\mathbf{q} = \sum_{\alpha} \frac{n_{\alpha}}{N_{\alpha}} \mathbf{y}_{\alpha}, \text{ for integer } n_{\alpha} \in [0, N_{\alpha} - 1] \quad (2.7)$$

In this way, we have defined a one-to-one mapping between the real-space lattice and the reciprocal space lattice. From now on, we will work in the  $\mathbf{q}$ -space.

Substituting Eq. (2.6) into Eq. (2.5), we obtain

$$\omega^2(\mathbf{q})A_\alpha(\mathbf{q}; b) = \sum_{\beta b'} D_{\alpha\beta}(\mathbf{q}; bb') A_\beta(\mathbf{q}; b') \quad (2.8)$$

where

$$D_{\alpha\beta}(\mathbf{q}; bb') = \sum_{l'} \frac{1}{\sqrt{m_b m_{b'}}} \Phi_{\alpha\beta}(\mathbf{r}_{l'}; bb') e^{i\mathbf{q} \cdot \mathbf{r}_{l'}} \quad (2.9)$$

is a  $3n_a \times 3n_a$  matrix which is called the dynamical matrix. Comparing Eq. (2.8) with Eq. (2.5), we find that the initial set of  $3N_a$  coupled equations has been separated into  $N$  sets of  $3n_a$  uncoupled equations.

The solution to Eq. (2.8) can be obtained by diagonalizing the dynamical matrix  $D$ , which yields  $3n_a$  eigenvalue-eigenvector pairs. One such pair is referred to as a phonon mode, indexed by  $\varphi = (\mathbf{q}, \nu)$  where the index  $\nu$  goes over all the  $3n_a$  branches. The eigenvalue  $\omega_\varphi$  and eigenvector  $\mathbf{A}_\varphi$  are the frequency and mode shape of the phonon, respectively. At each wavevector  $\mathbf{q}$ , a distinct set of phonon modes is obtained. From a microscopic point of view where  $N$  is a finite number, there are only  $N$  allowed wavevectors. From a macroscopic point of view, for a real crystal where  $N \rightarrow \infty$ , the wavevector  $\mathbf{q}$  can be viewed as a continuous variable. In practice, usually a dense  $\mathbf{q}$  point grid is chosen for phonon calculations, in order to represent the continuous  $\mathbf{q}$  in a real material.

Having solved Eq. (2.8), we are able to formulate some important harmonic phonon properties. Phonon dispersion relation refers to the relation between phonon frequency  $\omega$  and wavevector  $\mathbf{q}$ , namely  $\omega_\varphi(\mathbf{q})$ . Phonon group velocity originates from the wave nature of atom vibrations and is given by  $\mathbf{v}_\varphi = \frac{\partial \omega_\varphi}{\partial \mathbf{q}}$ . In thermal transport, the volumetric specific heat is an important quantity connecting the temperature and internal energy, which is defined by

$$C = \left. \frac{\partial E}{\partial T} \right|_V \quad (2.10)$$

where  $E$  is the internal energy and the derivative is take at constant volume  $\Omega$ ,  $T$  is temperature. The energy of a specific phonon mode is

$$E_\varphi = \left(n + \frac{1}{2}\right) \hbar \omega_\varphi \quad (2.11)$$

where  $n = \frac{1}{e^{\hbar \omega_\varphi / k_B T} - 1}$  is the phonon occupation number that obeys Bose-Einstein distribution,  $\hbar$  is the Planck constant, and  $k_B$  is the Boltzmann constant,. The internal energy is composed of the ground state energy at 0 K ( $E_{GS}$ ) and temperature dependent vibrational energy ( $E_{vib} = \sum_\varphi E_\varphi$ ). Therefore we can rewrite Eq. (2.10) into

$$C = \left. \frac{\partial E}{\partial T} \right|_V = \left. \frac{\partial (E_{GS} + \sum_\varphi E_\varphi(T))}{\partial T} \right|_V = \sum_\varphi \frac{\partial E_\varphi}{\partial T} \quad (2.12)$$

Plugging Eq. (2.11) into Eq. (2.12), we get

$$C_\varphi = \sum_\varphi C_\varphi = \sum_\varphi w_\mathbf{q} k_B \left( \frac{\hbar \omega_\varphi}{k_B T} \right)^2 \frac{e^{-\frac{\hbar \omega_\varphi}{k_B T}}}{\left( e^{-\frac{\hbar \omega_\varphi}{k_B T}} - 1 \right)^2} \quad (2.13)$$

where  $w_q$  is the weight for each discrete  $q$  point in the BZ.

### 2.1.2 Quasi-harmonic phonons

Under the HA, phonons are described as non-interacting harmonic oscillators. The crystal is regarded as an idea phonon gas. Some of the thermodynamics properties, such as the specific heat, can be explained by the HA. However, there are some well-known thermodynamics properties of crystals, such as thermal expansion and thermal conductivity, that cannot be accounted for by the HA [74]. In a perfect crystal, harmonic phonon properties are independent of the configuration or the volume of the lattice, leading to zero thermal expansion coefficient (TEC) at all temperature. Moreover, no scattering between phonons under the HA would lead to an infinite thermal conductivity. To resolve above paradox, anharmonic effects have to be considered.

One attempt to consider the phonon anharmonicity in thermodynamics properties evaluation, is by adopting the quasi-harmonic approximation (QHA). In the QHA theory, the lattice anharmonicity is restricted to thermal expansion while the phonons are still described as harmonic oscillators within the HA [75, 76, 77, 78]. The anharmonicity is accounted for by the volumetric dependence of phonons.

To obtain phonon properties, one has to define an equilibrium lattice configuration first. In the QHA theory, the equilibrium lattice configuration is found by minimizing the Helmholtz free energy at a specific temperature. Starting from the HA, the partition function of a phonon mode with frequency  $\omega_\varphi$  is given by

$$Z_\varphi = \sum_{n=0}^{\infty} e^{-(n+\frac{1}{2})\frac{\hbar\omega_\varphi}{k_B T}} = e^{-\frac{\hbar\omega_\varphi}{2k_B T}} \sum_{n=0}^{\infty} e^{-\frac{n\hbar\omega_\varphi}{k_B T}} = \frac{e^{-\frac{\hbar\omega_\varphi}{2k_B T}}}{1 - e^{-\frac{\hbar\omega_\varphi}{k_B T}}} \quad (2.14)$$

The partition function due to the vibrational contribution of the lattice consisting all the harmonic oscillators is

$$Z = \prod_{\varphi} Z_\varphi = \prod_{\varphi} \frac{e^{-\frac{\hbar\omega_\varphi}{2k_B T}}}{1 - e^{-\frac{\hbar\omega_\varphi}{k_B T}}} \quad (2.15)$$

Therefore, the Helmholtz free energy from the vibrational contribution is [79]

$$F_v = k_B T \ln Z = \sum_{\varphi} w_q \left[ \frac{\hbar\omega_\varphi}{2} - k_B T \ln(1 - e^{-\frac{\hbar\omega_\varphi}{k_B T}}) \right] \quad (2.16)$$

By including the ground state energy  $E_{GS}$  of the lattice, we get the total Helmholtz free energy of the lattice

$$\begin{aligned} F(\{a\}, T) &= E_{GS}(\{a\}) + F_v(\{a\}, T) \\ &= E_{GS}(\{a\}) + \frac{1}{2} \sum_{\varphi} w_q \hbar\omega_\varphi(\{a\}) \\ &\quad - k_B T \sum_{\varphi} w_q \ln \left( 1 - e^{-\frac{\hbar\omega_\varphi(\{a\})}{k_B T}} \right) \\ &= E_{GS}(\{a\}) + F_v^0(\{a\}) + F_v^T(\{a\}, T) \end{aligned} \quad (2.17)$$

where  $\{a\}$  represents a set of lattice parameters defining the lattice configuration,  $F_v^0$  is the zero-point vibrational energy. By varying  $\{a\}$  and finding the one with the minimum Helmholtz free energy given by Eq. (2.17), the equilibrium lattice configuration at specific

temperature  $T$  is obtained. Subsequently, phonon dispersion relation can be determined by performing LD (see Sec. 2.3.1) calculations on the obtained equilibrium lattice structure.

### 2.1.3 Anharmonic phonons

The anharmonic parts of atomic potentials are the higher than 2<sup>nd</sup> order terms in Eq. (2.2). We can divide the atomic potential into harmonic ( $U_{HA}$ ) and anharmonic ( $U_{AN}$ ) parts by rewriting Eq. (2.2) as

$$\begin{aligned}
 U &= U_{HA} + U_{AN} \\
 U_{AN} &= \frac{1}{k!} \sum_{k=3}^{\infty} \sum_{l_1 b_1 \alpha_1, \dots, l_k b_k \alpha_k} \Phi_{\alpha_1, \dots, \alpha_k}^{(k)} u_{\alpha_1}(l_1 b_1) \cdots u_{\alpha_k}(l_k b_k) \\
 U_{HA} &= U_0 + \sum_{lb\alpha} \left. \frac{\partial U}{\partial u_{\alpha}(lb)} \right|_0 u_{\alpha}(lb) \\
 &\quad + \frac{1}{2} \sum_{lb\alpha, l'b'\beta} \Phi_{\alpha\beta}(lb, l'b') u_{\alpha}(lb) u_{\beta}(l'b')
 \end{aligned} \tag{2.18}$$

where  $\Phi_{\alpha_1, \dots, \alpha_k}^{(k)}(l_1 b_1, \dots, l_k b_k) = \left. \frac{\partial^k U}{\partial u_{\alpha_1}(l_1 b_1) \cdots \partial u_{\alpha_k}(l_k b_k)} \right|_0$  represents the  $k$ th derivatives of the potential energy.

When the anharmonic effects is weak, namely either at low temperature or in a crystal with weak anharmonicity, we can reasonably neglect the effect of  $U_{AN}$  and consider phonons to be harmonic. However, where  $U_{an}$  substantially contributes to the potential energy, the HA breaks down as the anharmonic phonons can no longer be uncoupled. The phonon scattering effect has to be considered and the potential described by Eq. (2.18) is used.

To quantitatively evaluate the phonon anharmonicity, it is convenient to introduce the concept of phonon RT and MFP. In the kinetic theory, phonon RT  $\tau$  is the time interval a phonon travels between successive collisions with other phonons [80]. The only property we postulate about  $\tau$  is that the probability that the particle will make a collision in the infinitesimal time interval  $\delta t$  is  $\delta t/\tau$ . Similarly, the phonon MFP is defined by  $\Lambda_\phi = v_\phi \tau$ , which is the average distance a phonon travels between successive collisions with other phonons. Based on these definitions, the lattice thermal conductivity is given by [80]

$$\kappa = \sum_{\phi} C_{\phi} v_{\phi} \Lambda_{\phi} \quad (2.19)$$

To predict lattice thermal conductivity, it is essential to calculate the phonon RTs of all modes. In Sec. 2.3.2, we will see this can be accomplished using a number of computational techniques.

## 2.2 Computational approaches

There is a broad range of computational approaches that can be used to solve phonon thermal transport problems in crystals. Different computational techniques apply to different characteristic length ( $L$ ) and time ( $t$ ) scales of the heat transfer processes, as shown in Figure 2.1 [81]. The length scale regime is decided by the phonon wavelength, phonon MFP and the device dimensions while the time scale regime is decided by the phonon collision or RT. The LD approach adopts the HA which only considers the harmonic terms in the lattice Hamiltonian and neglects the anharmonic terms. The DFT approach computes the lattice Hamiltonian using quantum mechanics method. Due to its

high computational cost, typically the system under interest contains at most a few thousand atoms. The MD approach computes the lattice Hamiltonian using classical mechanics method. It can be applied to systems with size varying from nanometers to micrometers, and the time scale can reach the same order with phonon RT. The BTE approach is valid for describing the thermal transport as long as the heat carriers – phonons can be viewed as particles. It spans over the length scale  $L > \Lambda$  and the time scale  $t > \tau_c$ , with the most capability to study multi-length and multi-time scale thermal transport.

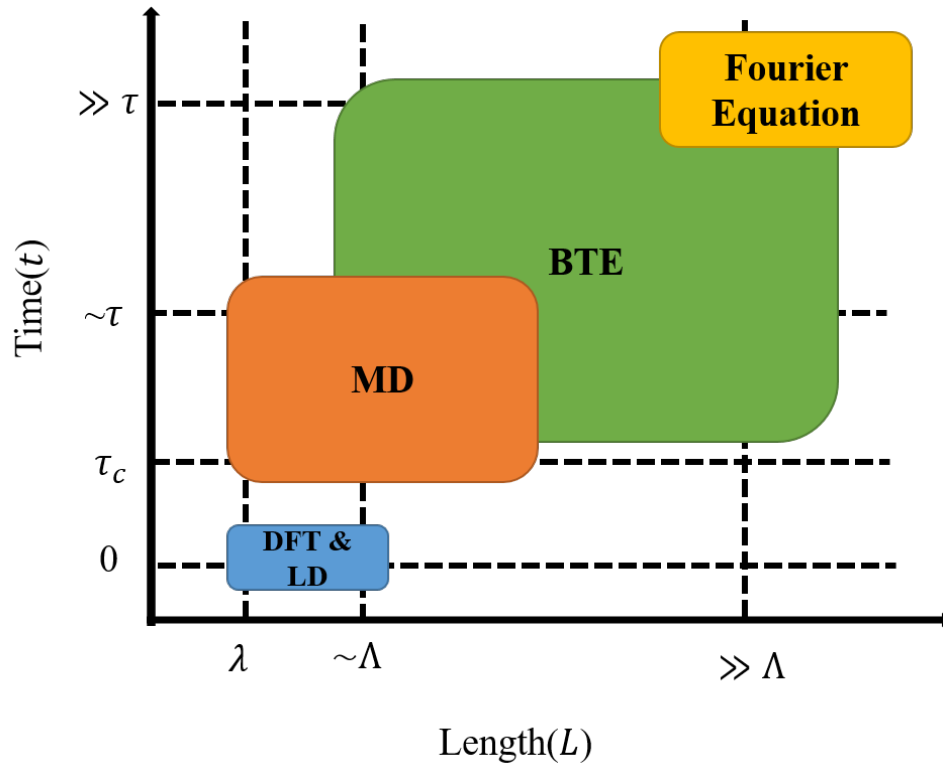


Figure 2.1. Schematic for range of length and time scale applicability of different phonon computational approaches (see Ref. [82]).  $\lambda$  is the phonon wavelength,  $\tau_c$  is the phonon collision time. The figure is adapted with permission from [82] © 2018 Springer Nature.

### 2.2.1 Molecular dynamics

MD is a computational technique that simulates the time evolution of a set of interacting atoms that are governed by Newton's second law. It was first developed in 1970s for studying dynamics of proteins [83] and enzymic reactions [84]. Ever since then, past few decades have seen a vast increase in the number of research works using MD approach. Nowadays, the size of the system in MD simulations can reach millions of atoms [85] and the time scale can reach milliseconds [86]. This advancement are largely due to the development in high performance computing and the cheap computational cost brought by the usage of classical potentials. In the field of thermal transport in 2D materials, MD has also been applied to investigate thermal properties of graphene [87], Si [88], MoS<sub>2</sub> [89], boron nitride [90], and so on.

In MD simulations, the Newton's EOM are integrated to capture the real-time trajectories of atoms. The most popular algorithm used in the integration is the Velocity Verlet algorithm [91]

$$\left\{ \begin{array}{l} \mathbf{r}_i(t + \Delta t) = [2\mathbf{r}_i(t) - \mathbf{r}_i(t - \Delta t)] + \mathbf{a}_i(t)\Delta t^2 + O(\Delta t^4) \\ \mathbf{v}_i(t + \Delta t) = \mathbf{v}_i(t) + \frac{1}{2}[\mathbf{a}_i(t) + \mathbf{a}_i(t + \Delta t)]\Delta t \\ \mathbf{a}_i(t) = -\frac{1}{m_i} \frac{dU(\mathbf{r}_1, \dots, \mathbf{r}_{N_a})}{dt} \end{array} \right. \quad (2.20)$$

where  $\mathbf{r}_i(t)$ ,  $\mathbf{v}_i$ , and  $\mathbf{a}_i$  are respectively the position, velocity, and acceleration of the  $i$ th atom at time  $t$ ,  $\Delta t$  is the timestep,  $m_i$  is the mass of the  $i$ th atom,  $U(\mathbf{r}_1, \dots, \mathbf{r}_{N_a})$  is the interatomic potential that is a function of the positions of all  $N_a$  atoms in the system. At

each step, the acceleration of every atom is evaluated using the potential and used to update its position. The general procedure of MD simulations is presented in Figure 2.2.

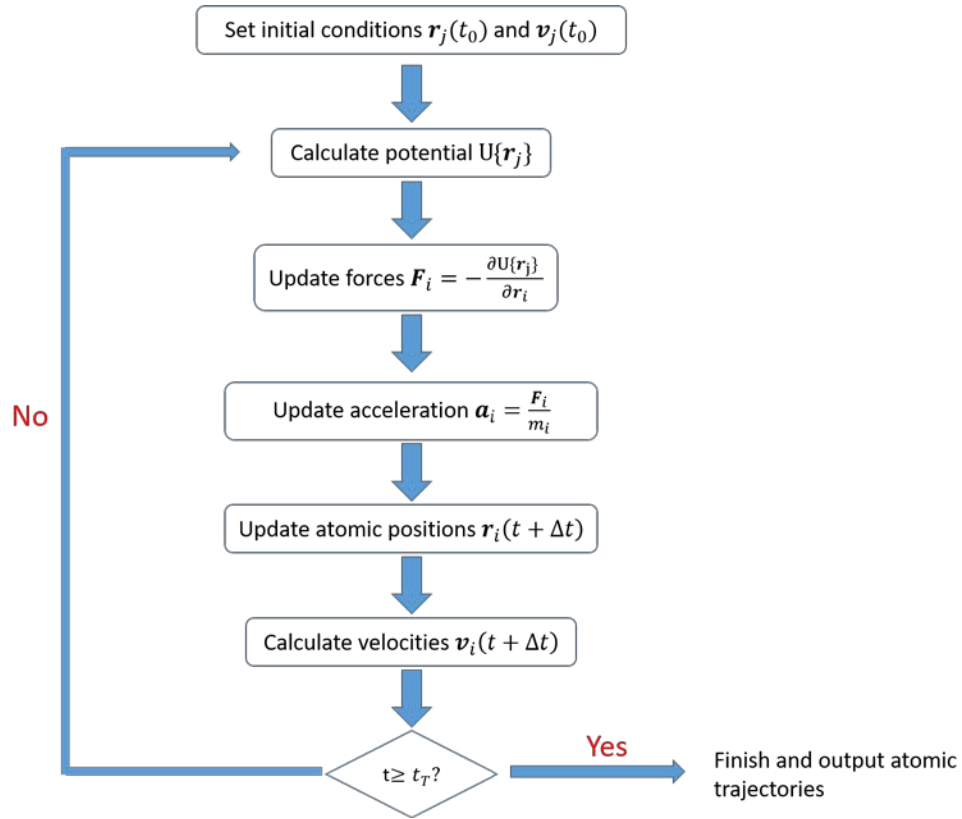


Figure 2.2. Flow chart of the MD simulations using the Velocity Verlet algorithm. Here,  $T$  represents the total simulation time. Notice that the velocities are updated after positions, in contrast to the intuitive thinking that one should update atomic velocities first before positions. The latter case will accumulate numerical errors in the integration scheme by integrating twice. Making use of the cancelation between Taylor expansion terms, the Velocity Verlet algorithm has higher order of accuracy than the integration by Taylor expansion alone.

The choice of timestep  $\Delta t$  should be carefully made for MD simulations. The timestep has to be chosen small enough to avoid discretization errors brought by Eq. (2.20) while not too small so as to simulate the system for a reasonable amount of time period. In practice, the maximum timestep is decided by the rate of fastest process in the system. For MD simulations on lattice vibrations, a reasonable choice of timestep is around one order

of magnitude smaller than the vibration period of highest frequency phonon mode. This is the common choice made for the timestep used in this thesis.

## 2.2.2 Density functional theory

### 2.2.2.1 Background

An exact theory for a system involving ions and interacting electrons is based on the many-body Schrödinger's Equation (SE):

$$\hat{H}\Psi(\mathbf{r}_i; \mathbf{R}_I) = E\Psi(\mathbf{r}_i; \mathbf{R}_I) \quad (2.21)$$

where  $\hat{H}$  is the Hamiltonian operator of the system containing the kinetic energy operator and potential energy operator,  $\Psi(\mathbf{r}_i; \mathbf{R}_I)$  is the many-body wavefunction as a function of positions of ions  $\mathbf{r}_i$  and variables of electrons ( $\mathbf{R}_I$  where  $I$  is the electron index). In a complete form

$$\begin{aligned} \hat{H} = & -\sum_i \frac{\hbar^2}{2m_i} \hat{\nabla}_{\mathbf{r}_i}^2 - \sum_I \frac{\hbar^2}{2m_e} \hat{\nabla}_{\mathbf{R}_I}^2 - \sum_{iI} \frac{Z_i e^2}{|\mathbf{r}_i - \mathbf{R}_I|} \\ & + \frac{1}{2} \sum_{IJ} \frac{e^2}{|\mathbf{R}_I - \mathbf{R}_J|} + \frac{1}{2} \sum_{ij} \frac{Z_i Z_j e^2}{|\mathbf{r}_i - \mathbf{r}_j|} \end{aligned} \quad (2.22)$$

where  $Z$  is the atomic number,  $m_e$  is the mass of electron,  $e$  is the electric charge of an electron,  $\hat{\nabla}$  is the Laplacian operator. In Eq. (2.22), the first and second terms are kinetic energy operator of ions and electrons, the 3<sup>rd</sup> term is potential energy due to an electron being attracted to an ion, the 4<sup>th</sup> term is Coulomb interaction between electrons, and the 5<sup>th</sup> term is the ion-ion interactions.

The Coulomb term in the exact SE makes solving it extremely difficult. Numbers of assumptions have been proposed to simplify Eq. (2.22). The first assumption introduced is the Born-Oppenheimer approximation which decouples the motion of ions and electrons, and assumes that electrons respond instantaneously to any ionic motion using the fact that electrons have much smaller mass than ions. In the context of calculating electronic states where ions are at rest, the first term turns to zero and the 5<sup>th</sup> term is simply a constant, the Hamiltonian Eq. (2.22) can be written as

$$\hat{H} = - \sum_I \frac{\hbar^2}{2m_e} \hat{\nabla}_{\mathbf{R}_I}^2 + \sum_I U_e(\mathbf{R}_I) + \frac{1}{2} \sum_{IJ} \frac{e^2}{|\mathbf{R}_I - \mathbf{R}_J|} \quad (2.23)$$

where we rewrite the ionic potential experienced by electrons as  $U_e$ .

Despite having a simpler form of Eq. (2.23) under the Born-Oppenheimer approximation, the SE is still formidable to solve due to the nature of electrons – exchange and correlation. The exchange characteristic is the Pauli Exclusion Principle that  $\Psi$  should change sign if two electrons with the same spin interchange positions. The correlation characteristic means that the motion of every electron is affected by all the other electrons. Different attempts have been made to further simplify SE. They primarily focus on how to describe the exchange-correlation nature of electrons with high accuracy and reasonable computational cost. The DFT method is one of these attempts. The other attempts include the Hartree-Fock approximation, the X- $\alpha$  method, the GW approximation, and so on. The readers are referred to Ref. [92, 93] that discuss the many-body theory in solid state physics for more details.

### 2.2.2.2 Kohn-Sham equations and DFT

In order to describe the exchange-correlation effect, Hohenberg, Kohn and Sham developed a different way of looking at the problem which is called the Hohenberg-Kohn-Sham theorem [94, 95]. This theorem constitute the fundamental ideas behind the DFT.

In DFT, the major assumption is that there is a one-to-one mapping between the electron wavefunction  $\Psi$  and electron density  $\rho(\mathbf{R})$  which is defined as

$$\rho(\mathbf{R}) = N_e \int \Psi^*(\mathbf{R}, \mathbf{R}_2, \dots, \mathbf{R}_{N_e}) \Psi(\mathbf{R}, \mathbf{R}_2, \dots, \mathbf{R}_{N_e}) d\mathbf{R}_2 \dots d\mathbf{R}_{N_e} \quad (2.24)$$

where  $N_e$  is the number of electrons in the system.

Taking Eq. (2.24) into Eq. (2.23), after some derivations, one arrives at the single-particle equations (Kohn-Sham equations)

$$\left[ -\frac{\hbar^2}{2m_e} \hat{\nabla}_{\mathbf{R}_I}^2 + U^{eff}[\mathbf{R}, \rho(\mathbf{R})] \right] \phi_I(\mathbf{R}) = \epsilon_I \phi_I(\mathbf{R}) \quad (2.25)$$

where  $U^{eff}[\mathbf{R}, \rho(\mathbf{R})] = U(\mathbf{R}) + e^2 \int \frac{\rho(\mathbf{R}')}{|\mathbf{R} - \mathbf{R}'|} d\mathbf{R}' + \frac{\delta E^{XC}[\rho(\mathbf{R})]}{\delta \rho(\mathbf{R})}$  is the effective ionic potential,  $\phi$  is the single-electron wavefunction,  $E^{XC}$  is the exchange-correlation functional of which the explicit expression is unknown. Finding a proper expression of  $E^{XC}[\rho(\mathbf{R})]$  is the major challenge in DFT.

### 2.2.2.3 Exchange-correlation functional

The local density approximations (LDA) [96, 97] is one of the early attempts to model the exchange-correlation functional. The basic idea is that the exchange-correlation energy can be found by dividing the system into infinitesimally small volumes, each with a constant electron density. The contribution of such a volume to  $E^{XC}[\rho(\mathbf{R})]$  will be

equivalent to a homogeneous electron gas that has the same electron density as the volume. The LDA neglects non-local effect in the exchange-correlation effect, thus greatly saves the computational cost. However, LDA does not work well for systems where the electron density cannot be approximated by homogeneous gas.

To better account for inhomogeneity in the electron density, the generalized-gradient approximation (GGA) [98, 99] is developed. Under the GGA, the exchange-correlation functional takes the form  $E^{XC}[\rho(\mathbf{R})] = \int \epsilon^{XC}[\rho(\mathbf{R}), \nabla\rho(\mathbf{R})] \rho(\mathbf{R}) d\mathbf{R}$ . The electron density of a specific infinitesimal volume depends on both the local density and the density of the neighboring volumes. The coupling effect between the infinitesimal volume and its neighbors are described using the gradient of the electron density. Numerous forms have been proposed for  $\epsilon^{XC}[\rho(\mathbf{R}), \nabla\rho(\mathbf{R})]$ , among which the most popular ones are the Perdew and Wang (PW91) [100] and the Perdew-Burke-Ernzerhof (PBE) [101] forms. In this thesis, most DFT calculations employ the PBE form of exchange-correlation.

### 2.2.3 Car-Parrinello Molecular Dynamics

The MD approach may fail for covalent or metallic systems where the atomic interactions cannot be well represented by empirical potentials. The DFT approach, on the other hand, can provide an accurate description of chemical bonds in a variety of systems, but are limited by its demanding computational cost. The CPMD approach combines the advantages of MD and DFT approaches to achieve considerable accuracy and fast computational speed.

The CPMD method belongs to the class of *Ab initio* MD (AIMD) methods, which employ classical mechanics description of the ions and quantum description for the electrons. Historically, CPMD was a synonym for AIMD since it had dominated AIMD methods for a long time. The basic idea of AIMD is a generalized Lagrangian that includes treatment of both ionic and electronic degrees of freedom (DOF).

### 2.2.3.1 Generalized extended Lagrangian's method

In the theory of AIMD, the generalized Lagrangian of a many-body system is [102]

$$\mathcal{L}(\boldsymbol{\epsilon}, \dot{\boldsymbol{\epsilon}}, \boldsymbol{\theta}, \dot{\boldsymbol{\theta}}) = \frac{1}{2} m \dot{\boldsymbol{\epsilon}}^2 + \frac{1}{2} \mu \dot{\boldsymbol{\theta}}^2 + k_s \mu G(\|\boldsymbol{\theta} - \boldsymbol{\vartheta}\|) - E(\boldsymbol{\epsilon}, \boldsymbol{\vartheta}) \quad (2.26)$$

where  $\boldsymbol{\epsilon}$  and  $\boldsymbol{\theta}$  are the generalized ionic and electronic coordinates,  $\mu$  is the mass of electronic DOF,  $\boldsymbol{\vartheta}$  is a further electronic variable that is calculated from a function  $\boldsymbol{\vartheta} = \Omega(\boldsymbol{\epsilon}, \boldsymbol{\theta})$ ,  $G(\|\boldsymbol{\theta} - \boldsymbol{\vartheta}\|)$  is a function positive everywhere and goes to zero at  $\|\boldsymbol{\theta} - \boldsymbol{\vartheta}\| = 0$ ,  $k_s$  acts as a spring constant regulating the distance between the  $\boldsymbol{\theta}$  and  $\boldsymbol{\vartheta}$ . From the Euler-Lagrange equation, we can easily derive the EOM as

$$\begin{cases} m \ddot{\boldsymbol{\epsilon}} = -\frac{\partial E}{\partial \boldsymbol{\epsilon}} - \frac{\partial E}{\partial \boldsymbol{\vartheta}} \frac{\partial \Omega}{\partial \boldsymbol{\epsilon}} + k_s \mu \frac{\partial G}{\partial \boldsymbol{\vartheta}} \frac{\partial \Omega}{\partial \boldsymbol{\epsilon}} \\ \mu \ddot{\boldsymbol{\theta}} = -\frac{\partial E}{\partial \boldsymbol{\vartheta}} \frac{\partial \Omega}{\partial \boldsymbol{\theta}} + k_s \mu \left[ \frac{\partial G}{\partial \boldsymbol{\vartheta}} + \frac{\partial G}{\partial \boldsymbol{\vartheta}} \frac{\partial \Omega}{\partial \boldsymbol{\theta}} \right] \end{cases} \quad (2.27)$$

### 2.2.3.2 CPMD

By choosing  $\boldsymbol{\vartheta} = \boldsymbol{\theta}$  in the extended Lagrangian, Eq. (2.27) simplifies to the CPMD form as

$$\begin{cases} m \ddot{\boldsymbol{\epsilon}} = -\frac{\partial E}{\partial \boldsymbol{\epsilon}} \\ \mu \ddot{\boldsymbol{\theta}} = -\frac{\partial E}{\partial \boldsymbol{\theta}} \end{cases} \quad (2.28)$$

which can be combined with the standard DFT method.

From the Kohn-sham equation Eq. (2.25), the DFT functional of the total energy is given by

$$E[\phi_I(\mathbf{R}), \mathbf{r}_i, \alpha_v] = \sum_I \int_V d^3\mathbf{R} \phi_I^*(\mathbf{R}) \left[ -\frac{\hbar^2}{2\mu} \hat{\nabla}^2 \right] \phi_I(\mathbf{R}) + U[\phi_i(\mathbf{R}), \mathbf{r}_i, \alpha_v] \quad (2.29)$$

An additional parameter  $\alpha_v$  is introduced here to represent addition DOF due to the variations of the unit cell during CPMD simulations whereas the original Kohn-Sham equation considers fixed unit cell.

In order to reduce the demanding computational cost in DFT, the CPMD method adopts a different approach which considers the minimization of the energy functional as an optimization problem [103, 104]. The objective function is the energy functional  $E$  in Eq. (2.29). There are three groups of DOF in the system, namely the electron wavefunctions, ion positions, and unit cell shape and volume. Using unit cell vectors  $\mathbf{h} = (\mathbf{x}_1, \mathbf{x}_2, \mathbf{x}_3)$ , we can express the positions of ions in terms of the unit cell vectors as  $\mathbf{r}_i = \mathbf{h}\mathbf{S}$ , where  $\mathbf{S}$  is the relative coordinates of the ion with respect to the cell. Following the same idea, for electron wavefunctions  $\phi_I(\mathbf{R})$ , we can also express it in terms of the unit cell vectors as  $\phi_I(\mathbf{R}) = \frac{1}{\sqrt{V}} \phi(\mathbf{h}^{-1}\mathbf{R}) = \frac{1}{\sqrt{V}} \phi(\mathbf{s})$  where  $V$  is the unit cell volume [104].

Assuming all the variables are time dependent, a Lagrangian is introduced

$$\begin{aligned}
\mathcal{L}_{CPMD} &= \sum_I \frac{1}{2} \mu \int_V d^3r |\dot{\phi}_I(\mathbf{r})|^2 + \sum_i \frac{1}{2} m_i \dot{\mathbf{r}}_i^2 - E(\phi_I, \mathbf{r}_i, \alpha_v) \\
&= K[\dot{\phi}_I, \dot{\mathbf{r}}_i, \dot{\alpha}_v] - E(\phi_I, \mathbf{r}_i, \alpha_v)
\end{aligned} \tag{2.30}$$

which is consistent with Eq. (2.26) under the assumption that  $\boldsymbol{\vartheta} = \boldsymbol{\theta}$ . Eq. (2.30) defines a classical kinetic energy  $K$  which represents departure of the system from the self-consistent minimum of its total energy. Therefore, in a MD simulation, a diminishing  $K$  means that the thermodynamics equilibrium has been reached. As always, the Lagrangian is subject to the constraints of the orthonormality of wavefunctions

$$\int_V d^3\mathbf{r} \phi_I^*(\mathbf{r}, t) \phi_J(\mathbf{r}, t) = \delta_{IJ} \tag{2.31}$$

Finally, by taking derivative of the Lagrangian  $L$  with respect to time, we arrive at a set of EOM for the generalized coordinates  $\psi_I$ ,  $\mathbf{r}_i$ , and  $\alpha_v$ .

$$\begin{cases} \mu \ddot{\psi}_I(\mathbf{r}_I, t) = -\frac{\delta E}{\delta \psi_I^*(\mathbf{r}_I, t)} + \sum_j \eta_{IJ} \psi_J(\mathbf{r}_J, t) \\ m_i \ddot{\mathbf{r}}_i = -\nabla_{\mathbf{r}_i} E \\ \mu_v \ddot{\alpha}_v = -\frac{\partial E}{\partial \alpha_v} \end{cases} \tag{2.32}$$

where  $\eta_{ij}$  is the Lagrangian multiplier of the wavefunction orthonormality constraints, i.e. Eq. (2.31). The second equation in Eq. (2.32) represents ionic dynamics that could have a real physical meaning of the trajectories of ions. As the temperature associated with  $K$  is reduced to zero by varying the generalized velocities  $\dot{\psi}_I$ ,  $\dot{\mathbf{r}}_i$ , and  $\dot{\alpha}_v$ , the equilibrium state is achieved.

## 2.3 Thermal transport calculations

In the previous section, we visit the basic theory behind various computational approaches. We will focus on the application of these techniques in the calculation of thermal transport properties in this section.

### 2.3.1 Phonon dispersion relation

As is shown in Sec. 2.1.1, the phonon dispersion relation is calculated by diagonalizing the dynamical matrix  $D$ . One starts from the interactions between atoms to evaluate the force constant matrix  $\Phi$ . Then the dynamical matrix of a phonon at a given point in the reciprocal lattice can be constructed and diagonalized. The resulting eigenvalues of the dynamical matrix are the phonon frequencies.

Determination of the force constant matrix plays a central role in calculating the phonon dispersion relation. One way to achieve this is using the small displacement method [105, 106, 107]. The basic idea is displacing each atom in the unit cell by a small amount and evaluating the resultant forces exerted on the other atoms. In principle,  $3n_a$  calculations have to be performed since there are  $3n_a$  DOF. However, this number can be substantially reduced, making use of the lattice symmetry. It should be noted that the force constant calculated in this way is a sum over the supercells of forces between one atom and all periodic images of another. It is not exactly the force constants entering the dynamical matrix, which are the ones for the infinite lattice. Therefore, it is required that the supercell size is large enough for the forces at the boundary of the supercell fall off to negligible values.

Another approach to determine the force constant matrix is the density functional perturbation theory (DFPT) [108, 109, 110] under the framework of DFT. The idea is based on the linear response theory and DFT. A phonon introduces displacements on the atoms that are described by the phonon polarization vectors. These displacements introduce perturbations to the potential, leading to a change in the electron density  $\rho(\mathbf{R})$  that is expressed as

$$\delta\rho(\mathbf{R}) = \int \zeta(\mathbf{R}, \mathbf{R}') \delta U d\mathbf{R}' \quad (2.33)$$

where  $\delta U$  is the change in the potential due to the presence of phonons and  $\zeta(\mathbf{R}, \mathbf{R}')$  is the coefficient of linear response. Using the perturbed potential, the force constants can be calculated using the “2n+1” theorem [110].

## 2.3.2 Phonon relaxation time

### 2.3.2.1 Klemens’ theory

The Klemens’ theory relates the phonon RT to Grüneisen parameter [111, 112]. The Grüneisen parameter provides information about the thermal expansion and anharmonic phonon-phonon interactions. The volumetric Grüneisen parameter is defined as [113]

$$\gamma_{\phi}^V = -\frac{\partial(\ln \omega_{\phi})}{\partial(\ln V)} = -\frac{V_0}{\omega_{\phi}^0} \frac{\partial \omega_{\phi}}{\partial V} \Big|_0 \quad (2.34)$$

One can also work with a three-dimensional form of the Grüneisen parameter as

$$\gamma_{\varphi}^{\alpha} = - \left. \frac{\partial(\ln \omega_{\varphi})}{\partial(\ln a^{\alpha})} \right|_0 = - \left. \frac{a_0^{\alpha}}{\omega_{\varphi}^0} \frac{\partial \omega_{\varphi}}{\partial a^{\alpha}} \right|_0 \quad (2.35)$$

where  $a^{\alpha}$  is the lattice parameter in the Cartesian direction  $\alpha$ , the script “0” represents a quantity taken at the equilibrium lattice configuration. In practice, the Grüneisen parameters are calculated by taking the first derivative of phonon frequency with respect to the corresponding lattice parameter at equilibrium via applying a central difference scheme to Eq. (2.34) or Eq. (2.35).

Using the obtained Grüneisen parameter, the phonon RT is calculated by [111, 112]

$$\frac{1}{\tau_{\varphi}} = \frac{2k_B T}{m v^2 \omega_D} (\gamma \omega_{\varphi})^2 \quad (2.36)$$

where  $\omega_D$  is the Debye frequency,  $\gamma$  is the Grüneisen parameter averaged over all phonon modes, and  $v$  is the average phonon group velocity at the long-wavelength limit given by  $\frac{1}{v^3} = \frac{1}{3} \left( \frac{1}{v_{LA}^3} + \frac{1}{v_{TA}^3} + \frac{1}{v_{ZA}^3} \right)$  [111]. To better account for the anisotropy in phonon modes, the mode-dependent  $\gamma_{\varphi}$  and both the average velocity [41] and mode-dependent velocity [114, 115] have been introduced into Eq. (2.36)

$$\frac{1}{\tau_{\varphi}} = \frac{2k_B T}{m v^2 \omega_D} (\gamma_{\varphi} \omega_{\varphi})^2 \quad (2.37)$$

$$\frac{1}{\tau_{\varphi}} = \frac{2k_B T}{m \omega_D} \left( \frac{\gamma_{\varphi} \omega_{\varphi}}{v_{\varphi}} \right)^2 \quad (2.38)$$

### 2.3.2.2 Boltzmann transport equation

The phonon BTE provides another route to compute the phonon RTs. The BTE governs the phonon distribution function  $f_{\varphi}$  by [80, 116]

$$\frac{\partial f_\varphi}{\partial t} + \mathbf{v} \nabla f_\varphi = \left( \frac{\partial f_\varphi}{\partial t} \right)_{collision} \quad (2.39)$$

The LHS represents the spatial and time variation of  $f_\varphi$ , the right-hand-side (RHS) represents the scattering processes that lead to deviation of  $f_\varphi$  from its thermal equilibrium. The scattering process can include various sources such as the phonon-phonon, phonon-boundary, phonon-impurity scattering, and so on. In this thesis, the phonon-phonon scattering is considered.

In most situations, the BTE can be linearized based on the assumption that both the deviation of  $f_\varphi$  from thermal equilibrium and temperature gradient  $\nabla T$  is small [117, 118]. As a result,  $f_\varphi$  is written as

$$f_\varphi = f_\varphi^0 - \mathbf{F}_\varphi \nabla T \frac{df_\varphi^0}{dt} \quad (2.40)$$

where  $f_\varphi^0 = (e^{\frac{\hbar\omega}{k_B T}} - 1)^{-1}$  is the equilibrium distribution function that follows the Bose-Einstein distribution and  $\mathbf{F}_\varphi$  measures the deviation from equilibrium, which is the unknown we are solving for. The widely adopted relaxation time approximation (RTA) simplifies the RHS of Eq. (2.39) as [80]

$$\left( \frac{\partial f_\varphi}{\partial t} \right)_{collision} = \frac{f_\varphi^0 - f_\varphi}{\tau_\varphi^{RTA}} \quad (2.41)$$

where  $\tau_\varphi^{RTA}$  is the phonon RT. Combining Eq. (2.39), Eq. (2.40), and Eq.(2.41), the linearized phonon BTE equation is obtained

$$\mathbf{F}_\varphi = \tau_\varphi^0 (\mathbf{v}_\varphi + \Delta_\varphi) \quad (2.42)$$

$$\Delta_\varphi = \frac{1}{N_m} \sum_{\varphi'\varphi''}^{\pm} [\Gamma_{\varphi\varphi'\varphi''}^+ (\mathbf{F}_{\varphi''} - \mathbf{F}_{\varphi'}) + \frac{1}{2} \Gamma_{\varphi\varphi'\varphi''}^- (\mathbf{F}_{\varphi''} + \mathbf{F}_{\varphi'})]$$

$$\frac{1}{\tau_\varphi^0} = \frac{1}{N_m} \left( \sum_{\varphi'\varphi''}^+ \Gamma_{\varphi\varphi'\varphi''}^+ + \frac{1}{2} \sum_{\varphi'\varphi''}^- \Gamma_{\varphi\varphi'\varphi''}^- \right)$$

where a  $\mathbf{q}$  mesh in the BZ centering at  $\Gamma$  and containing  $N_m$  points is introduced.  $\Gamma_{\varphi\varphi'\varphi''}^\pm$  is the three-phonon scattering rates that correspond to phonon creation and annihilation process. They can be calculated using the higher than 2<sup>nd</sup> order derivatives of the atomic potential, name the coefficients of  $U_{AN}$  in Eq. (2.18) [117].  $\tau_\varphi^0$  is the RT under the SMRTA, or referred to as the zeroth-order solution of phonon BTE. Solving (2.42) involves iterations where the values of  $\mathbf{F}_\varphi$  and  $\Delta_\varphi$  is updated in each iteration. As  $\mathbf{F}_\varphi$  and  $\Delta_\varphi$  depend on each other, a self-consistent solution is obtained when both values of  $\mathbf{F}_\varphi$  and  $\Delta_\varphi$  converge. Thus, the RT  $\tau_\varphi^{RTA}$  is obtained.

### 2.3.2.3 Phonon spectral energy density

Phonon RTs can also be calculated from the phonon SED approach. Derived from the anharmonic LD theory, the phonon SED is given by [119, 120]

$$\Phi^{SED}(\mathbf{q}, \omega) = \sum_{\varphi}^{3N_a} B_\varphi \frac{\frac{\Gamma_\varphi}{\pi}}{[\omega_\varphi - \omega]^2 + \Gamma_\varphi^2} \quad (2.43)$$

where  $B_\varphi$  is a mode-dependent constant. The SED is a superposition of  $3N_a$  Lorentzian functions centering at  $\omega_\varphi$ , having linewidth  $\Gamma_\varphi$ .

Alternatively, SED can be calculated from the atomic velocities. The kinetic energy normal mode coordinate  $\dot{q}(\varphi, t)$  is expressed by atomic velocities  $\dot{u}_\alpha(lb, t)$  and phonon eigenvectors  $A_\alpha^*(\mathbf{q}; b)$  as

$$\dot{q}(\varphi, t) = \sum_{\alpha, b, l}^{3, n_a, N} \sqrt{\frac{m_b}{N}} \dot{u}_\alpha(lb, t) A_\alpha^*(\mathbf{q}; b) \exp[i\mathbf{q} \cdot \mathbf{r}_l] \quad (2.44)$$

Given a set of atomic velocities from MD simulations and phonon mode eigenvectors, the SED can be calculated by

$$\begin{aligned} & \Phi^{SED}(\mathbf{q}, \omega) \\ &= 2 \sum_{\nu}^{3N_a} T(\varphi, \omega) = 2 \sum_{\nu}^{3N_a} \lim_{\tau_0 \rightarrow \infty} \frac{1}{2\tau_0} \left| \frac{1}{\sqrt{2\pi}} \int_0^{\tau_0} \dot{q}(\varphi, t) \exp(-i\omega t) dt \right|^2 \end{aligned} \quad (2.45)$$

and be fitted to Lorentzian functions using Eq. (2.43) to obtain  $\omega_\varphi$  and  $\Gamma_\varphi$ . The phonon

RT is related to the half linewidth of the SED by  $\tau_\varphi = \frac{1}{2\Gamma_\varphi}$ .

## **Chapter 3 Phonon and electronic properties of folded single-layer molybdenum disulfide**

The main content of this chapter appeared in the Journal article: Peng, Jie, Peter W. Chung, Madan Dubey, and Raju R. Namburu. "Tunable electron and phonon properties of folded single-layer molybdenum disulfide." *Nano Research* 11, no. 3 (2018): 1541-1553. Permission from [121] © 2018 Springer Nature.

TMDCs have layered structure bonded by weak VDW interactions. Therefore it is possible to bend their SL forms to create novel nanostructures that possess interesting properties different from their bulk forms. Similar idea has already been realized in other 2D materials such as graphene origami [122] and carbon nanotubes [123]. As one example, folding has already been shown to significantly change the photoluminescence spectrum and some in-plane properties of MoS<sub>2</sub> [124, 125]. However, little has been identified about how those properties have been modulated. In this work, we investigate the atomic structure, the ground state electronic, and phonon transport properties of folded SLMoS<sub>2</sub>. Since the folded structure is created by curving a single sheet, the wrapping length decides the relative size of the bilayer region to the closed loop along the edge. Different methods including variational mechanics, classical MD, and DFT approaches are employed. Equilibrium configuration of different folded structure indicates that the shape of closed loop edge is insensitive to changing wrapping length. Calculations of the electronic band gap of the folds find that it varies significantly as a function of wrapping length and

converges from below to the infinite bilayer gap value. On the other hand, the phonons are insensitive to the wrapping length despite being largely modulated by folding compared to its bulk counterparts. Indeed, the overall thermal transport behavior along the fold axis is unchanged. By modulating the electronic band gap value while holding thermal properties unaffected opens up exciting new possibilities for this emergent material.

### 3.1 Introduction

SLMoS<sub>2</sub> has attracted considerable interests for technological applications. It has an intrinsic direct band gap of 1.79 eV that is favored by electronic applications [126]. The large mobility of above 200 cm<sup>2</sup>V<sup>-1</sup>s<sup>-1</sup> suggests its novel application in optoelectronics and energy harvesting devices [124]. By phonon engineering, the figure of merit ZT of SLMoS<sub>2</sub> and thermoelectric performance could be greatly enhanced [125].

A number of recent studies found that folds in SLMoS<sub>2</sub> may occur naturally during fabrication or processing [70, 127]. Subsequent photoluminescence (PL) measurements of identified folded regions found a significant blue shift [127] that was attributed to exciton screening induced by the folded bilayer structure. Another experiment showed that varying layer stacking in folded SLMoS<sub>2</sub> flakes leads to a decrease in interlayer coupling and enhancement of photoluminescence emission yield [70] which bodes well for new possible device concepts.

Though only a few studies have specifically examined folds, a significant number of efforts that have examined the flat bilayer configuration. However, the folded configuration is merely the same single sheet placed into contact with itself to create a

bilayer structure with the fold along one edge. Thus, the understanding of bilayers should, in principle, provides insights into the structure and properties of the folded configuration. Bilayer studies of the effect of changing stacking pattern on the electronic band gap and optical nonlinearities [71], changing twist angle on PL [128], and strain effects [129, 130] should all convey when local fold effects are not of interest. It is also expected that studies of thermal properties [31, 131] will behave similarly. But a fundamental understanding of how folding changes the local ground state electronic and thermal properties is still lacking. Based on the previous experiments [127, 70], the fold does not appear to induce chemical reactivity and it therefore forms a well-defined structure whose properties are likely not sensitive to the manner in which it was created and therefore its properties may be readily reproduced. In situations where dimensions are on the order of mean free paths, knowledge of local properties and, perhaps more importantly, their convergence to the bilayer properties would be useful.

In this work, using a combination of methods – variational mechanics, classical potentials and density functional theory – we determine the equilibrium structure, the phonon transport, and the ground state electronic properties of folded configurations of SLMoS<sub>2</sub>. Size-dependence of properties is examined by studying changes in properties as a function of the length of the overlapping bilayer region.

## **3.2 Computational details**

Molecular statics, MD simulations using LAMMPS [132], and LD using GULP [133] were used to determine the folded configuration as well as estimate its thermal

properties. The classical potential is based on a parameterization for MoS<sub>2</sub> of the Stillinger-Weber potential [134] where the VDW interactions are described by a Lennard-Jones potential [135]. The DFT calculations employed Quantum-Espresso [136] to further optimize the folded configuration as well as determine the ground state electronic band structures. In all cases, structures from the molecular simulations were used as the starting configurations for DFT. We employed the PBE-GGA pseudopotential as implemented in Quantum-Espresso [101]. The VDW interaction was modeled using DFT-D2 which contains a semi-empirical force-field-based correction to the energy [137]. An energy cutoff of 40 Ry was used for all calculations with a convergence threshold for the self-consistent-field (SCF) calculation of 0.001 Ry. The DFT-based optimization was performed using analytical energy gradients with respect to atomic coordinates using BFGS (Broyden Fletcher-Goldfarb-Shanno) quasi-newton algorithm for Hessian update. Full relaxations were performed until the average atomic force was smaller than 0.001 Ry/a.u. and the energy difference between two consecutive relaxation configurations was smaller than 0.001 Ry.

Structure evaluation using the variational mechanics approach assumes the dominant contributions to the energy originate from elastic bending in the folded region as a function of the displacement of the neutral plane of the sheet and the VDW interactions that produces the attraction in the bilayer tail region [138]. The bending energy and bilayer attraction compete to find an equilibrium which is found in the stationary value of the curvature  $p$  that minimizes the folding energy relative to the energy of a single flat sheet

$$\Delta E = w \left[ \int_0^{L_{fold}} D_b p^2 ds + \epsilon_b \frac{L_{flat}}{2} \right] \quad (3.1)$$

The first term on the right hand side is the contribution from the bending energy and the second is from the bilayer attraction. Here,  $w$  is the width of the single layer in the direction parallel to the fold axis,  $L_{fold}$  is the length of the folded region,  $L_{flat}$  is the length of the flat region,  $D_b$  is the elastic bending stiffness, and  $\epsilon_b$  is the bilayer interaction energy per unit area. The dimensions are depicted in Figure 3.1 where  $L_{sheet}$  is the length of original flat sheet.

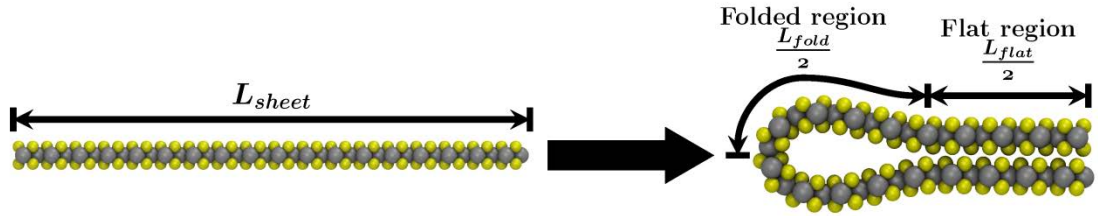


Figure 3.1. Dimensions of folded SLMoS<sub>2</sub> for variational mechanics solution. Left figure is the original flat sheet and right figure is of the folded sheet.

The bending stiffness and bilayer interaction are material parameters. The bending stiffness was estimated from the relation  $E = \frac{1}{2} D_b p^2$  using a sequence of molecular statics calculations of single-walled MoS<sub>2</sub> nanotubes of defined radii where  $E$  is the determined strain energy per unit area of the nanotube and  $p$  is the inverse of the defined nanotube radius. To determine  $D_b$ , a rectangular sheet of length  $l$  (armchair direction) and width  $w$  (zigzag direction) was rolled into a nanotube so that the circumference of the nanotube is  $l$  and tube length is  $w$ . The radius  $R$  and the curvature of the nanotube can be calculated from the relation  $l = 2\pi R = \frac{2\pi}{p}$ . The strain energy per unit area was calculated as the energy difference between the nanotube and the original flat sheet after energy

minimization was performed. Ten nanotubes with radii between 159.1 and 15.5 Å were studied. These correspond to tubes whose circumference contains 186, 167, 149, 130, 112, 93, 75, 55, 37 and 9 rectangular unit cells. All tubes were of length  $w=58.74 \text{ Å}^{-1}$  (19 unit cells). The rectangular unit cell used in these constructions is shown in Figure 3.4. The respective equilibrated curvatures ranged from 0.006287 to 0.06462 Å<sup>-1</sup>. The resulting strain energies are shown in Figure 3.2 from which the bending stiffness was estimated to be  $D_b = 8.6 \text{ eV}$ , which is comparable to reported values of  $D_b = 9.61 \text{ eV}$  [139] and  $D_b = 8.8\text{-}13.4 \text{ eV}$  [140]. The VDW interaction energy associated with the bilayer region is defined by  $E_{VDW} = w\rho_{VDW} \frac{L_{flat}}{2}$  where  $\rho_{VDW}$  is the interaction energy per unit area  $\rho_{VDW} = \frac{E_{bilayer} - 2E_{SLMoS_2}}{A} = -0.047 \text{ eV/Å}^2$ . We determined  $\rho_{VDW}$  by calculating  $E_{SLMoS_2}$  and  $E_{bilayer}$  using molecular statics from single and bilayer stacked rectangular sheets of length 80.32 Å (armchair direction) and width 58.74 Å (zigzag direction) with in-plane periodicity. The supercell was sized so that the effective interlayer spacing was 25 Å to exclude image interactions. The equilibrated intralayer distance in the bilayer configuration was determined to be 2.433 Å by energy minimization.

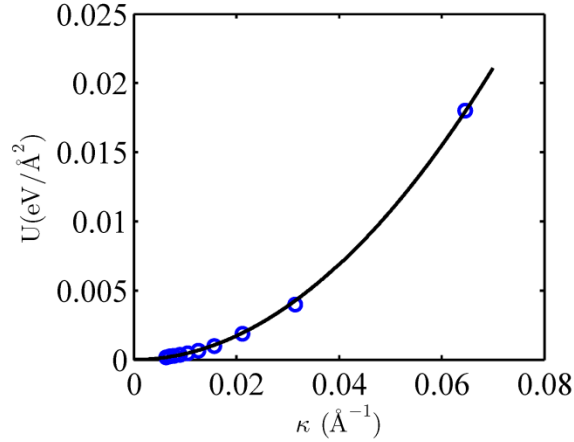


Figure 3.2. Strain energy VS curvature of SLMoS<sub>2</sub> nanotube. Open circles represent the strain energy obtained from molecular simulations and the line is the best fit used to estimate bending stiffness. Curvature  $p = \frac{1}{R}$  where  $R$  is the radius of SLMoS<sub>2</sub> nanotube which is defined as distance from center to middle Mo atomic layer.

The procedure to produce a fold in initially-flat SLMoS<sub>2</sub> sheets is as follows. The flat sheets of length  $L$  were placed in supercells whose widths are equal to the sheet width but whose other dimensions are twice the sheet length  $L$ . Aside from the obvious continuation of the sheet along the width direction, no image interaction effects could be noticed using this supercell size. Periodic boundary conditions were applied on all sides of the supercell. A timestep of 2 fs was used. After an initial low temperature NVT equilibration for  $10^5$  steps, forces were applied on the first three rows MoS<sub>2</sub> molecules on both ends of the flat sheet and three rows of molecules near the center were held fixed to facilitate the folding. When the two ends were brought together to within the VDW cutoff distance, the end forces and atom constraints were removed and attractive forces from the incipient bilayer interactions took over to produce a “zipping” effect that resulted in the configuration depicted schematically in Figure 3.1. After  $5 \times 10^5$  steps subsequent NVT

equilibration steps, we switched to an NPT ensemble to further equilibrate the system for another  $5 \times 10^5$  steps.

Free edges were initially used in the folding to resemble the structures observed in experiments [127]. The free edge energy is subsequently estimated by  $E_{edge} = \frac{1}{2a}(2E_{single} - E_{dual})$  where  $E_{single}$  is the energy of the single fold configuration and  $E_{dual}$  is the dual fold energy which comes from placing together the equilibrated single fold configuration and its copy, rotated  $180^\circ$ . The result has the appearance of a flattened tube. In this new configuration, six system sizes were created with  $2L=117.8 \text{ \AA}$  (22),  $149.9 \text{ \AA}$  (28),  $192.8 \text{ \AA}$  (36),  $235.6 \text{ \AA}$  (44),  $278.4 \text{ \AA}$  (52),  $310.6 \text{ \AA}$  (60) where the number in parentheses indicates the total number of unit cells in the wrap direction. A single unit cell is modeled along the fold direction. These sizes correspond to supercells containing 168, 216, 264, 312 and 348 atoms, respectively. The resulting structures were subsequently equilibrated before recording the total energy. The free edge energy was calculated to be  $E_{edge} = 3.94 \text{ eV/\AA}$ . The dual-fold structures serve as the starting configurations for the optimizations that follow using DFT. The removal of free edges avoids dangling bonds and spurious edge states.

With the dual-fold geometry obtained from the molecular simulations as the starting configuration, further optimization using DFT produced a representative supercell as shown in Figure 3.3. The resulting structure is clearly one-dimensional whose transport direction is only along the fold axis (zigzag) so that the  $\mathbf{q}$ -point mesh in the BZ needs only to be resolved along the axis. Only the  $\Gamma$ -point was used for structure optimization, while

for the electronic band structure calculation the  $\mathbf{q}$ -point mesh was set to  $10 \times 1 \times 1$ . We also computed the optimized structure and electronic band structure of bulk  $\text{MoS}_2$ , bilayer  $\text{MoS}_2$  and  $\text{SLMoS}_2$  to serve as references. The Monkhorst-Pack k-point meshes for these were  $8 \times 8 \times 8$ ,  $8 \times 8 \times 8$  and  $10 \times 10 \times 1$ , respectively.

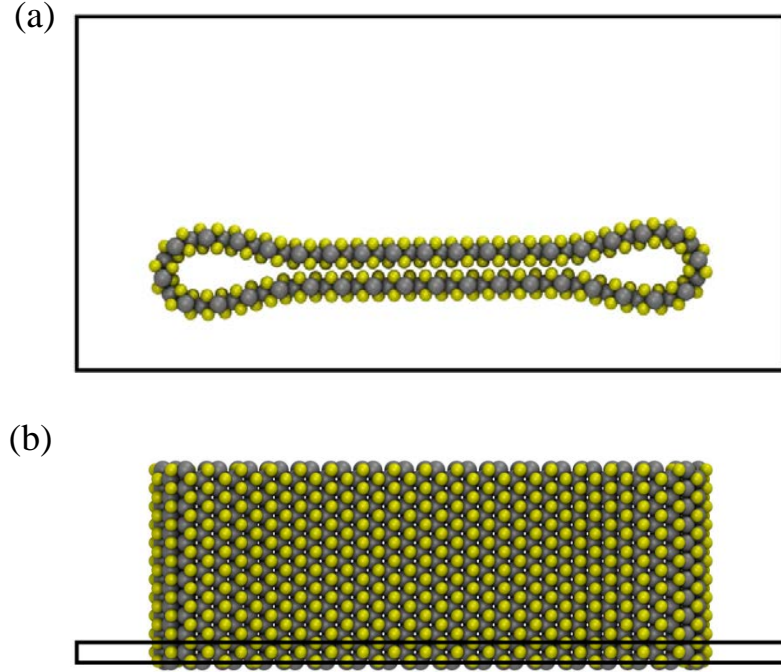


Figure 3.3. The  $10 \times 1 \times 1$  supercell of dual fold  $\text{SLMoS}_2$  (wrap length  $192.76 \text{ \AA}$ ) in DFT simulations. (a) Side view. (b) Top view. Vacuum layers of  $>10 \text{ nm}$  are used in the lateral directions.

The Green-Kubo method relates the thermal conductivity to the equilibrium current-current autocorrelation function based on the fluctuation-dissipation theorem and linear response theorem

$$\kappa_{\alpha\beta}(t) = \frac{1}{Vk_B T^2} \int_0^t \langle J_\alpha(\tau) J_\beta(0) \rangle d\tau \quad (3.2)$$

where the angular brackets represent the ensemble average,  $J$  is the heat current. This calculation can be performed directly in LAMMPS. For the trajectories, we used the same

configuration as was used in the phonon kinetic theory (see Sec. 2.1.3) and embark on a dynamics simulation with a timestep size of 1 fs. The dual fold supercell was created using 10x1x1 unit cells as depicted in Figure 3.3. The system was first run in NVT with Nose-Hoover heat bath for  $10^5$  timesteps to equilibrate at 300 K. Once the desired temperature was reached, we switched to the isothermal-isobaric ensemble (NPT) for another  $4 \times 10^5$  steps to further equilibrate the system at 300 K. Finally, a micro-canonical ensemble (NVE) which ran for  $2 \times 10^7$  timesteps was used to obtain the autocorrelation function and eventually the thermal conductivity. The correlation length was set to 200 ps which had been tested to be sufficient for the autocorrelation function to vanish and for the thermal conductivity to converge.

Phonon RT was obtained by fitting autocorrelation function given by MD simulations to a single exponential function:

$$\frac{\langle J(t)J(0) \rangle}{\langle J(0)J(0) \rangle} = Ae^{-\frac{t}{\tau}} \quad (3.3)$$

where  $A$  is a constant. Applying the gray approximation in the phonon kinetic theory which considers an averaged value for phonon RT and group velocity, the thermal conductivity can be expressed as:

$$\kappa = C\bar{v}\bar{\Lambda} = C\bar{v}^2\bar{\tau} \quad (3.4)$$

where  $\bar{v}$  is average phonon group velocity. So we can calculate the average phonon group velocity by  $\bar{v} = \sqrt{\frac{\kappa}{C\bar{\tau}}}$  and the phonon MFP by  $\bar{\Lambda} = \bar{v}\bar{\tau}$ .

Phonon calculations of bulk MoS<sub>2</sub>, bilayer MoS<sub>2</sub> and SLMoS<sub>2</sub> were also performed to serve as references. The respective Monkhorst-Pack **q**-point meshes for the unfolded configurations were  $10 \times 10 \times 10$ ,  $10 \times 10 \times 10$  and  $10 \times 10 \times 1$ . Rectangular sheets of size  $l = 74.97 \text{ \AA}$  and  $w = 58.74 \text{ \AA}$  ( $19 \times 14$  unit cells) were used.

### 3.3 Results and discussion

#### 3.3.1 Folded structure

A SLMoS<sub>2</sub> is comprised of a layer of Mo atoms sandwiched by two layers of S atoms. Interactions between atoms in SLMoS<sub>2</sub> are mainly covalent bonds while in bulk MoS<sub>2</sub>, adjacent MoS<sub>2</sub> layers are weakly attractive through VDW interactions. The stacked Mo and S layers of atoms are offset from one another to give a hexagonal structure that, in the bulk, forms a centrosymmetric trigonal prismatic crystal. The single layer and bulk lattices of MoS<sub>2</sub> are shown in Figure 3.4 with their respective unit cells. In the MD simulations, we employ single layer lattice parameters  $a = 3.09 \text{ \AA}$ ,  $c = 3.21 \text{ \AA}$ , bulk lattice parameters  $a = 3.09 \text{ \AA}$ ,  $c = 12.1 \text{ \AA}$  and interlayer spacing distance  $d = 2.445 \text{ \AA}$ , all of which were determined initially through molecular statics calculations using the classical potential described further below. The corresponding primitive unit cells are shown in the dashed-line boxes in Figure 3.4. The SLMoS<sub>2</sub> flat sheet was constructed by periodic arrangement of a rectangular cell shown by the black line box in Figure 3.4, for

which the  $1 \times 1 \times 1$  unit cell has dimensions  $\sqrt{3}a(\text{armchair}) \times a(\text{zigzag}) \times c = 5.35 \text{ \AA} \times 3.09 \text{ \AA} \times 3.21 \text{ \AA}$ . A likewise construction was used for the bulk structure.

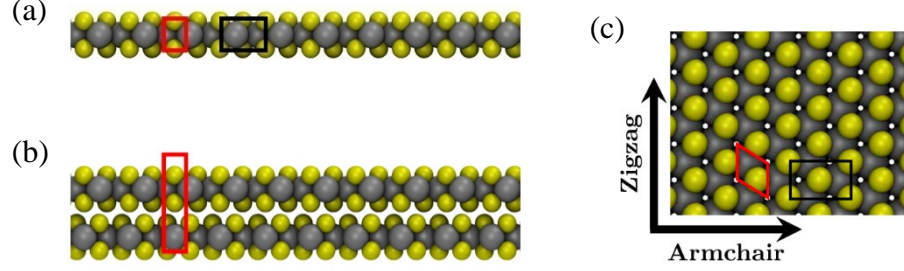


Figure 3.4. Side views of (a) single layer of MoS<sub>2</sub>, (b) two layers of bulk MoS<sub>2</sub>, and (c) Top view along c-axis. The top view for both SL and bulk appear identical. The primitive unit cells are shown in red line boxes. The rectangular unit cell is shown in the black line boxes.

We label the wrap axis as the axis in the direction of the sheet that is folded back onto itself. The fold axis is orthogonal to the wrap axis and runs along parallel to the fold. In this work, the wrap axis is limited to the armchair direction and fold axis along the zigzag direction. Size effects are studied using the size of the sheet along the wrap axis while the size of the sheet along the fold axis is held fixed. Dependence of the properties on the wrap and fold directions relative to the lattice vectors is not presently considered. The fact that a fold is created necessarily limits later discussions on transport to only one-dimension parallel to the fold axis.

The folded SLMoS<sub>2</sub> nanostructure has the appearance of a racket-shape folded region and a bilayer region that is observably flat. The flat region is composed of two SLMoS<sub>2</sub> sheets with the same stacking pattern and lattice parameter as bulk MoS<sub>2</sub> which has the AB stacking pattern of 2H MoS<sub>2</sub>. In the direction of the fold axis, the lattice parameter remains unchanged from the SLMoS<sub>2</sub> value. All of the present calculations

produced bulk stacking in the bilayer region. The lattice parameter in the zigzag direction does not change as a consequence of folding. The structure is shown in Figure 3.5(a). The lengths of the flat and folded regions are denoted as  $L_{flat}$  and  $L_{fold}$ , where both are measured using the centerplane of Mo atoms. The system size, or total wrap length, is thus defined as  $2L = 2(L_{flat} + L_{fold})$ .

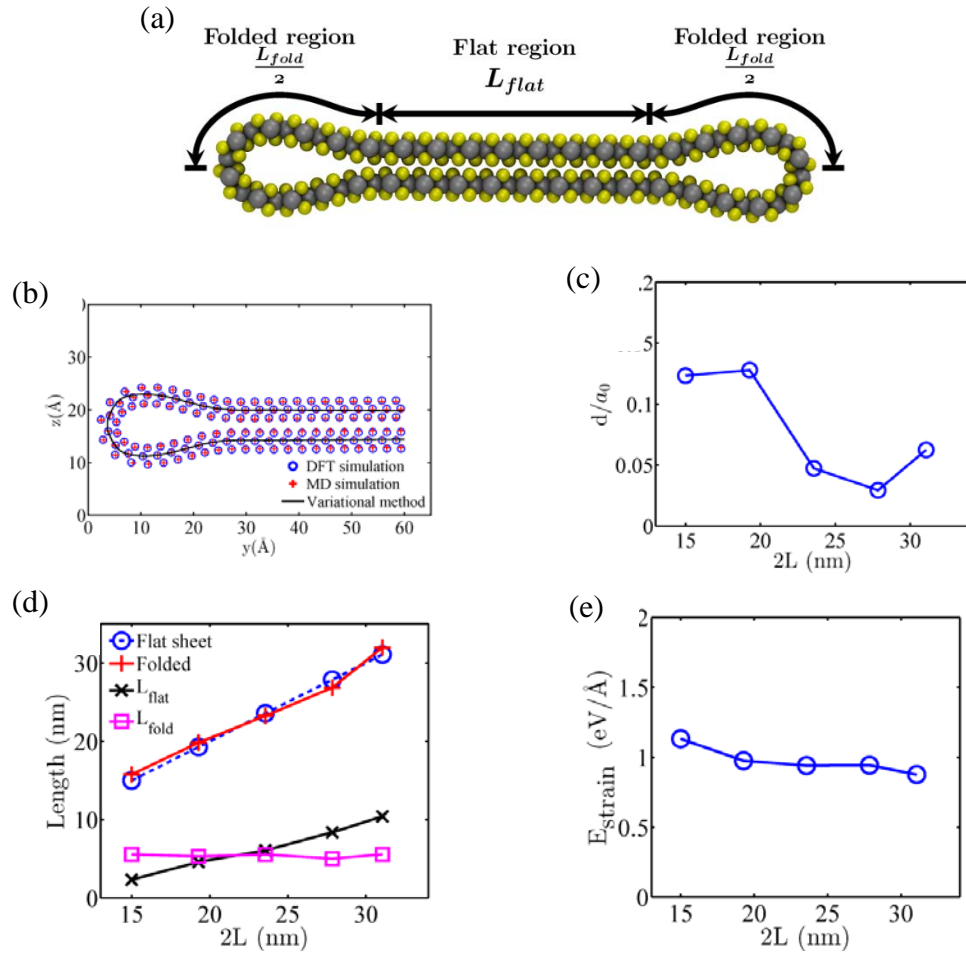


Figure 3.5. (a) Side view of equilibrium folded SLMoS<sub>2</sub> with  $2L = 192.8$  Å from DFT simulation. (b) Equilibrium configuration of folded SLMoS<sub>2</sub> ( $2L = 235.6$  Å) showing atomic coordinates from variational mechanics, molecular, and DFT methods. (c) Average atomic distance between folded SLMoS<sub>2</sub> nanostructure obtained from MD and DFT as functions of wrap length ( $2L$ ). The distances are divided by the single layer lattice constant  $a_0$ . (d) Equilibrated lengths of flat and folded regions as a function of original sheet length. (e) Strain energy per unit length of fold versus wrap length.

The varying methods to estimate the equilibrated folded structures were all in agreement including, remarkably, the variational mechanics solution. The resulting atomic structures from the three methods are depicted in Figure 3.5(b) for the case of  $2L = 235.6 \text{ \AA}$ . There is strong qualitative agreement in the prediction based on variational mechanics as evidenced by the coincidence of the center plane solution with nearly every Mo atom. The largest departures occur in the region adjacent to, but not at, the location of highest curvature and in the distant bilayer regions. The agreement of the solution with the classical potential result is expected to be slightly better than with the quantum result since the bending stiffness is obtained using the empirical potential.

Differences are observable between the results of the classical and quantum methods. In Figure 3.5(c), the differences are shown using  $d/a_0 = \frac{1}{a_0 N_a} \sum_{i=1}^N |\vec{r}_i^{MD} - \vec{r}_i^{DFT}|$  where  $a_0$  is the lattice constant of the single layer. Smaller wrap lengths appear to result in larger disparity between molecular and quantum results but average differences tend to be smaller than 15% of the lattice constant, or approximately  $0.46 \text{ \AA}$ . The smallest length that remained stable after the folding procedure is  $2L = 117.8 \text{ \AA}$  (22 unit cells). However, it resulted in a final equilibrium configurational energy that was significantly higher than the other lengths we considered and therefore was removed from further analysis. This is likely because of the disproportionate deformation experienced by the two different layers of S atoms, and the volume exclusion effects that lead to large repulsive forces among the S atoms in the inner layer indicates that having an equal number of S atoms inside and outside of the fold may be unphysical. Varying the number of S atoms by

removing them from the inner layer was not explicitly examined. Even smaller systems were either unable to maintain the racket shape or simply became flat again after releasing the folding forces. The largest of these, which is not shown here, was easily perturbed and preferred to take on spiral-like shapes with one of the free edges, aided by the exposed inner Mo layer, attaching orthogonally at random locations on the S surface. However, it was more common that the forces needed to maintain the fold were not sufficient to counteract the internal forces due to bending.

No dependence is observed between the curvature in the fold and the wrap length. Thus the configuration in the fold region exhibits an intrinsic behavior that is independent of the size of the adjacent bilayer region. It is therefore expected that any fold that wraps the armchair axis onto itself will produce a structural feature that is approximately 5.0-5.6 nm in distance between the points where curvature is finite. For all lengths studied, exactly 20 Mo atoms traverse this distance. The smallest radius of curvature is approximately 4 Å. The sizes of the folded and flat regions with varying  $2L$  are shown in Figure 3.5(d). The overall length of the sheet is not found to change appreciably due to folding. Namely,  $2L = 2L_{sheet}$ . The bending of the sheet results in asymmetric amounts of deformation in the outer and inner S layers. By comparing the interatomic separation of S atoms in the folded region and in the flat sheet, we observe that the outer layer has a tensile strain of around 11% while the inner layer has a compressive strain around 8%. To further confirm the lack of a size effect in the fold, the strain energy stored in the folded region is shown in Figure 3.5(e). The strain energy also does not change substantially with varying system size.

### 3.3.2 Electronic band structure.

The calculated bulk, bilayer, and single layer electronic band structures are shown in Figure 3.6, and their gap values compare well with known values as shown in Table 3.1. In the bulk, we estimate the indirect gap to be 0.99 eV from  $\Gamma$  to  $\Sigma = 0.25 \times 2\pi/a$ . This compares to 1.23 eV from the experiments. Our model of bilayer MoS<sub>2</sub> has an indirect band gap of 1.2 eV, which agrees well with the estimate of 1.2 eV from a DFT result using the PW91 exchange correlation functional pseudopotential.

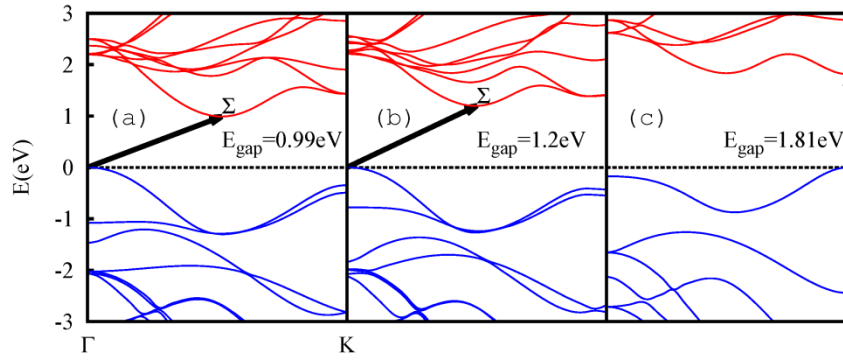


Figure 3.6. Electronic band structure of (a) Bulk MoS<sub>2</sub>. (b) Bilayer MoS<sub>2</sub>. (c) SLMoS<sub>2</sub>. Conduction bands (Red) and valance bands (Blue) and band gap (solid line arrow) are shown in the figure. The zero of the energy spectrum has been set to the valence band maximum (VBM) which is denoted by the horizontal dashed line. The conduction-band-minimum (CBM) is denoted as  $\Sigma$ .

Table 3.1. Electronic band gap (eV) for bulk MoS<sub>2</sub>, bilayer MoS<sub>2</sub> and SLMoS<sub>2</sub>.

	Bulk MoS <sub>2</sub>	Bilayer MoS <sub>2</sub>	SLMoS <sub>2</sub>	Folded SLMoS <sub>2</sub>
Present calculation	0.99	1.2	1.81	0.43-1.05
Experiments	1.23 [24] 1.29 [141]	1.6 [24]	1.8 [24] 1.83-1.98 [21], [141]	-
Numerical simulations	1 [21] 1.29 [11]	1.89 [11] 1.2 [142] 1.09 [143]	1.78 [144] 1.57 [142] 1.9 [12] 1.79 [124]	-

Removing one layer in going from the bilayer to SL MoS<sub>2</sub>, the electronic band structure undergoes an indirect-to-direct transition such that in the single layer the VBM and CBM are both located at the K point with the gap increasing to 1.81 eV, whose value is confirmed both by experiment [24] and numerical simulations [124, 144]. Experimentally, the electronic band gap of flat SLMoS<sub>2</sub> has been measured to be 1.83-1.98 eV [21, 24]. This compares to the presently calculated direct gap of 1.8 eV.

Upon folding, the direct band gap located at the  $K$  point transitions back to a smaller indirect band gap as shown in Figure 3.7. The gap after folding is sensitive to the length of sheet that was folded, yielding gap values ranging from 0.43 eV to 1.05 eV among the configurations we examined. The CBM does not change as a function of  $2L$  and are all located at  $\Sigma_{min} = 0.35 \times 2\pi/a$ . The VBM is located at  $\Sigma_{max} = 0.15 \times 2\pi/a$  for smaller sheet lengths, and is located at the  $\Gamma$  point for larger lengths.

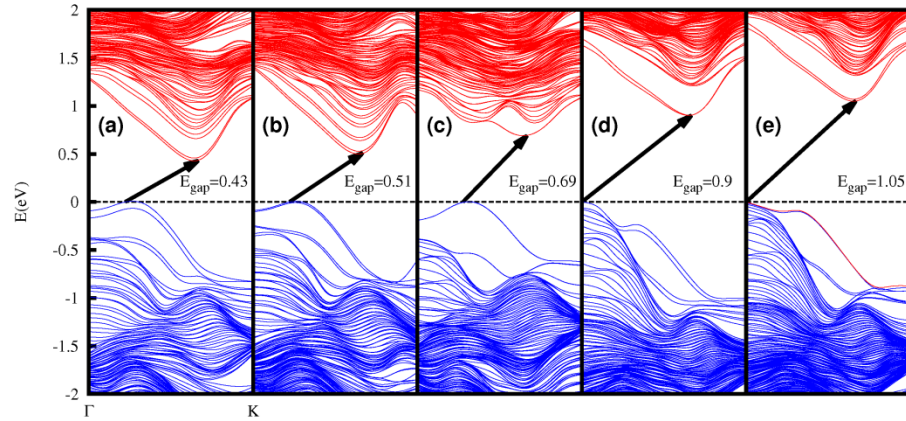


Figure 3.7. Electronic band structure of folded SLMoS<sub>2</sub>. (a)  $2L = 149.9 \text{ \AA}$ . (b)  $2L = 192.8 \text{ \AA}$ . (c)  $2L = 235.6 \text{ \AA}$ . (d)  $2L = 278.4 \text{ \AA}$ . (e)  $2L = 310.6 \text{ \AA}$ . The high symmetry direction  $\Gamma \rightarrow K$  corresponds to the zigzag direction in real space.

The calculated indirect band gaps appear to converge monotonically to the bilayer gap value with increasing size. The trend is depicted in Figure 3.8. With increasing system size ( $2L$ ), the configuration of the folded region stays invariant while the ratio between sizes of the flat and folded regions decreases. This indicates the fold is associated with local states and when  $L_{fold}/L_{flat}$  reaches approximately 0.53 we reach the largest gap among the finite-length folded sheets currently studied. The suggestion is that in the limit as size of the fold becomes vanishingly small relative to the bilayer region, the bilayer gap will be recovered.

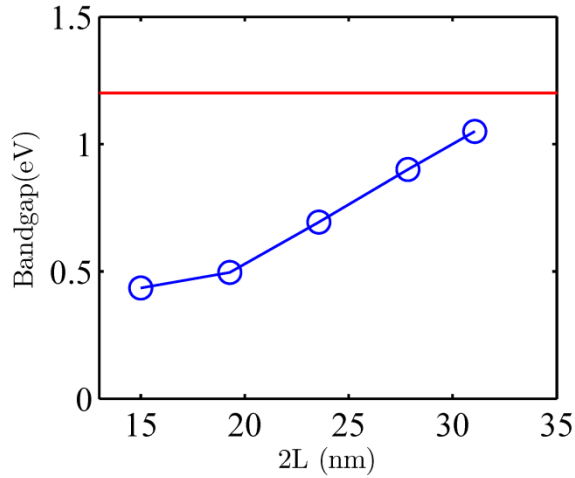


Figure 3.8. Calculated electronic band gap as a function of wrap length of folded SLMoS<sub>2</sub>. The value for the infinite bilayer is shown as a horizontal line.

### 3.3.3 Thermal conductivity and Phonons.

Phonon dispersion curves of bulk MoS<sub>2</sub>, bilayer MoS<sub>2</sub> and SLMoS<sub>2</sub> are shown in Figure 3.9. Bulk MoS<sub>2</sub> has 9 atoms in its unit cell, thus having 18 phonon modes among which 3 are acoustic modes while other 15 are optic modes. Due to the inversion symmetry of bulk MoS<sub>2</sub>, all the phonon modes are split into two branches. And since the interaction

between two SLMoS<sub>2</sub> layers in bulk MoS<sub>2</sub> is weak, the splitting is very low. So when reduced to bilayer, the splitting is almost gone and in SLMoS<sub>2</sub> which only has 3 atoms per unit cell, there is no splitting. Overall, phonon dispersion curves of bulk, bilayer and single-layer MoS<sub>2</sub> share a resemblance.

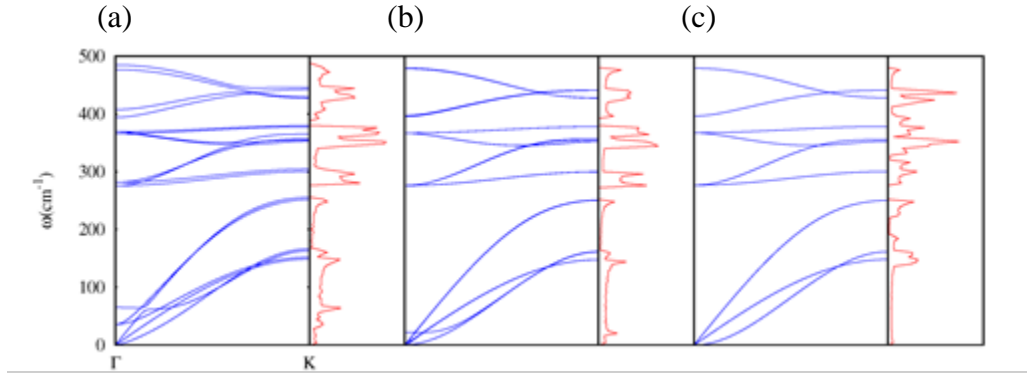


Figure 3.9. Phonon dispersion curves and densities of states of (a) bulk MoS<sub>2</sub>. (b) bilayer MoS<sub>2</sub>. (c) SLMoS<sub>2</sub>.

The phonon dispersion curves and densities of states (DOS) of folded SLMoS<sub>2</sub> with variable wrap length are shown in Figure 3.10. A band gap is present in all of the cases starting at around 242 cm<sup>-1</sup> of size 28 cm<sup>-1</sup>. We can observe a relatively small sensitivity of the gap size to wrap length where the gaps for the largest and smallest wrap lengths differ by about 10%. The calculated lattice specific heats, in units of  $Nk_B$ , differ little among the different forms - bulk, bilayer, SL, and folded - as shown in Table 3.2. The largest value is observed for the single layer which is consistent, when used with the phonon gas model, with the observations that single layer transport is improved over multiple-layers [38]. This effect is seen in the dispersion curves where there is increasing degeneracy and the lowering of frequencies of some of the branches at  $\Gamma$  as one goes from the bulk to the single layer. The lowering of the frequency of a mode increases its relative

contribution to the overall specific heat due to the dependence of the latter on the monotonically decaying function  $x^2 \exp(x)/[1 - \exp(x)]^2$  where  $x = \hbar\omega/k_B T$ . In the folded configuration, the specific heat of all of the folds that were studied was consistently around  $2.52 Nk_B$  which is only moderately higher than the corresponding value in the bulk. This insensitivity to sheet length, coupled with the observation that the folded structure is also insensitive to length, suggests that the specific heat per unit length of fold is an intrinsic property of MoS<sub>2</sub>.

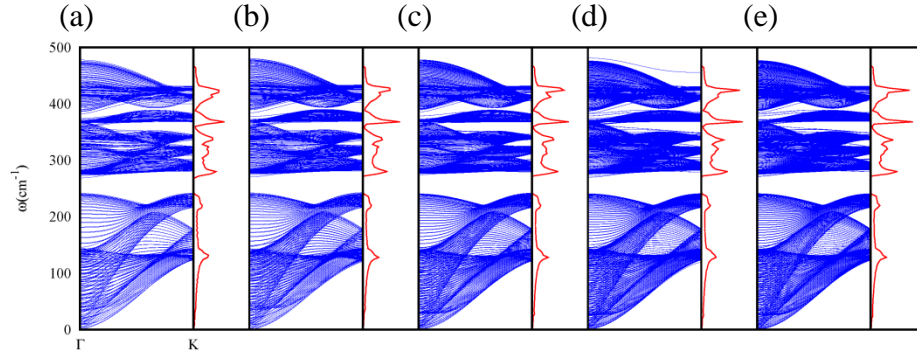


Figure 3.10. Phonon dispersion curves and densities of states of folded SLMoS<sub>2</sub>. (a)  $2L = 149.94 \text{ \AA}$ . (b)  $2L = 192.76 \text{ \AA}$ . (c)  $2L = 235.6 \text{ \AA}$ . (d)  $2L = 278.44 \text{ \AA}$ . (e)  $2L = 310.58 \text{ \AA}$ .

Table 3.2. Specific heat, phonon relaxation time, phonon group velocity, phonon mean free path and thermal conductivities.

	Bulk	Bilayer	SLMoS <sub>2</sub>	2L=149.94	2L=192.76	2L=235.6	2L=278.44	2L=310.58
$C_v(Nk_B)$	2.48337	2.49304	2.69225	2.52198	2.51942	2.52033	2.52138	2.52092
$\tau(\text{ps})$	23.75	19.09	23.25	7.91	10.01	11.8	8.65	8.55
$V(\text{m/s})$	621.16	731.16	800.08	663.2	704.78	713.27	664.24	729.34
$\Lambda(\text{nm})$	14.75	13.96	18.60	5.24	7.06	8.42	5.74	6.23
$\kappa(\text{Wm}^{-1}\text{K}^{-1})$	$75.37 \pm 2.16$	$84.26 \pm 3.74$	$132.68 \pm 4.67$	$24.74 \pm 2.62$	$35.89 \pm 3.79$	$44.71 \pm 5.32$	$26.29 \pm 3.67$	$31.45 \pm 4.31$

The insensitivity to length carries over to thermal conductivity which was determined using both Debye phonon integration from lattice dynamics and the Green-

Kubo method using molecular dynamics. The thermal conductivities of bulk, bilayer, and single-layer forms are summarized in Table 3.3; the Green-Kubo method is consistently in the range of 24.74~44.71  $\text{Wm}^{-1}\text{K}^{-1}$ . This compares to the estimates for bulk, bilayer, and single layer of  $75.37 \pm 2.16$ ,  $84.26 \pm 3.24$  and  $132.68 \pm 4.67$   $\text{Wm}^{-1}\text{K}^{-1}$  respectively. The effect of folding is a significant reduction in thermal conductivity of over 60% relative to the flat single layer value and, like the specific heat, conductivity is insensitive to the size of the sheet along the wrap axis once the fold has been created. The estimated thermal conductivity at 300 K along the fold axis (zigzag) as a function of sheet length is shown in Figure 3.11. By analyzing heat autocorrelation function from MD simulations we obtain single phonon RTs for bulk, bilayer, SL and folded  $\text{MoS}_2$ , as shown in Table 3.2. The relaxation times of folded configurations of  $\text{MoS}_2$  are around 10 ps, almost 50% of the values in flat  $\text{MoS}_2$  systems which are around 20 ps. A smaller phonon relaxation time implies a faster rate at which heat current decays and stronger phonon scattering. We also compute and present the average phonon group velocity and phonon MFP in Table 3.2. We see the same trend as in thermal conductivity that phonon mean free paths of the folded sheet are smaller than  $\text{SLMoS}_2$ , and also insensitive to the wrap length. We attribute the substantial decrease in thermal conductivity to increased anharmonic phonon scattering brought by the fold. Furthermore, the break in symmetry and the ensuing highly distorted bonds that drive the low energy-high group velocity modes to higher energies and reduce viable transverse modes along the fold axis also have the effect of frustrating heat carriers.

Table 3.3. Thermal conductivity ( $\text{Wm}^{-1}\text{K}^{-1}$ ) of bulk  $\text{MoS}_2$ , bilayer  $\text{MoS}_2$ ,  $\text{SLMoS}_2$  and folded  $\text{SLMoS}_2$ .

	Bulk MoS <sub>2</sub>	Bilayer MoS <sub>2</sub>	SLMoS <sub>2</sub>	Folded SLMoS <sub>2</sub>
Present calculation	75.37±2.16	84.26±3.24	132.68±4.67	24.74~44.71
Experiments	52 [32] 0.4-1.59 [145], [146] 85-112 [147] ~1.5 [148]	77±25 [45]	34.5±4 [31] 84±17 [45]	-
Numerical simulations	98 [38] 99.1 [149]	108 [38]	23.2 [150] ~5 [134] 138 [38] ≥83 [39] 1.35 [151]	-

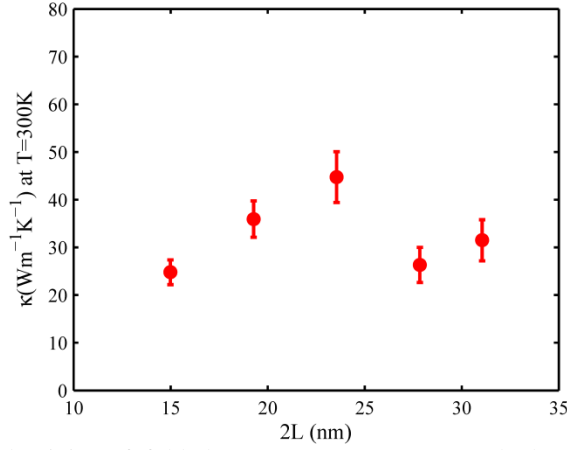


Figure 3.11. Thermal conductivity of folded SLMoS<sub>2</sub> at T=300 K calculated by Green-Kubo method. Thermal conductivity of folded SLMoS<sub>2</sub> is considerably smaller than thermal conductivity of SLMoS<sub>2</sub>.

### 3.4 Summary

We have shown that folding can evoke unique thermal and electronic properties with clear directionality in MoS<sub>2</sub> relative to its bulk, bilayer, and single layer forms. In this study we examined in SLMoS<sub>2</sub> the effect of folding and wrap length on physical, electronic, and phonon structures. Using multiple modeling techniques, the fold structure and dimensional features are determined to be independent of wrap length. A fold created

by wrapping the armchair axis in SLMoS<sub>2</sub> onto itself will produce a loop feature that is 5-5.6 nm. The electronic band gap showed clear modulation as a function of wrap length approaching the gap value for the bilayer structure monotonically from below. The size of the gap could be modulated by almost 50% by adjusting the wrap length used in the fold. On the other hand, thermal properties, while sensitive to folding by as much as 60% in reducing thermal conductivity, were remarkably insensitive to wrap length once the fold is formed. These observations suggest a promising route for device material designs involving MoS<sub>2</sub> that simultaneously permits directed breaking of symmetry that modulates electronic band structures while holding thermal properties fixed.

## **Chapter 4 Temperature-dependent phonons in 1T-HfS<sub>2</sub>: a first-principle study under quasi-harmonic approximation**

The main content of this chapter appeared in the Journal article: Peng, Jie, Sina Najmaei, Madan Dubey, and Peter W. Chung. "Dominant ZA phonons and thermal carriers in HfS<sub>2</sub>." *Journal of Applied Physics* 126, no. 16 (2019): 164302. Permission from [152] © 2018 Springer Nature

### **4.1 Introduction**

In recent years, TMDCs have attracted significant interest due to their unique electronic [14], optoelectronic [153], and catalytic [154] properties. MoS<sub>2</sub> is one of the most widely studied TMDC material, thanks to its natural abundance and sizable electronic bandgap making it a potential alternative to gapless graphene [155]. However, the relatively low mobility and heavy electron effective mass limit its applications [156]. Recent studies have shown that HfS<sub>2</sub> exhibits many promising properties. Its room-temperature mobility has been calculated to be 1833 cm<sup>2</sup>V<sup>-1</sup>s<sup>-1</sup>, much higher than 340 cm<sup>2</sup>V<sup>-1</sup>s<sup>-1</sup> of MoS<sub>2</sub> [157]. It has a finite bandgap of 1.2 eV [13]. Theoretical estimates of the current density of HfS<sub>2</sub>-based tunneling FET can be almost 100 times higher than that of MoS<sub>2</sub> [158]. Additionally, the unique c-axis electron transport and anisotropy in the electronic properties of HfS<sub>2</sub> promises new device applications [57]. Furthermore, ultrathin HfS<sub>2</sub> phototransistors have been fabricated with high on-off current ratio, photoresponsivity, and photogain [159]. Kanazawa et al. have also fabricated few-layer

HfS<sub>2</sub> transistors and found the drain current can be as high as  $0.75 \text{ mA}/\mu\text{m}$ , compared to the maximum value of  $0.5 \text{ mA}/\mu\text{m}$  for a MoS<sub>2</sub> FET [160].

In contrast to the large number of studies on the electrical and optical properties of HfS<sub>2</sub>, only few have focused on its thermal properties despite the important role they play in the stability and functionality of nano-electronic devices. Several problems pertaining to the thermal properties of HfS<sub>2</sub> are largely unanswered and are of primary interest. First, although it is generally known that thermal conductivities of TMDCs are highly anisotropic, due to the weaker interlayer VDW interactions compared to the planar covalent bonds [35], the underlying anisotropic thermal transport mechanism in HfS<sub>2</sub> has not yet been explored. Existing efforts for treatment of HfS<sub>2</sub> phonon and thermal properties have not gone beyond isotropic models [48]. It is therefore important to develop accurate models that incorporate the structural and phonon anisotropy intrinsic to the HfS<sub>2</sub> crystal. Secondly, the determination of the origins of phonon anisotropy through incorporation of the complete BZ is essential to a comprehensive understanding of thermal properties in HfS<sub>2</sub>. The actual contribution to phonon anisotropy can be a result of either intrinsic or extrinsic sources. The fundamental intrinsic anisotropy due to low symmetry of the bulk lattice can give rise to anisotropy of phonon dispersion and intrinsic scattering mechanisms. The latter is made evident by observing that Fermi's Golden Rule has a strong dependence on lattice structure [161]. Indirectly, however, the phonon dispersion anisotropy causes the group velocities to also be anisotropic, which can lead to anisotropy of related transport properties such as energy transfer rates and RTs. The extrinsic causes of anisotropy are surfaces or mesostructures that bring structural disorder to the pristine bulk or serve as a

scatterer. To understand these sources of anisotropy, one must have a complete BZ understanding of the phonons. Previous efforts primarily provide information at the BZ center  $\Gamma$  [52, 53, 54, 55] or point averages of the Grüneisen parameter  $\gamma$  over acoustic phonon modes [48]. Moreover, experimentally it has been shown that the long-range Coulomb interactions significantly affect the lattice dynamics at  $\Gamma$  of  $\text{HfS}_2$ , causing the splitting between longitudinal and transverse optical phonon frequencies (LO-TO splitting) [54, 55, 52]. Such splitting ultimately depends on the symmetry of the crystal structure, which also determines the phonon transport properties. The splitting is a marker for anisotropic phonon effects that can produce very long ranged fields enabling -- or even disabling -- a material's interesting properties. A theoretical quantification of the LO-TO splitting and  $\Gamma$  phonon properties in  $\text{HfS}_2$  would therefore help reveal the interplay between atomic interactions and lattice structure and suggest the presence of important long range fields.

In this work, we examine the thermal properties of  $\text{HfS}_2$  via a complete BZ DFT calculation. We show for the first time the underlying mechanism and the degree of anisotropy in phonon transport of  $\text{HfS}_2$  and demonstrate that a single phonon branch carries roughly 80% of the total heat in all three dimensions. This is extraordinary as it is the largest single phonon branch contribution to phonon transport known among TMDCs, and may open new opportunities for manipulating thermal properties in  $\text{HfS}_2$ . The remainder of this chapter is organized as follows. Section 4.2 provides a description of the approaches and computational details of the calculations. This is followed by the calculations of lattice structure and phonon properties at 0K in Sec. 4.3.1. In Sec. 4.3.2, we discuss the effect of

the coupling between the optical phonons and the electric fields generated by the atomic displacements on  $\Gamma$  phonon properties. The results for thermal properties at room temperature, including the Grüneisen parameters, the mode-dependent phonon group velocities, specific heats, RTs, MFPs, and thermal conductivities, are described in Sec. 4.4. The temperature dependence of the lattice structural and thermal properties is discussed in Sec. 4.4.4. Finally, we draw the conclusions in Sec. 4.5.

## 4.2 Computational Methods

### 4.2.1 DFT calculations

We employed DFT calculations using the Quantum Espresso code to perform our calculations of structural, phonon, and thermal properties of  $\text{HfS}_2$  [162]. For lattice structural optimization at 0K, we tested and compared three forms of the exchange-correlation functional - the LDA [163], the PBE-GGA [164], and an analytical form within the LDA (an-LDA) [165] - to find the pseudopotential that produces lattice parameters that agree best with other published values (see Table 4.1). The interlayer VDW interactions were modeled following the approach of Grimme [166]. A plane wave energy cutoff of 50 Ry was chosen while the first BZ was sampled with a  $10 \times 8 \times 8$  Monkhorst-Pack  $\mathbf{q}$  point mesh grid. The structural optimization was performed using analytical energy gradients with respect to atomic coordinates using the BFGS (Broyden-Fletcher-Goldfarb-Shanno) quasi-Newton algorithm for the Hessian update. Full relaxation was performed until the average force acting on the atom was less than  $1 \times 10^{-5}$  Ry/Bohr and the energy

difference between two consecutive relaxed configurations was less than  $1 \times 10^{-6}$  Ry. Convergence tests were performed to ensure no dependence of the lattice parameters and atomic coordinates on above parameters used in the DFT models.

All phonon calculations were performed using the DFPT. An  $8 \times 8 \times 8$  Monkhorst-Pack  $\mathbf{q}$  point mesh was used to calculate the dynamical matrices at these  $\mathbf{q}$  points, from which the force constant matrix was extracted. Then the dynamical matrix at any  $\mathbf{q}$  point in the BZ could be generated using the obtained force constant matrix. A total of 28117  $\mathbf{q}$  points in the BZ were chosen for calculating the phonon frequencies. The phonon group velocities, defined as the first derivative of the phonon frequency with respect to the wavevector, were calculated by a central difference scheme. The mode-dependent specific heat was calculated using Eq. (2.13).

#### 4.2.2 The Grüneisen parameters

The lattice directional Grüneisen parameter is calculated by Eq. (2.34) and Eq. (2.35). As the HfS<sub>2</sub> lattice has a hexagonal structure with two lattice parameters  $a$  and  $c$ , we have calculated three different Grüneisen parameters -  $\gamma_{\phi}^a$  (in-plane),  $\gamma_{\phi}^c$  (c-axis), and  $\gamma_{\phi}^V$  (volumetric). To generate the needed permutations in the structure, we applied homogeneous biaxial strains of  $\pm 0.4\%$  in the in-plane directions, uniaxial strains in the c-axis direction, and triaxial strains to determine  $\gamma_{\mathbf{q},j}^a$ ,  $\gamma_{\mathbf{q},j}^c$ , and  $\gamma_{\mathbf{q},j}^V$ , respectively. The Grüneisen parameters were calculated by taking the first derivative of phonon frequency with respect to the corresponding lattice parameter at equilibrium via a central difference scheme applied to Eq. (2.34) and (2.35).

### 4.2.3 Thermal expansion coefficients

The TECs are defined as

$$\alpha_i(T) = \frac{1}{a_i(T)} \frac{da_i(T)}{dT} \quad (4.1)$$

where  $i$  is the direction index. At temperature  $T$ , the equilibrium lattice configuration can be found by minimizing the Helmholtz free energy  $F(\mathbf{a}, T)$  with respect to all the lattice parameters  $\mathbf{a} = \{a_1, a_2, a_3\}$ . Under the QHA (see Sec. 2.1.2), the Helmholtz free energy can be expressed as the sum of the lattice ground state energy  $E_{GS}$  and vibrational energy  $F_v$ , as is shown by Eq. (2.17). The anharmonic effect brought by temperature is considered through lattice structural dependence of the phonon frequencies  $\omega_\phi(\mathbf{a})$ . The equilibrium lattice parameters can be obtained from  $\left. \frac{\partial F}{\partial a_i} \right|_T = 0$ , so that one can express the TECs using the Grüneisen parameters by [113]

$$\alpha_{jk} = \sum_{\phi} C(\omega_{\phi}, T) \sum_k \frac{S_{jk}}{V_0} \gamma_{\phi}^k \quad (4.2)$$

where  $S_{jk}$  are the components of the elastic compliance tensor. For a hexagonal lattice with two independent lattice parameters, the linear TECs are found to be [167]

$$\begin{bmatrix} \alpha_a \\ \alpha_c \end{bmatrix} = \frac{1}{M} \begin{pmatrix} G_{33} & -G_{13} \\ -2G_{13} & G_{11} + G_{12} \end{pmatrix} \begin{bmatrix} Y_a \\ Y_c \end{bmatrix} \quad (4.3)$$

where  $G_{mn}$  are the components of the elastic constant tensor,  $M = (G_{11} + G_{12})G_{33} - 2G_{13}^2$  and  $Y_{\beta}(T) = \sum_{\phi} \gamma_{\phi}^{\beta} C(\omega_{\phi}, T)$ . The elastic constants are determined by calculating the strain energy as a function of applied lattice strains and estimating the curvature of the energy vs strain relationship. Five different homogeneous and uniform strains were applied, where

the strain tensors and corresponding strain energies are  $(\delta, 0, 0, 0, 0, 0) \leftrightarrow \Delta E = \frac{1}{2}C_{11}\delta^2$ ,  
 $(\delta, \delta, 0, 0, 0, 0) \leftrightarrow \Delta E = \frac{1}{2}(C_{11} + C_{12})\delta^2$ ,  $(0, 0, \delta, 0, 0, 0) \leftrightarrow \Delta E = \frac{1}{2}C_{33}\delta^2$ ,  
 $(\delta, \delta, \delta, 0, 0, 0) \leftrightarrow \Delta E = \frac{1}{2}(2C_{11} + 2C_{12} + 4C_{13} + C_{33})\delta^2$ ,  $(\delta, 0, \delta, 0, 0, 0) \leftrightarrow \Delta E =$   
 $\frac{1}{2}(C_{11} + 2C_{33} + 2C_{13})\delta^2$ . (The six elements of the strain tensor represent strains along x,  
y, z, xy, xz, and yz directions, respectively). To generate multiple configurations along  
each direction, we used  $\delta = \pm 0.4\%$ ,  $\pm 0.3\%$ ,  $\pm 0.2\%$ , and  $\pm 0.1\%$ . Then, the calculated  
elastic constants, Grüneisen parameters, and specific heats are used in Eq. (4.3) to  
determine the TECs. The temperature dependent lattice parameters were calculated by  
integrating the TECs with respect to temperature.

#### 4.2.4 Phonon mean free paths, relaxation times, and thermal conductivities

The phonon RTs are calculated under the Klemens' theory (see Sec. 2.3.2.1).

The phonon MFP along different lattice orientations are calculated by

$$\Lambda_{\varphi}^{\alpha} = v_{\varphi}^{\alpha} \tau_{\varphi} \quad (4.4)$$

Then the thermal conductivity was calculated as a sum over a set of discrete  $\mathbf{q}$  points

$$\begin{aligned} \kappa^i &= \sum_{\varphi} \kappa_{\varphi}^i \\ &= \sum_{\varphi} C(\omega_{\varphi}, T) v_i(\omega_{\varphi}) v_i(\omega_{\varphi}) \tau(\omega_{\varphi}, T) \\ &= \sum_{\varphi} C(\omega_{\varphi}, T) \Lambda_i(\omega_{\varphi}, T) \Lambda_i(\omega_{\varphi}) \end{aligned} \quad (4.5)$$

In principle, all of the quantities in Eq. (4.5) are temperature dependent. However, this requires phonon calculations at every temperature that is of interest. To reduce computational cost, in this work we assume the phonon group velocities and Grüneisen parameters to be temperature independent and their values at 0K are used for all temperature dependent evaluations the terms in Eq. (4.5).

## 4.3 Results and discussion

### 4.3.1 Lattice structure of bulk $\text{HfS}_2$

$\text{HfS}_2$  crystallizes in the  $\text{CdI}_2$ -type lattice structure where one layer of hafnium atoms is sandwiched by two layers of sulfur atoms, which has the  $D_{3d}^3(P\bar{3}m1)$  space group symmetry, shown in Figure 4.1. The sandwiched layers of S-Hf-S are separated by a VDW gap between the adjacent S atom layers.

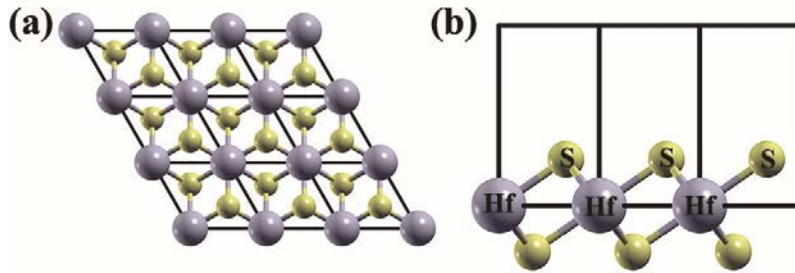


Figure 4.1. (a) Top view and (b) side view of the  $\text{HfS}_2$  lattice structure. Each  $\text{HfS}_2$  unit cell, represented by the black boxes, consists of one Hf atom and two S atoms. The figures are generated using the XCRYSDEN [168] program.

The calculated lattice parameters using all three pseudopotentials are compared with other published results (Table 4.1). Among all the DFT models, PBE+VDW yields the lattice parameters in closest agreement with experimental estimates. Values of the

lattice parameters in the literature are in the range  $a \in [3.60 \text{ } 3.655] \text{ \AA}$  and  $c \in [5.837 \text{ } 5.88] \text{ \AA}$ , whereas our calculated estimate of  $a$  using PBE+VDW falls within its range while  $c$  is 3% lower than the smaller value in its range. The inclusion of VDW correction terms in the PBE pseudopotential leads to a notable decrease in  $c$ , while  $a$  and Hf-S bond length are almost unaffected. This is because the lattice structural properties in the in-plane direction are dominated by covalent bonds that are much stronger than the interlayer VDW interactions.

Table 4.1. Lattice parameter  $a$  and  $c$  from experiments, numerical simulations, and this work.  $d_{\text{Hf-S}}$  represents the bond length between Hf atom and its nearest neighbor S atom.

	Methods		$a(\text{\AA})$	$c(\text{\AA})$	$d_{\text{Hf-S}}(\text{\AA})$
This work	LDA	no VDW	3.498	5.853	2.478
	an-LDA	no VDW	3.483	5.659	2.486
	PBE	no VDW	3.669	6.188	2.573
		VDW	3.653	5.654	2.562
Exp	[169]		3.635	5.837	
	[53]		3.622	5.880	
Num	[170]		3.640	5.860	
	[171]		3.655	6.932	
	[172]		3.635	5.837	
	[173]		3.600	5.840	

#### 4.3.2 Phonons, phonon normal modes, and LO-TO splitting

The primitive unit cell of  $\text{HfS}_2$  has three atoms with nine phonon branches, the first three of which are acoustic. The irreducible representations of  $\Gamma$  point vibrational modes are given as:  $\Gamma = A_{1g}(\text{R}) + E_g(\text{R}) + 2A_{2u}(\text{I}) + 2E_u(\text{I})$ , of which one  $A_{2u}$  and one  $E_u$  are acoustic modes [54]. We calculated the phonon dispersion curves and densities of states

(DOS) using the PBE models and further probe the effect of VDW correction on the phonon properties, as shown in Figure 4.2.

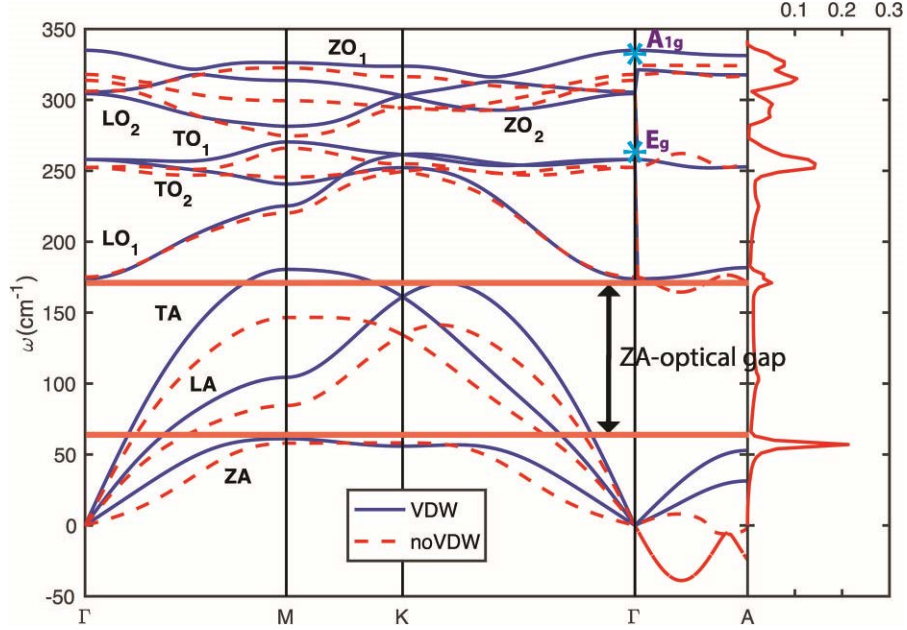


Figure 4.2. Phonon dispersion curves and density of states (DOS) of bulk  $\text{HfS}_2$  calculated using the PBE and PBE+VDW DFT models. The experimentally measured  $A_{1g}$  and  $E_g$  frequencies [52, 174] are marked by star symbols with a cyan color at  $\Gamma$ . DOS calculated by the PBE+VDW model is shown on the right as solid red lines. The high symmetry path  $\Gamma - M - K - \Gamma$  is in the xy plane, while  $\Gamma - A$  is along the c-axis in the reciprocal space. The nine phonon branches are represented by longitudinal acoustic (LA) and optical (LO), transverse acoustic (TA) and optical (TO), and out-of-plane acoustic (ZA) and optical (ZO) symbols. The subscripts “1” and “2” represent R-active and IR-active modes, respectively. The absence of a gap in the phonon spectrum, as shown in the phonon DOS, implies frequent scattering among the acoustic and optical branches and, consequently, a low thermal conductivity of  $\text{HfS}_2$ .

Phonon dispersion determined using PBE with no VDW shows negative frequencies along  $\Gamma A$ . This is consistent with the data shown in Table 4.1 where the bare PBE functional overestimates lattice parameter  $c$  by over 6%, leading to unphysical phonon dispersions along the c-axis direction whereas the in-plane parameter  $a$  only differs from the experimental values by around 1% and no negative frequency. Moreover, the inclusion of VDW correction terms leads to increases in most of the phonon frequencies due to increased atomic force constants brought by the additional energy terms. Based on the

results above, we have chosen the PBE+VDW model for subsequent calculations of thermal transport properties. The calculated frequencies of  $\Gamma$  phonon modes are listed in Table 4.2. Our results are in agreement with published results on  $E_g$  and  $A_{1g}$  mode frequencies.

Table 4.2. Comparison between  $\Gamma$  phonon frequencies calculated in present work and the ones from literature.

		$E_u(\text{LO})$	$E_u(\text{TO})$	$E_g$	$A_{2u}$	$A_{1g}$
Present work		305.42	171.7	256.95	305.42	338.71
Exp	[54]	318	166			
	[55]	318	166	$262 \pm 2$	$325 \pm 2$	$337 \pm 2$
	[52]	321	166	260	295	337
	[174]			260		337
Num	[175]	299	152	264	309	331

The well-known phenomenon of LO-TO splitting can be observed in the  $\text{LO}_1$  and  $\text{TO}_1$  branches at  $\Gamma$  in Figure 4.2. This is a breaking of degeneracy between longitudinal and transverse optical phonon modes in the long-wavelength limit. The split is a consequence of polarizability and an indication that the  $\text{HfS}_2$  has nontrivial, and possibly anisotropic, Born effective charge tensors. The long-range nature of the Coulombic interactions gives rise to macroscopic electric fields for LO phonons in the long-wavelength limit. The coupling between the electric fields and optical phonons alters the dispersion characteristics and leads to the splitting of the LO and TO modes. The energy of the split can be evaluated quantitatively using DFT, based on a linear response approximation [176]. This entails the determination of a modified Hamiltonian through a linear combination of the perturbations due to the collective atomic displacements and the associated electric fields. The frequency of a phonon mode that is affected by the electric fields can be calculated as the 2<sup>nd</sup> derivative of the Hamiltonian. Thus, the coupling effect can be quantified by breaking down the force constant matrix, from which the phonon frequencies

are calculated. In the limit  $\mathbf{q} \rightarrow 0$ , the force constant matrix elements can be split into a sum of analytic and nonanalytic contributions as [176, 177]:

$$\Phi_{bi,b'j}(\mathbf{q} \rightarrow 0) = \Phi_{bi,b'j}^{an}(\mathbf{q} = 0) + \Phi_{bi,b'j}^{nan}(\mathbf{q} \rightarrow 0) \quad (4.6)$$

where  $i$  and  $j$  here represent the direction index, not the atom index as in Chapter 2 and Chapter 3. The two terms,  $\Phi_{bi,b'j}^{an}(\mathbf{q} = 0)$  and  $\Phi_{bi,b'j}^{nan}(\mathbf{q} \rightarrow 0)$ , correspond to perturbations brought by the  $\Gamma$  phonons and the associated electric fields, respectively. The direction-dependent term  $\Phi_{bi,b'j}^{nan}(\mathbf{q} \rightarrow 0)$  takes the general form:

$$\begin{aligned} \Phi_{bi,b'j}^{nan}(\mathbf{q} \rightarrow 0) &= \frac{4\pi}{V} \frac{(\sum_l q_l Z_{b,li}^*)(\sum_{l'} q_{l'} Z_{b',l'j}^*)}{\sum_{ij} q_i \epsilon_{ij}^\infty q_j} \\ &= \frac{4\pi}{V} \frac{(\mathbf{q} \cdot \mathbf{Z}_b^*)_i (\mathbf{q} \cdot \mathbf{Z}_b^*)_j}{\mathbf{q} \cdot \boldsymbol{\epsilon}^\infty \cdot \mathbf{q}} \end{aligned} \quad (4.7)$$

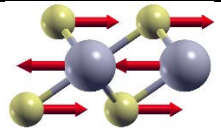
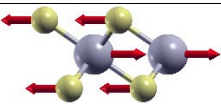
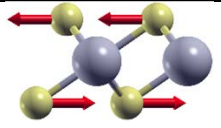
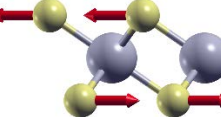
where  $Z_{b,li}^*$  is the Born effective charge tensor describing the force acting on an atom  $b$  along the  $i$ -direction induced by the electric fields, and  $\epsilon_{ij}^\infty$  is the dielectric permittivity tensor describing the electric fields generated by the atomic displacements. We have calculated the Born effective charge and dielectric permittivity tensors to be  $\mathbf{Z}_{Hf}^* = \begin{pmatrix} 6.057 & & \\ & 6.057 & \\ & & 1.945 \end{pmatrix}$ ,  $\mathbf{Z}_S^* = \begin{pmatrix} -3.046 & & \\ & -3.046 & \\ & & -0.969 \end{pmatrix}$ ,  $\boldsymbol{\epsilon}^\infty = \begin{pmatrix} 9.322 & & \\ & 9.322 & \\ & & 5.633 \end{pmatrix} \frac{e^2}{Ry \cdot Bohr}$ , where the in-plane isotropy and out-of-plane anisotropy are evident. Thus,  $\Phi_{bi,b'j}^{nan}(\mathbf{q} \rightarrow 0)$  clearly depends on the direction from which the wavevector  $\mathbf{q}$  approaches  $\Gamma$ .

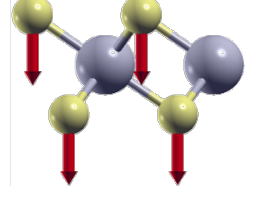
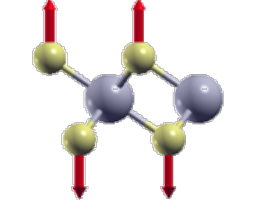
The LO-TO splitting phenomenon is also an indication that the in-plane and out-of-plane force constants have different impacts on phonon frequencies. The phonon frequencies calculated by diagonalizing the dynamical matrix  $\Phi_{b\alpha,b'\beta}(\mathbf{q} \rightarrow 0)$  with  $\mathbf{q}$  approaching  $\Gamma$  in the in-plane and c-axis directions, together with the visualized phonon modes are listed in Table 4.3. To first determine a reference zero-gap solution, we neglected the effect of the electric field by omitting the nonanalytic term in eq. (11) and obtained  $\omega[E_u(\text{LO})]=\omega[E_u(\text{TO})]=172 \text{ cm}^{-1}$ . Then, including the effect of the electric fields as  $\mathbf{q} \rightarrow \Gamma$  in the in-plane directions leads to a LO-TO splitting in the  $E_u$  mode ( $\omega[E_u(\text{LO})]-\omega[E_u(\text{TO})]=131.52 \text{ cm}^{-1}$ ), which has been observed in a number of experiments ( $152 \text{ cm}^{-1}$  [54, 55] and  $155 \text{ cm}^{-1}$  [52]). (The difference between our calculations and experiments is attributed to the error of the pseudopotential in DFT models that is amplified in the determination of LO-TO splitting using Eq. (4.6) and Eq. (4.7), since the LO-TO splitting value depends on Born effective charge and dielectric permittivity tensor that both require derivatives of the system Hamiltonian.) However, for  $\mathbf{q}$  approaching  $\Gamma$  in the c-axis direction, there is no LO-TO splitting in the  $E_u$  mode. Such contrasting behavior of the LO-TO frequencies can be more clearly understood by studying the force constant matrix. In the  $E_u$  mode, Hf and S atoms all vibrate in the in-plane direction. Thus, the mode frequencies are determined by the in-plane force constants. If we consider the term  $\Phi_{Hfx,Sx}^{nan}(\mathbf{q} \rightarrow 0)$  to represent the nonanalytic force constants only between Hf and S atoms in the x-direction, from (12) we see that

$$\Phi_{Hfx,Sx}^{nan}(\mathbf{q} \rightarrow 0) = \lim_{\mathbf{q} \rightarrow 0} \frac{4\pi}{V} \frac{q_x^2 Z_{Hf,xx}^* Z_{S,xx}^*}{q_x^2 \epsilon_{xx}^\infty + q_y^2 \epsilon_{yy}^\infty + q_z^2 \epsilon_{zz}^\infty} \quad (4.8)$$

from which it follows that  $\Phi_{Hfx,Sx}^{nan}(\mathbf{q}_{in-plane} \rightarrow 0) = \frac{4\pi}{V} \frac{Z_{Hf,xx}^* Z_{S,xx}^*}{\epsilon_{xx}^\infty}$  and  $\Phi_{Hfx,Sx}^{nan}(\mathbf{q}_{c-axis} \rightarrow 0) = 0$ . Therefore, the  $E_u$  mode frequency becomes  $\sim 304 \text{ cm}^{-1}$  due to the non-zero term added to force constants when  $\mathbf{q}$  approaches  $\Gamma$  in the in-plane direction while staying unchanged at  $172 \text{ cm}^{-1}$  when  $\mathbf{q}$  approaches  $\Gamma$  in the c-axis direction. Physically, the  $\mathbf{q}$ -dependent phonon frequency is due to the 2D planar structure and polar bonds in  $\text{HfS}_2$  that give rise to anisotropic Born effective charge and dielectric permittivity tensors.

Table 4.3. Phonon frequencies calculated from force constants representing the phonon perturbations [ $\Phi_{b\alpha,b'\beta}^{an}(\mathbf{q} = 0)$ ] and electric field perturbations associated with phonons with  $\mathbf{q}$  approaching  $\Gamma$  from in-plane [ $\Phi_{b\alpha,b'\beta}^{nan}(\mathbf{q}_{in-plane} \rightarrow 0)$ ] and c-axis [ $\Phi_{b\alpha,b'\beta}^{nan}(\mathbf{q}_{c-axis} \rightarrow 0)$ ] directions. The frequencies are in unit  $\text{cm}^{-1}$ . Visualizations of the phonon modes are shown in the right column where the red arrows indicate the atomic displacements.

	$\Phi_{b\alpha,b'\beta}^{an}(\mathbf{q} = 0)$	$\Phi_{b\alpha,b'\beta}^{nan}(\mathbf{q}_{in-plane} \rightarrow 0)$	$\Phi_{b\alpha,b'\beta}^{nan}(\mathbf{q}_{c-axis} \rightarrow 0)$	
$E_u(\text{LO})$	172	304	172	
$E_u(\text{TO})$	172	172	172	
$E_g(\text{LO})$	257	257	257	
$E_g(\text{TO})$	257	257	257	

$A_{2u}$	305	305	323	
$A_{1g}$	339	339	339	

To quantify the role of VDW interactions on the optical modes, we examine the frequencies of  $A_{1g}$  mode, which is the out-of-plane optical (ZO) mode, for SL and bulk configurations across different TMDCs. In the SL configuration, the intralayer interactions, simplified as an effective “spring” connecting two S layers in one trilayer, dominate the  $A_{1g}$  mode. Therefore, the frequency of ZO mode is expressed as  $\omega_{SL}^{ZO} = \sqrt{\frac{C_{intra}}{m_S}}$  where  $m_S$  is the mass of S atom and  $C_{intra}$  is the effective spring constant of the in-plane interactions. In bulk  $HfS_2$ , the VDW interlayer interactions introduce an additional effective “spring” between adjacent S layers, represented by  $C_{VDW}$ , resulting in a higher ZO mode frequency  $\omega_{bulk}^{ZO} = \sqrt{\frac{C_{VDW} + C_{intra}}{m_S}}$ . Combining above two frequencies, we define the ratio between the VDW and in-plane effective spring constants  $R_{VDW}$  by

$$R_{VDW} = \frac{C_{VDW}}{C_{intra}} = \left( \frac{\omega_{bulk}^{ZO}}{\omega_{SL}^{ZO}} \right)^2 - 1 \quad (4.9)$$

to be used as a fingerprint of the VDW interactions in  $HfS_2$ . Moreover,  $R_{VDW}$  can also be calculated for other types of 2D materials to measure the relative strength of the interlayer

VDW interactions with respect to the in-plane bonds. We listed  $R_{VDW}$  values of some typical TMDC materials in Table 4.4.

Table 4.4. ZO mode frequencies in bulk and SL 2D TMDC materials and  $R_{VDW}$  calculated from Eq. (4.9). In the schematic of the ZO mode, the red circles represent the atoms, the blue arrows represent the atomic displacements, the springs represent the effective VDW and in-plane interactions. (We note that the ZO mode frequency of a  $3\pm 1$ -layer ZrS<sub>2</sub> sample are taken as the  $\omega_{SL}^{ZO}$  value here [178]. However, we consider the difference between the A<sub>1g</sub> frequencies of 3-layer and SL ZrS<sub>2</sub> negligible since the frequency shows weak layer number dependence (going from 331.9 cm<sup>-1</sup> for a 3-layer sample to 332.45 cm<sup>-1</sup> for a 42-layer sample)).

	HfS <sub>2</sub>	ZrS <sub>2</sub> [178]	MoS <sub>2</sub> [179]	WS <sub>2</sub> [180]	WSe <sub>2</sub> [180]
$\omega_{bulk}^{ZO}(\text{cm}^{-1})$	338.71	$333.7\pm 0.3$	412	420.8	250.9
$\omega_{SL}^{ZO}(\text{cm}^{-1})$	320.31	$331.9\pm 1.3$	410.3	417.9	249.5
$R_{VDW}$	0.1182	0.0109	0.0083	0.0139	0.0113
Schematic of the lattice structure and ZO mode					

The  $R_{VDW}$  of HfS<sub>2</sub> is distinctively larger than other 2D TMDCs having similar lattice structures, indicating the relatively higher VDW-to-in-plane strength ratio in HfS<sub>2</sub>. Since the interlayer VDW interactions in these layer materials are tightly related to their structural and thermal properties, HfS<sub>2</sub> is expected to exhibit unique c-axis transport properties.

## 4.4 Phonon properties of HfS<sub>2</sub> at 300K

### 4.4.1 Group velocity and specific heat

The mode-dependent phonon group velocities and specific heats calculated for HfS<sub>2</sub> are shown in Figure 4.3. From Figure 4.3(a), it is seen that the group velocities are transversely isotropic. The anisotropy of phonon group velocities has already been shown to significantly affect thermal conductivity of VDW layered materials, usually manifesting in a much larger in-plane value than the c-axis value [181, 182]. Therefore, it is reasonable to anticipate a smaller thermal conductivity in the c-axis direction than the in-plane directions. Our calculated sound velocities in the long-wavelength limit for HfS<sub>2</sub> are 506 (ZA), 822.3 (LA), and 1357.1 m/s (TA), compared to 693.5 (TA) and 1108.8 m/s (LA) for single-layer (SL) MoS<sub>2</sub> [41] and 3743 (TA) and 5953 (LA) m/s for graphene [183]. The mode-dependent group velocities as a function of frequency are shown in Figure 4.3(b). The group velocities of acoustic modes are generally larger than the optical modes, except a few optical modes with frequency between 200 and 300 cm<sup>-1</sup> that have group velocities larger than the  $\Gamma$  acoustic modes. But Figure 4.3(c) shows that these high frequency optical modes have smaller specific heats than the low frequency acoustic modes at temperatures below 1000K. According to Eq. (2.19), a quantification of the mode-wise contribution towards the total thermal conductivity requires further information on the phonon RTs, which will be presented in Sec. 4.4.3.

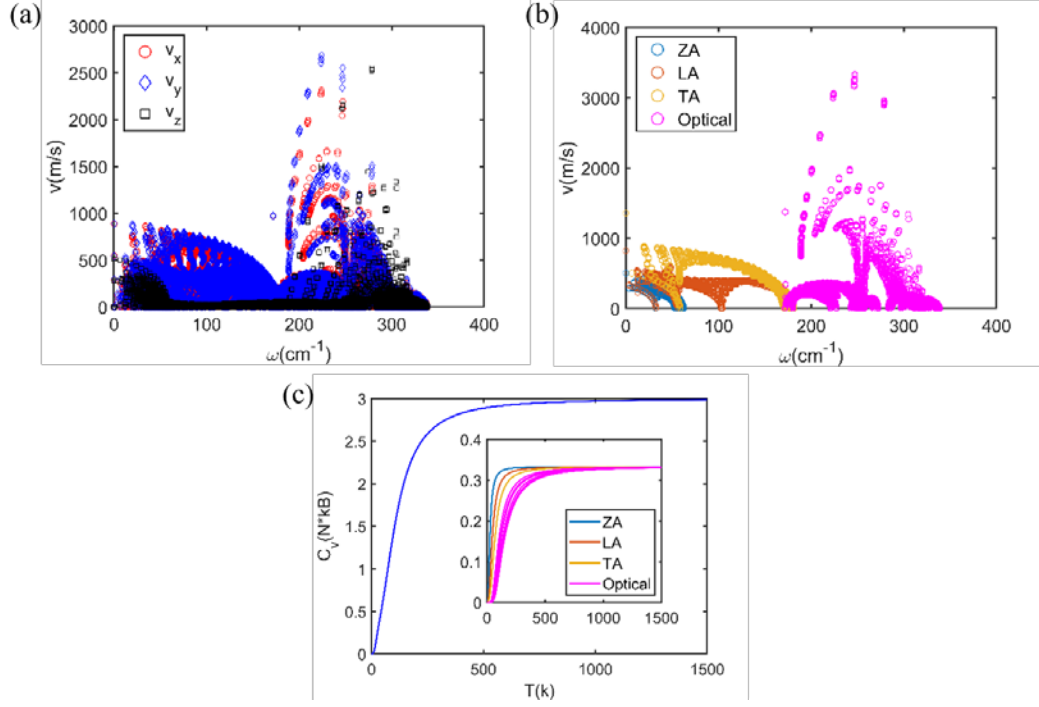


Figure 4.3. (a) Mode-dependent phonon group velocities along  $\mathbf{q}_x$ ,  $\mathbf{q}_y$  and  $\mathbf{q}_z$  directions. For the in-plane group velocities,  $v_x \approx v_y$  for almost all the phonon modes, so that the circle (red) dots are nearly all covered by the diamond (blue) dots, whereas the square (black) dots representing  $v_z$  have significantly smaller values (b) Magnitude of phonon group velocity VS frequency in the full BZ. (c) Specific heat VS temperature of  $\text{HfS}_2$ . The inset shows the branch-wise phonon specific heats. The acoustic branches have a larger contribution to the total specific heat than the optical branches at low T. As T increases, equipartition is gradually recovered.

#### 4.4.2 Grüneisen parameters

The mode-dependent Grüneisen parameters  $\gamma_a$ ,  $\gamma_c$ , and  $\gamma_V$  calculated from Eq. (2.34) and Eq. (2.35) are shown in Figure 4.4. Usually,  $\gamma$  is positive since the phonon frequency decreases as the force constants between atoms are reduced with the expanding lattice. In Figure 4.4(a)-(c), all three ZA mode Grüneisen parameters cross into the negative region. Negative  $\gamma$  for the bending mode ZA near  $\Gamma$  is common in 2D materials such as graphene [184], Si [185], and SL  $\text{MoS}_2$  [186] because of the coupling between XY and Z

vibrations caused by the orientation of the bonds between the metal and chalcogenide layers. Such coupling leads to hardened bending modes upon expansion, resulting in negative effective Grüneisen parameters. As has already been shown in Si and Ge [185], these negative  $\gamma$  modes lead to negative TECs according to Eq. (4.2). However, apart from the ZA modes, most of the other phonon modes in HfS<sub>2</sub> have positive  $\gamma$ . Therefore, the overall TECs are positive due to the relative dominance of the modes with positive  $\gamma$ . The detailed TECs results and discussions are compiled in Sec. 4.4.4.

The acoustic modes generally have larger Grüneisen parameters than the optical modes, suggesting that the acoustic modes are more sensitive to lattice deformations. It could be inferred that at higher temperature, the acoustic modes exhibit larger frequency shifts than the optical modes due to thermal expansion. Since all the components contribution to the thermal conductivity – phonon specific heat, group velocity, and  $RT$  – all depend on the phonon frequencies, such larger frequency shifts of acoustic modes are expected to manifest in greater sensitivity by the thermal conductivity to changes in temperature.

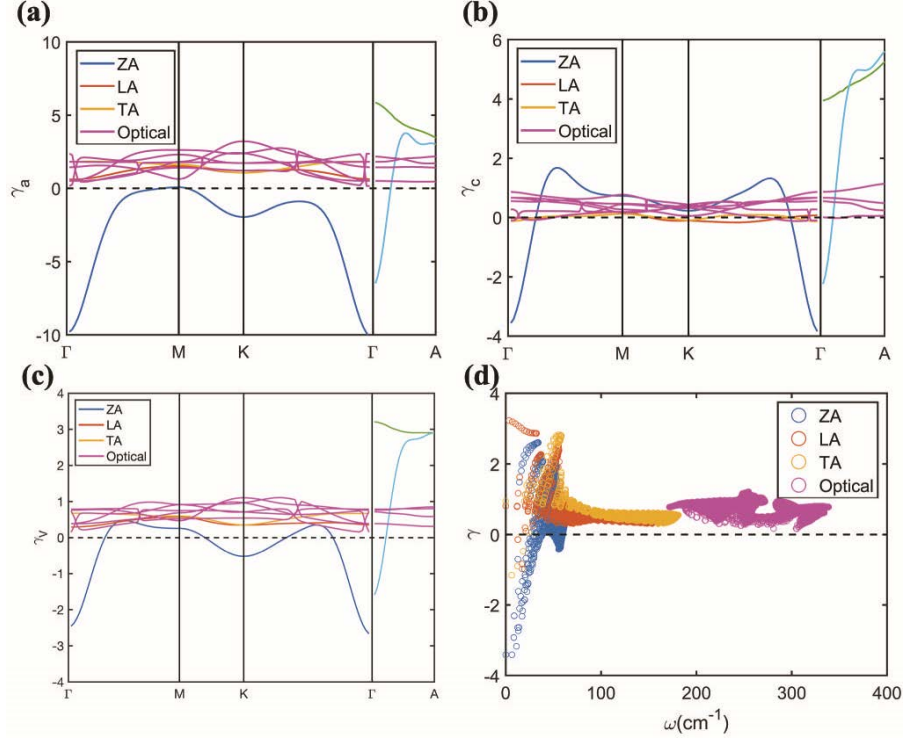


Figure 4.4. Gruneisen parameters (a)  $\gamma_a$  (b)  $\gamma_c$  (c)  $\gamma_v$  along high symmetry paths. (d)  $\gamma_v$  of all phonon modes in the BZ as a function of frequency. The volumetric Gruneisen parameter  $\gamma_v$  is used for subsequent calculations of RTs.

#### 4.4.3 Phonon relaxation time, mean free path, and thermal conductivity

In Figure 4.5, the mode-dependent phonon RTs and MFPs are shown. Eq. (2.37) is used to evaluate the RTs. However, in that expression,  $\tau$  of an individual mode is inversely related to the square of its frequency  $\omega$  and Gruneisen parameter  $\gamma$ . Therefore, a singularity occurs in  $\tau$  when  $\omega = 0$  or  $\gamma = 0$ . The case when  $\omega = 0$  for acoustic modes at  $\Gamma$  has been discussed for 2D semiconductors such as graphite [187] and MoS<sub>2</sub> [41], where an ad hoc small cutoff frequency  $\omega_c$  was defined below which smaller frequencies were simply not sampled to avoid the singularity. A study has shown that for most semiconductors, including phonons with frequencies higher than a cutoff value could

account for over 90% of the total thermal conductivity [188]. For a specific phonon branch, the cutoff value is chosen by finding the phonon of which the MFP is around 200 times smaller than the one at the BZ edge. Here, we utilize this method to choose the cutoff frequencies of  $\omega_c = 2.5$  (ZA), 4.5 (TA), and  $7.4 \text{ cm}^{-1}$  (LA) for three acoustic branches. The other cause of singularities in  $\tau$  are when  $\gamma = 0$ . A vanishing Gruneisen parameter implies the phonon frequency is unaffected by the lattice strains, or the vibrational energy is independent of lattice structural change. The statistical nature of phonons suggests that the probability is identically zero of finding a phonon mode exactly at the point in the BZ coinciding with  $\gamma = 0$ . Thus we can reasonably exclude modes with  $\omega = 0$  or  $\gamma = 0$  and calculate the mode-dependent RTs. These are shown in Figure 4.5(a)(b). The RTs of acoustic modes ZA, LA, and TA are generally larger than optical modes. For LA and TA modes, the RT decreases as the wavevector leaves  $\Gamma$  and reaches a low value at the BZ edges, while for the ZA mode, the RT reaches several peak values between  $\Gamma$  and BZ edges. The large RTs of these ZA modes are because they have  $\gamma$  values close to 0, as shown in Figure 4.4(c). A general trend of decreasing RT with increasing phonon frequency is seen from Figure 4.5(b), where  $\tau$  of all BZ phonons range from 0.1 ps to 0.1  $\mu\text{s}$ . The ZA modes with wavenumbers smaller than  $60 \text{ cm}^{-1}$  have substantially larger RTs than other modes, indicating a lower phonon scattering rate. This is due to the large ZA-optical phonon gaps, as shown in Figure 4.2, that hinder the energy transfer between the ZA and optical phonons whereas the LA-optical and ZA-optical phonon gaps are smaller, resulting in higher phonon scattering rates. Using these RTs, the phonon MFPs along three dimensions are calculated and shown in Figure 4.5(c)(d)(e) as a function of frequency. A very large

spectrum of MFPs is observed. The MFPs can be as small as  $10^{-15}$  nm for certain optical modes that have almost zero group velocities. The largest MFP of ZA modes is 1  $\mu\text{m}$ , which is significantly larger than the largest MFP in SLMoS<sub>2</sub> which is 18.1 nm [41]. This is because the smallest Grüneisen parameter in HfS<sub>2</sub> is  $\gamma \approx 0.005$  while the smallest in SLMoS<sub>2</sub> is  $\gamma \approx 1$ .

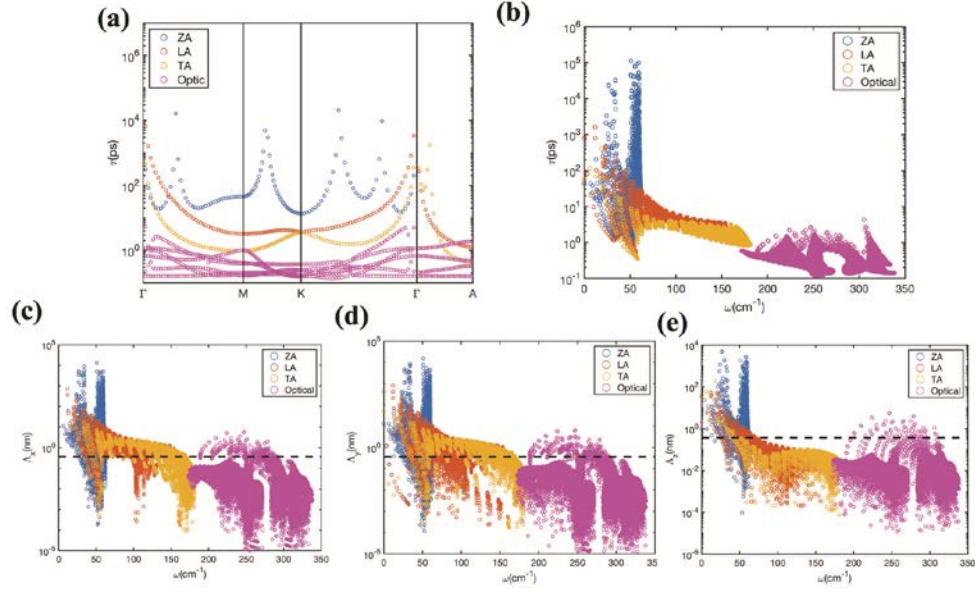


Figure 4.5. Mode-dependent phonon RTs for ZA, LA, TA, and optical modes (a) along the high symmetry paths (b) in the full BZ and phonon MFPs along (c) x- (d) y- (e) z-directions of HfS<sub>2</sub> at 300K. The dash line represents the lattice parameter  $a$  of HfS<sub>2</sub>. Despite the unrealistically small MFP ( $\approx 10^{-15}$  nm) for some optical modes, our results show that most of the optical modes have MFP smaller than the lattice parameter, thus having negligible contribution ( $<1\%$ ) to the total thermal conductivity. Therefore, we replace the MFPs of these modes by the lattice parameter  $a$  for a more reasonable estimate of thermal conductivity.

The mode-dependent thermal conductivities are shown in Figure 4.6. Due to the small group velocities, low specific heats, and small RTs, most optical mode terms in the sum are smaller than  $10^{-5}$  W/m/K and therefore contribute negligibly. The acoustic mode terms, on the other hand, are several orders of magnitude larger. The branch-wise contributions were determined by summing mode-dependent thermal conductivities along

each branch. The results are summarized in Table 4.5 along with comparable literature values for SLMoS<sub>2</sub> and graphene. The ZA modes contribute 80.6% ( $\kappa_x$ ), 80.5% ( $\kappa_y$ ), and 76.5% ( $\kappa_z$ ) towards the total thermal conductivity. These numbers are significantly larger than those in SLMoS<sub>2</sub> or graphene. Graphene has larger ZA contributions than SLMoS<sub>2</sub>. This is due to the symmetry selection rule that only allows even numbers of ZA phonons to be involved in phonon-phonon scattering [51]. The one-atom thickness structure greatly restricts the phonon-phonon scattering between ZA and other phonon modes in graphene [51] whereas the anti-symmetric trilayer structure of SLMoS<sub>2</sub> loosens such restriction. In HfS<sub>2</sub>, the large ZA-optical phonon gap, in contrast to no ZA-optical gap in graphene, further restricts the scattering of ZA modes, resulting in an even larger ZA contribution to the total thermal conductivity.

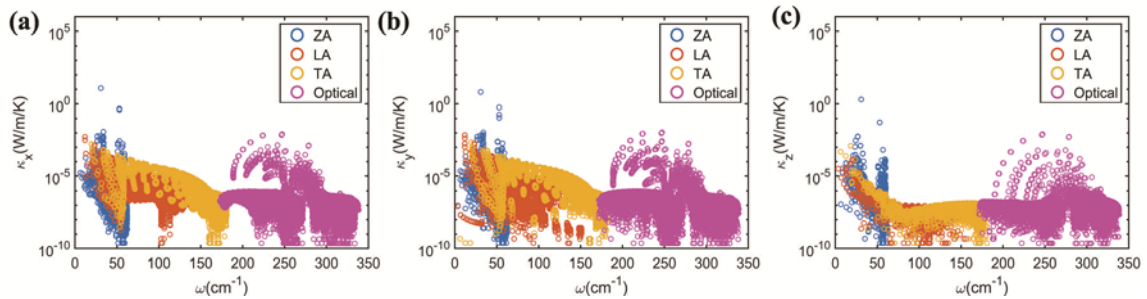


Figure 4.6. Mode-dependent thermal conductivities in (a) x-, (b) y-, and (c) z-direction of HfS<sub>2</sub> at 300K. There is no substantial difference among the thermal conductivity distributions along different lattice directions. The thermal conductivity decreases with increasing frequency, suggesting that the largest contribution towards the total thermal conductivity comes from the lowest frequency ZA modes.

Table 4.5. Calculated Phonon branch (ZA, LA, TA, and optical) contributions to total thermal conductivity of HfS<sub>2</sub> at 300K with analogous literature values for graphene and SLMoS<sub>2</sub>.

	ZA (%)	LA (%)	TA (%)	Optical (%)	Total (W/m/K)
HfS <sub>2</sub> ( $\kappa_x$ )	80.6	5.3	12.6	1.5	8.77
HfS <sub>2</sub> ( $\kappa_y$ )	80.5	5.6	12.4	1.5	8.73
HfS <sub>2</sub> ( $\kappa_z$ )	76.5	0.9	14.9	7.7	2.12
HfS <sub>2</sub> ( $\kappa_{in-plane}$ ) [48]					~9
SLHfS <sub>2</sub> ( $\kappa_{in-plane}$ ) [49]					~14

Graphene ( $\kappa_{armchair}$ ) [51]	76	15	8	1	~3500
SLMoS <sub>2</sub> ( $\kappa_{in-plane}$ ) [189]	29.1	30.4	39.1	1.4	101

The calculated in-plane thermal conductivities show good agreement with solutions from phonon BTE [48, 49]. The thermal conductivity and branch-wise contributions are almost identical along x- and y-directions, confirming the in-plane isotropy. The c-axis thermal conductivity is 4~5 times smaller than in-plane values. This is mainly attributed to smaller group velocities in the z-direction compared to the ones in the in-plane directions, as shown in Figure 4.3(a).

Table 4.6. In-plane and c-axis thermal conductivities of HfS<sub>2</sub> and other 2D materials. The anisotropy ratio  $R_{an} = \frac{\kappa_{c-axis}}{\kappa_{in-plane}}$ . The unit for thermal conductivities is W/m/K.

	HfS <sub>2</sub>	Graphene	MoS <sub>2</sub> [62]	WS <sub>2</sub> [63]	MoSe <sub>2</sub> [35]	WSe <sub>2</sub> [32]
$\kappa_{in-plane}$	8.77	1700~4100 [190]	105	124	35	42
$\kappa_{c-axis}$	2.12	~6 [7]	2	1.7	2.6	2.4
$R_{an}$	0.24	~0.003	0.02	0.014	0.074	0.057

To quantitatively evaluate the anisotropy of thermal conductance in HfS<sub>2</sub>, we summarize thermal conductivities of HfS<sub>2</sub> and other typical 2D materials in Table 4.6. The c-axis thermal conductivities of these 2D materials all have similar values (1~10 W/m/K). However, the anisotropy ratio  $R_{an}$  of HfS<sub>2</sub> is considerably larger than other 2D materials, due to its much smaller in-plane thermal conductivity. This observation is consistent with earlier discussions in Sec. 4.3.2 that the  $R_{VDW}$  is one order of magnitude larger than other TMDC materials, since the in-plane bonding strength in HfS<sub>2</sub> is much weaker.

#### 4.4.4 Temperature effect

The changing lattice structure, as calculated under the QHA, is the present means by which the temperature influences the physical properties. The calculated elastic constants are listed in Table 4.7 in comparison to experimental and DFT calculations from the literature and the TECs as a function of temperature are shown in Figure 4.7(a). Notably,  $\alpha_a$  is negative below 40K, and the lattice parameter  $a$  decreases by a negligible amount of  $1.31 \times 10^{-5} \text{\AA}$  from 0K to 40K. This is because at very low temperature, the excited phonon modes are primarily the low-frequency ZA modes. A number of ZA modes have negative Grüneisen parameter  $\gamma_a$ , as shown in Figure 4.4(a), leading to negative  $\alpha_a$  according to Eq. (4.2). At larger temperatures, more modes with positive  $\gamma_a$  are excited, and the  $\alpha_a$  becomes net positive. Both  $\alpha_a$  and  $\alpha_c$  increase with temperature and approach constant values of  $\alpha_a = 10.56 \times 10^{-6} \text{ K}^{-1}$  and  $\alpha_c = 7.66 \times 10^{-6} \text{ K}^{-1}$  at high temperature.

The temperature-dependent lattice parameters are shown in

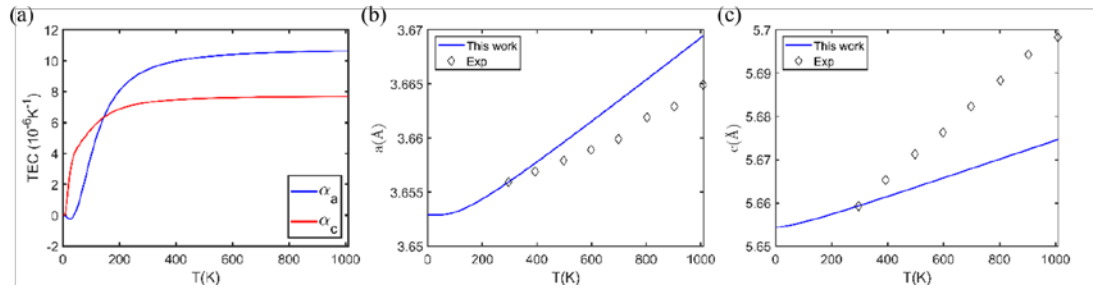


Figure 4.7(b)(c). Both lattice parameters  $a$  and  $c$  deviate from the experimental measurements. This is due to the harmonic phonon approximation in the QHA as described in Sec. 2.1.2. The Hamiltonian of a lattice at high temperature cannot be approximated only

to the second order and the higher order terms must be included. The missing higher order terms leads to inaccurate free energy surfaces at each temperature, resulting in inaccurate equilibrium lattice parameters and TECs. However, the QHA should be valid for relatively low temperature [191].

Table 4.7. Elastic constants and bulk modulus of HfS<sub>2</sub>. All values are in GPa.

	$G_{11}$	$C_{12}$	$G_{13}$	$G_{33}$	$G_{44}$	$G_{66}$	$B_0$
This work	186.12	48.5	15.35	56.18	25.67	68.79	44.5
Exp [192]	143( $\pm 7$ )	50( $\pm 15$ )	10( $\pm 1$ )	39.4( $\pm 1.4$ )	10.1( $\pm 0.4$ )		
DFT [193]	141.98	25.95	6.53	32.99	12.03	58.01	35.07

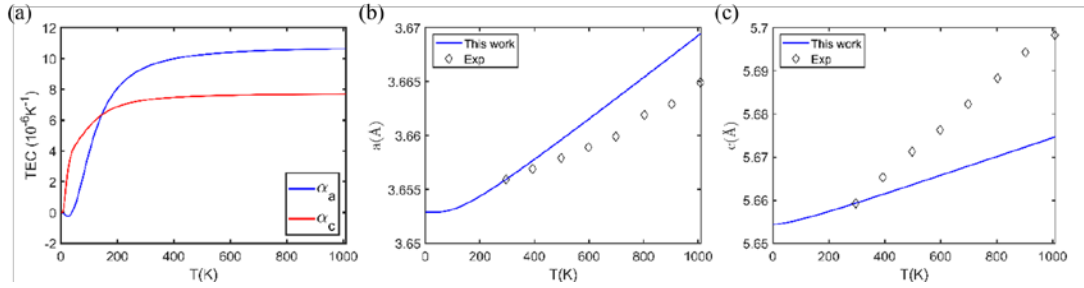


Figure 4.7. (a) TECs along  $a$  and  $c$  directions, lattice parameter (b)  $a$  and (c)  $c$  VS temperature of HfS<sub>2</sub>. The XRD experiment showed that HfS<sub>2</sub> decomposes to form HfO<sub>2</sub> at 735°C [194], therefore we limited the temperature to 1010K. In order to compare the temperature dependence rather than the absolute values, the experimentally measured lattice parameters have all been subtracted by a constant value which enforces them to agree with results of this work at room temperature.

In this work, the specific heats, phonon MFPs, and RTs are all temperature dependent. To illustrate the temperature effect more clearly, we take the average of the phonon MFPs and RTs over the full BZ by

$$\bar{\tau}(T) = \frac{\sum_{\varphi} C(\omega_{\varphi}, T) v^2(\omega_{\varphi}) \tau(\omega_{\varphi}, T)}{\sum_{\varphi} C(\omega_{\varphi}, T) v^2(\omega_{\varphi})} \quad (4.10)$$

$$\bar{\Lambda}_i(T) = \frac{\sum_{\varphi} C(\omega_{\varphi}, T) v_i(\omega_{\varphi}) \Lambda_i(\omega_{\varphi}, T)}{\sum_{\varphi} C(\omega_{\varphi}, T) v_i(\omega_{\varphi})} \quad (4.11)$$

so that the total thermal conductivity can be expressed as  $\kappa^{\alpha}(T) = C(T) \bar{\Lambda}_i(T) \bar{\tau}(T)$ . The results are shown in Figure 4.8. The initial increase of  $\bar{\tau}$ ,  $\bar{\Lambda}^{\alpha}$ , and  $\kappa^{\alpha}$  from 0K to around

30K are because more phonons are thermally excited to transport heat as temperature increases. However, phonon scattering – accounted for primarily in the RTs – starts to dominate thermal transport as temperature continues to increase, resulting in a continuous decrease starting at 30K. The components of the maximum thermal conductivity at 30K are  $\kappa_x = 61.2$  W/m/K,  $\kappa_y = 61.8$  W/m/K, and  $\kappa_z = 17.8$  W/m/K. As seen from Eq. (2.37), RT is inversely related to temperature as  $\tau \sim \frac{1}{T}$ . This is also presented in Figure 4.8(a). Despite that the specific heat  $C$  increases with  $T$ , this inverse relation to  $T$  is preserved in the total thermal conductivity as shown in Figure 4.8(c). Such similarity between the temperature dependence of  $\kappa$  and  $\tau$  further validates the dominant role phonon scattering plays over phonon population in thermal transport properties. The transverse isotropy of thermal conductivity is present at all temperatures, as seen from the agreement between the x and y values but contrast from the z value in Figure 4.8(c). The c-axis values are consistently around 4–5 times smaller than the in-plane values.

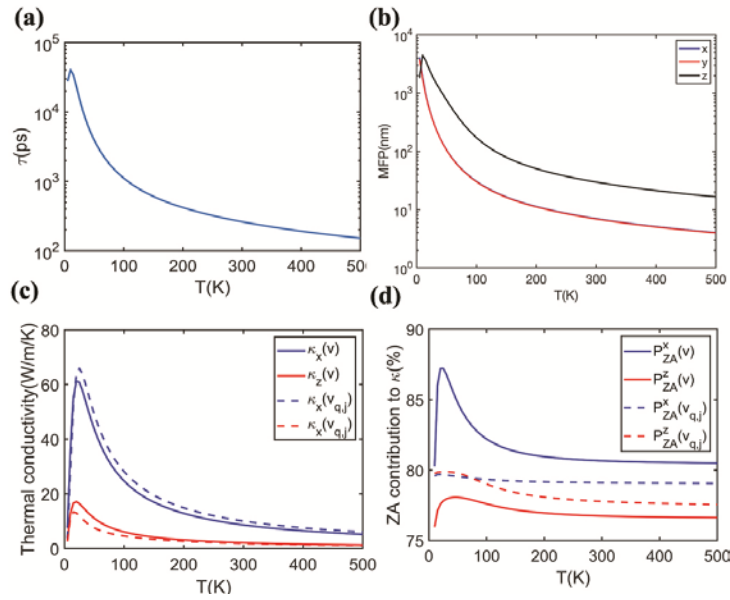


Figure 4.8. Temperature-dependent average (a) RT, three-dimensional (b) MFP, and (c) thermal conductivity. (d) Contribution from the ZA branch toward the total thermal conductivity of HfS<sub>2</sub>. In (c) and (d), the results calculated using Eq. (9) are marked with (v), while the ones from Eq. (10) are marked with (v<sub>qj</sub>).

The nearly 80% contribution from the ZA branch towards the total thermal conductivity is shown in Figure 4.8(d), where it can be seen this holds true at almost all temperatures along all three directions. Such dominance of the ZA phonon modes in thermal properties of HfS<sub>2</sub> is due to their larger specific heats [shown in Figure 4.3(c)], longer RTs (Sec. 4.4.3), and considerable group velocities [shown in Figure 4.3(b)] compared to other modes. Similar behavior has also been seen in WSe<sub>2</sub> that ZA phonons contribute 80% to the thermal conductivity at room temperature due to their longer RTs [47]. The fundamental cause of ZA phonon dominant thermal carriers in HfS<sub>2</sub> is attributed to the relatively weak interlayer VDW interactions leading to low vibrational frequencies of out-of-plane phonon modes and subsequently resulting in the large ZA-optical phonon gap shown in Figure 4.2. The scattering between ZA modes and optical modes is restricted by the large energy gap, whereas other branches have small or no phonon gaps, thus leading to frequent scattering. It is therefore evident that a close relation between the thermal transport properties and the phonon gap is dominant in HfS<sub>2</sub> phonon properties.

Furthermore, two forms of the relaxation time expression within the framework of Klemens' theory give similar thermal conductivity and ZA contributions. In Figure 4.8(c), Eq. (2.37) and Eq. (2.38) produce consistent results of temperature dependent thermal conductivity, despite slight difference in the absolute values. In Figure 4.8(d), the ZA contributions to thermal conductivity are all higher than 76% at all temperatures, using either Eq. (2.37) or Eq. (2.38).

## 4.5 Summary

In summary, we have explored the thermal properties of  $\text{HfS}_2$  using first principle DFT calculations of lattice structural and phonon characteristics. Our results, showing good agreement with experimental measurements, uncover important and distinctive properties of  $\text{HfS}_2$ . From the analysis of the out-of-plane optical modes at the  $\Gamma$  symmetry point, we discover that among other TMDCs,  $\text{HfS}_2$  has uncharacteristically strong out-of-plane VDW interactions relative to the in-plane bonds. This has significant effects on many phonon and thermal properties. The calculated mode-dependent Grüneisen parameters indicate an anomaly where specific ZA modes in  $\text{HfS}_2$  possess negative values caused by a hybridization between in-plane and out-of-plane atomic vibrations. Umklapp phonon scattering limited relaxation times and mean free paths are calculated to estimate the phonon transport properties and thermal conductivity of  $\text{HfS}_2$  in 0K to 500K temperature range. These are used to determine that large phonon populations and phonon gaps are associated with the ZA phonon modes, making them the overwhelmingly dominant mode for phonon transport. In fact, the ZA modes are found to be responsible for nearly 80% of the phonon contribution to the total thermal conductivity, highest among the TMDCs we considered. Additionally, a large crystal orientation dependent anisotropy in the thermal conductivity is found. The room temperature c-axis thermal conductivity of  $\text{HfS}_2$  is estimated to be 2.12 W/m/K and is 4-5 times smaller than the in-plane directions. Intrinsically, this is due to a weaker in-plane bonding strength in  $\text{HfS}_2$  compared to other 2D materials that leads to a smaller in-plane thermal conductivity. Our results outline some

of the fundamental and unique phonon characteristics of  $\text{HfS}_2$  that can be explored for controlling the thermal properties of the material in thermal management and thermoelectric devices.

## Chapter 5 Structural phase change and phonon stiffening in $\text{HfS}_2$

In Chapter 4, the thermal properties of  $\text{HfS}_2$  are studied under the QHA theory. The fundamental assumption in the QHA theory, as discussed in Sec. 2.1.2, is that phonons are still harmonic. However, this assumption would break down at high temperature or for materials with strong anharmonicity. It remains unclear whether the  $\text{HfS}_2$  phonons at finite temperature can be well represented under the QHA.

In this Chapter, we will present experimental and theoretical studies on the temperature dependent structural and phonon properties of  $\text{HfS}_2$ . Most remarkably, a structural phase transition at 300 K is discovered. Two unusual phenomenon are observed in the Raman and X-ray diffraction measurements on  $\text{HfS}_2$  from 80 K to 500 K. The first is that all the temperature coefficients of lattice parameters and phonon frequencies along both in-plane and c-axis orientation change at around 300 K. The second is that the c-axis phonon mode  $A_{1g}$  exhibits anomalous phonon stiffening below 300 K and reverses into phonon softening above 300 K. Based on the two observations, the hypothesis of a structural phase transition at 300 K is proposed. From the first-principle simulations, we observe the 3R phase ( $>300$  K) which is characterized by a different stacking order than the 1T phase ( $<300$  K). The temperature coefficients obtained from Car-Parrinello MD simulations agree with experimental measurements within 40%, thus supporting our hypothesis of phase transition. The anomalous phonon stiffening in  $A_{1g}$  mode is attributed to decreasing thickness of trilayers as temperature increases. By comparing first-principle

calculations adopting QHA and anharmonic approximation, the mechanism governing the phase transition is attributed to anharmonic phonon scattering that becomes more pronounced at high temperature. The discovered 3R phase, which can stabilize just above room temperature, would suggest a wide range of potential applications in electronic and optoelectronic devices.

## 5.1 Introduction

Transition-metal dichalcogenides (TMDCs) have attracted interests due to wide range of electronic, thermal, and optical properties they possess [16, 1]. They share common layered structures where one layer of M atoms is sandwiched by two layers of X atoms. Most widely known structures of TMDCs are characterized by trigonal prismatic (2H), octahedral (1T), or dimerized 1T (1T') coordination of the metal atom. Besides these commonly known phases, the so-called 3R phase also exists in some TMDCs such as MoS<sub>2</sub> [16, 195, 196], WS<sub>2</sub> [196], and MoTe<sub>2</sub> [197]. Distinguished from above central symmetric phases, the 3R phase can suppress the interlayer interaction and evoke strong valley polarization [198, 199]. In MoS<sub>2</sub> and WS<sub>2</sub>, the 3R phase has been shown to possess better catalytic properties towards the hydrogen evolution reaction than their 2H phase counterparts [196]. 3R phase TMDCs also show great potential in novel applications of nonlinear optics and valleytronics due to the high frequency conversion efficiency and strong spin-orbit coupling [200, 201].

In this chapter, we report the first discovery of 3R phase in HfS<sub>2</sub>, which can stabilize just above the room-temperature. This is enabled by the experimental and theoretical

studies of the structural and phonon properties of  $\text{HfS}_2$ . From Raman and X-ray diffraction measurements, a change in the temperature coefficients of lattice parameters and phonon frequencies are observed. In addition, in the c-axis  $A_{1g}$  phonon mode, we observe an anomalous phonon stiffening below 300 K that reverses to phonon softening above 300 K. Based on experimental observations, the hypothesis of structural phase transition is made. The hypothesis is supported by first-principle calculations performed. The mechanism governing the structural phase transition and phonon stiffening is attributed to lattice anharmonicity.

## 5.2 Experiments

All the figures and data shown in this section are produced by experiments performed by Dr. Sina. Najmaei and his research group from the Army Research Lab (ARL, Adelphi, Maryland).

We perform Raman spectroscopy and X-ray diffraction (XRD) measurements to examine the structural and phonon properties of  $\text{HfS}_2$ . The results are shown in Figure 5.1. Opposite temperature dependence between the in-plane ( $E_g$ ) and c-axis ( $A_{1g}$ ) phonon frequencies is observed below room-temperature. In Figure 5.1(b) and (f), below 300 K, the frequency of c-axis phonon mode  $A_{1g}$  frequency  $\omega_A$  increases as the temperature is raised. Normally, lattice expands as temperature increases. The thermal expansion leads to softened atomic bonds, thus resulting in a decrease of the phonon frequency or phonon softening. However, on the contrary, phonon stiffening is observed in the  $A_{1g}$  mode. On the other hand, the in-plane mode  $E_g$  exhibits normal phonon softening below 300 K, as

seen from Figure 5.1 (a) and (e). No prominent thickness dependence of the phonon stiffening and softening is observed from Figure 5.1(a) and (b). The anomalous phonon stiffening has also been observed in other materials such as  $\text{SiF}_3$  [202, 203] and  $\text{SnSe}$  [204]. The underlying mechanism is attributed to negative thermal expansion coefficients (TECs) that stiffen atomic bonds as temperature increases. However, no negative TEC is observed in  $\text{HfS}_2$ . As shown in Figure 5.1(c) and (d), both TECs  $\alpha_a$  and  $\alpha_c$  are positive from 120 K to 400 K. Since the phonon frequencies are determined by the lattice configurations, the observation of phonon stiffening indicates unusual change of atomic structure as a function of temperature below 300 K.

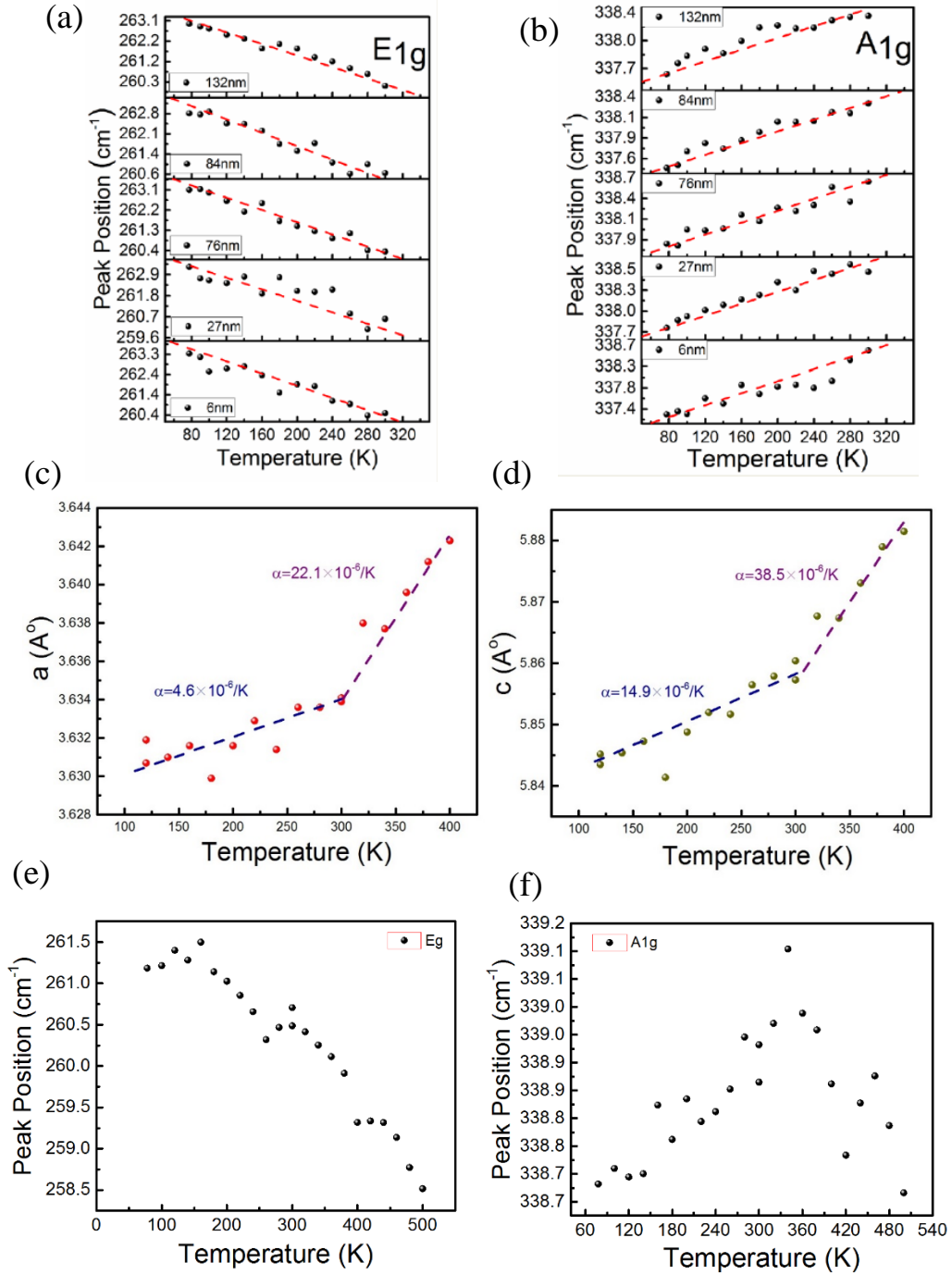


Figure 5.1. Measurements on phonon frequencies and lattice parameters of  $\text{HfS}_2$ . The scatters represent experimental data while the dash lines represent the linearly fitted curve. Temperature dependent Raman peaks of (a)  $\text{E}_{1g}$  and (b)  $\text{A}_{1g}$  modes for  $\text{HfS}_2$  samples with different thickness, in the temperature range [77, 300] K. Approximately linear dependence on temperature is observed. Considering the lattice parameter  $c$  of  $\text{HfS}_2$  is around 0.583-0.88 nm [53, 169], the thinnest sample in the experiments contains over 10 layers. Therefore, all the samples are deemed to be bulk  $\text{HfS}_2$ . XRD measured lattice parameters (c)  $a$  and (d)  $c$  of

HfS<sub>2</sub> samples with 300nm thickness. The TEC of lattice parameter  $a$  is calculated as  $\alpha_a = \frac{d\epsilon_a}{dt}$ . The strain is calculated as  $\epsilon_a = \frac{a(T)-a(0)}{a(0)}$  with  $a(0) = 3.622 \text{ \AA}$  (interception of the fitted curve with y axis, which is considered as lattice parameter  $a$  at 0K). The TEC of lattice parameter  $c$  is calculated using the same approach. Temperature dependent Raman peaks of (e) E<sub>g</sub> and (f) A<sub>1g</sub> modes for HfS<sub>2</sub> sample with thickness 300 nm in the temperature range [77 500] K.

We also observe that all the temperature coefficients of lattice parameters and phonon frequencies change at around 300 K. In Figure 5.1(c) and (d), both TECs  $\alpha_a$  and  $\alpha_c$  change at 300 K. Specifically,  $\alpha_a(T > 300K) \approx 4.8\alpha_a(T < 300K)$  and  $\alpha_c(T > 300K) \approx 2.6\alpha_c(T < 300K)$ . In Figure 5.1(e) and (f), temperature coefficients of A<sub>1g</sub> and E<sub>g</sub> phonon, namely  $\chi_A$  and  $\chi_E$  change at 300 K. Change in the TECs implies structural phase transition [205, 206].

Our leading hypothesis is that the experimental observations are due to a solid-to-solid structural phase transition that starts in the known 1T phase at low temperature (< 300K) and arrives at a yet-to-be-discovered phase at high temperature (>300K). In the 1T phase below 300 K, the c-axis phonon A<sub>1g</sub> exhibits anomalous phonon stiffening. In the new phase above 300 K, A<sub>1g</sub> exhibits phonon softening.

### 5.3 Theoretical calculations

To provide a theoretical explanation for the experimentally measured temperature dependence of structural and phonon properties, QHA (see Sec. 2.1.2) and CPMD (see Sec. 2.2.3) calculations are performed within the framework of the DFT theory.

### 5.3.1 QHA

Same DFT parameters as the ones used in Sec. 4.2.1 are adopted. The equilibrium lattice structure as a function of temperature is determined by performing phonon calculations at 25 lattice configurations with different lattice parameters  $a$  and  $c$ . Five values of  $a$  (from 3.458 Å to 3.958 Å with increment of 0.1 Å) and  $c$  (from 5.502 Å to 5.902 Å with increment of 0.1 Å) are chosen to generate the lattice configurations. The Helmholtz free energy of these configurations are calculated using Eq. (2.17). At a specific temperature, the calculated Helmholtz free energy are fitted to  $a$  and  $c$  as a third order polynomial. Then the parameters  $a$  and  $c$  of equilibrium lattice configuration is obtained by finding the minimum of the fitted function. We vary temperature from 0 K to 500 K with a 5 K interval.

### 5.3.2 CPMD

A series of CPMD simulations at temperature from 80 K to 500 K with 40 K increment are performed. In each simulation, a  $3 \times 3 \times 3$  HfS<sub>2</sub> supercell containing 81 atoms subject to periodic boundary condition is considered. A time step of 10 a.u. (1 a.u.=0.024189 fs) is used. The fictitious electron mass, i.e.  $\mu$  in Eq. (2.30) and Eq. (2.32), is set to be 800 a.u. (1 a.u is the electron rest mass,  $m_e = 9.109384 \times 10^{-31}$  Kg). The system is brought to thermal equilibrium at the target temperature via a sequence of different runs. Initially, we relax the system to ground state at 0 K. This is done by relaxing electrons, ions, and supercell DOFs to the minimum energy configuration. Convergence is achieved when the difference between total energy of two consecutive lattice

configurations is less than  $1 \times 10^{-6}$  Ry, all components of all forces acting on atoms are less than  $1 \times 10^{-3}$  Ry/a.u., and the kinetic energy is less than  $1 \times 10^{-5}$  Ry. Subsequently, a displacement is applied to every atom in the system to initiate a CP dynamics. The magnitude of the displacement is randomized between -0.01 and 0.01 a.u. (1 a.u.=0.5291772 Å). The initial velocities of all atoms are set to zero. Next, the system is heated up to the target temperature by a NPT run of 50 ps. A Nose-Hoover thermostat is implemented to keep the temperature of ionic system constant [207]. Finally, data are collected from simulations in NPT ensemble for over 200 ps, where the atomic trajectories are sampled every 10 timesteps.

## 5.4 Results and discussion

From the QHA and CPMD calculations, we extract temperature dependent phonon frequencies and lattice parameters to compare with the experimental data.

### 5.4.1 Structural phase transition

In the CPMD simulations, we observe a structural phase transition at 300 K. The equilibrium lattice configurations at different temperature are shown in Figure 5.2. They are obtained by taking the time average of atomic coordinates and supercell vectors from the NPT ensembles in CPMD simulations. At  $T < 300$  K, HfS<sub>2</sub> lattice stays as the commonly known 1T phase. However, as temperature approaches 300 K, the lattice experiences a structural phase transition. The new phase above 300 K is characterized by a shift between adjacent layers. The quantification of atomic coordinates indicates that each layer is shifted

with respect to the adjacent ones by  $(\frac{1}{3}\mathbf{x}_1, \frac{1}{3}\mathbf{x}_2, 0)$ , thus exhibiting a ABC stacking order. The ABC stacking order has been observed in other 2D layered materials. In trilayer graphene, it is found that the ABC (rhombohedral) stacking order is retained at high temperature ( $>800$  °C) and exhibits phonon and electronic properties different from those of the usual ABA (Bernal) stacking order [208, 209]. In MoS<sub>2</sub>, the ABC stacked (3R) phase also exists as well as the most stable AB stacked (2H) phase [198, 210]. Again, high temperature ( $\geq 850$  °C) is required for 3R-MoS<sub>2</sub> to stabilize. There are two prominent differences between the ABC stacked HfS<sub>2</sub> and other 2D layered crystals. First, ABC-HfS<sub>2</sub> can stabilize at much lower temperature ( $>300$  K) than the ones required by the other 2D crystals. This indicates that the energy barrier for structural phase transition in HfS<sub>2</sub> is significant lower than the values for 2D materials. Second, above ABC stacking phase are studied in trilayer or few-layer graphene and MoS<sub>2</sub> samples whereas in our work, bulk HfS<sub>2</sub> samples are considered. The first observation of ABC-HfS<sub>2</sub> in our work suggests a rout for exploring the effect of interlayer VDW interaction on phonon and electronic properties of HfS<sub>2</sub>. Similar work has already been done for MoS<sub>2</sub> and graphene [208, 198].

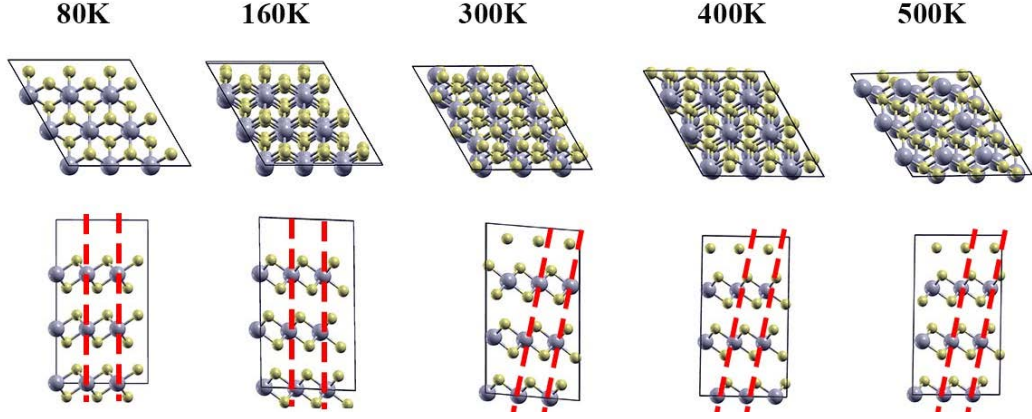


Figure 5.2. Equilibrium lattice configurations of  $\text{HfS}_2$  supercells at different temperature. The structural phase transition is characterized by a change in the stacking order between adjacent trilayers, as is denoted by the dash red lines.

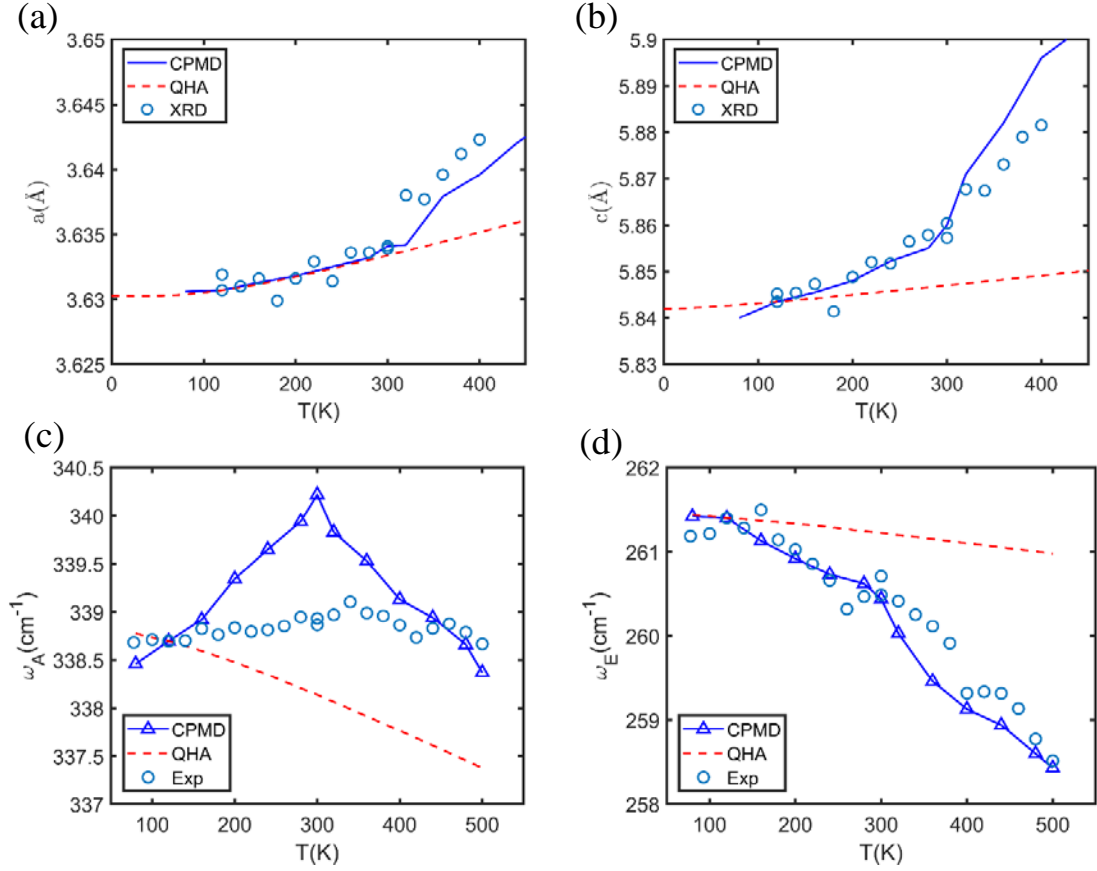


Figure 5.3. Temperature dependent (a) in-plane lattice parameter  $a$ , (b) c-axis lattice parameter  $c$ , (c)  $A_{1g}$  phonon frequency  $\omega_A$ , and (d)  $E_g$  phonon frequency obtained from theoretical calculations and experimental measurements. In all the figures, the simulation data has been subtracted by a constant number to match with experimental data at 120K, in order to compare the temperature dependence rather than absolute values. In

(b), the lattice parameter  $c$  of 3R-HfS<sub>2</sub> is obtained by taking one third of the supercell dimension along  $c$ -axis, since one supercell contains three unit cells along the  $c$ -axis direction.

The CPMD simulations also successfully reproduce the phonon stiffening and softening behavior of A<sub>1g</sub> and E<sub>g</sub> modes observed in experiments, as is shown in Figure 5.3(c) and (d). To quantitatively compare experimental and theoretical data, we extract the temperature coefficients of lattice parameters and phonon frequencies via linear fitting of all the data shown in Figure 5.3. The temperature coefficients are summarized in Table 5.1. Three out of four temperature coefficients calculated from CPMD approach -  $\chi_E$ ,  $\alpha_a$ , and  $\alpha_c$  - all agree with experimental data within 35%. The only exception is the temperature coefficient of A<sub>1g</sub> phonon frequency, which is 8 times (T<300 K) and 6 times (T>300 K) larger than the experimental value. However, qualitatively, the phonon stiffening (T<300 K) and softening (T>300 K) behavior are both successfully reproduced by the CPMD simulations.

Table 5.1. Temperature coefficients of lattice parameters ( $\alpha_a$  and  $\alpha_c$ ) and phonon frequencies ( $\chi_A$  and  $\chi_E$ ). The frequencies are fitted to a linear equation  $\omega(T) = \omega_0 + \chi T$  where  $\omega_0$  is the frequency at ground state and  $\chi$  is the temperature coefficient. The lattice parameters are fitted to a linear equation  $g(T) = g_0(1 + \alpha)T$  where  $g_0$  is the lattice parameter at ground state and  $\alpha$  is the temperature coefficient. The percentage difference between experimental and simulation data, calculated as  $\left| \frac{sim-exp}{exp} \right| \times 100\%$ , are shown in the square.

	T<300 K			T>300 K		
	Exp	CPMD	QHA	Exp	CPMD	QHA
$\chi_A(\text{cm}^{-1}/\text{K})$	0.0011	0.0082	-0.0034	-0.0013	-0.0077	-0.0034
$\chi_E(\text{cm}^{-1}/\text{K})$	-0.0043	-0.0046	-0.0011	-0.01	-0.0093	-0.0011
$\alpha_a(10^{-6}/\text{K})$	4.6	4.3 (-6.5%)	3.2 (-30.4%)	22.1	20.5 (-7.2%)	5.7(-74.2%)
$\alpha_c(10^{-6}/\text{K})$	14.9	9.4 (-36.9%)	3.4 (-77.2%)	38.5	50.6 (31.4%)	4.2 (-89.1%)

### 5.4.2 Lattice anharmonicity

The mechanism governing the structural phase transition from 1T to 3R phase is the more and more pronounced anharmonic phonon scattering as temperature increases. This is discussed in the following analysis on theoretical calculations. The lattice parameters  $a$  and  $c$  obtained from the QHA calculations, CPMD simulations, and XRD measurements are plotted in Figure 5.3(a) and (b). Both the in-plane and c-axis parameters calculated by the CPMD approach agree well with experimental data at all temperature. On the other hand, the values obtained from QHA calculations deviate from experimental measurements significantly. The difference between QHA and CPMD results can be understood from a free energy perspective. A stable phase of a crystal is always associated with minimum free energy under specified thermodynamic conditions. In the case of HfS<sub>2</sub> here, the Helmholtz free energy can be chosen which is given by [79]

$$\begin{aligned} F(\{a\}, T) &= E_{GS}(\{a\}) + F_V(\{a\}, T) \\ &= U_{HA}(\{a\}) + U_{AN}(\{a\}) + F_V(\{a\}, T) \end{aligned} \tag{5.1}$$

where  $\{a\}$  represents a set of lattice parameters defining the lattice configuration,  $T$  is the temperature,  $E_{GS}$  is the ground-state energy,  $F_V(\{a\}, T)$  is the vibrational energy,  $U_{HA}(\{a\})$  and  $U_{AN}(\{a\})$  represent the harmonic and anharmonic terms in the Taylor expansion of interatomic potential respectively. At any temperature, the equilibrium lattice configuration is the one with the lowest free energy  $F(\{a\}, T)$ . In QHA calculations, the anharmonic terms  $U_{AN}$  are completely neglected. Moreover, the lattice is ascribed with 1T phase under the QHA - only the variance of  $a$ ,  $c$ , and the internal atomic coordinates are

considered. No phase other than 1T is considered in QHA calculations. In CPMD simulations, all the anharmonic terms  $U_{AN}$  are considered without neglecting any higher order terms. Therefore, all degrees of freedom of the lattice configuration are allowed to relax and equilibrate in a thermodynamic ensemble. It is able to sample through all possible configurations and stabilize as the minimum energy configuration. As a result, it stabilize as 1T phase at  $T < 300$  K and ABC phase at  $T > 300$  K. The anharmonic terms  $U_{AN}(\{a\})$  at  $T > 300$  K leads to the fact that 3R phase is more thermally stable than 1T phase.

### 5.4.3 Phonon stiffening and bonding length

The anomalous phonon stiffening of  $A_{1g}$  mode can be explained by the temperature dependence of the bonding length. The intralayer ( $h$ ) and interlayer ( $h_{VDW}$ ) distances at different temperature, which are obtained by taking time average in CPMD simulations, are plotted in Figure 5.4. We can qualitatively express  $A_{1g}$  frequency as

$$\omega_{A_{1g}} = \sqrt{\frac{C_{VDW} + C_{intra}}{m_S}} \quad (5.2)$$

since  $A_{1g}$  phonon corresponds to atomic vibrations along c-axis direction (see Sec. 4.3.2).

We assume that the relations  $C_{VDW} \sim \frac{1}{h_{VDW}}$  and  $C_{intra} \sim \frac{1}{h}$  stand. This is because as the atomic bonds are stretched along c-axis direction, the bonding strength are decreased. Combining these relations with (5.2), we have a qualitative relation between  $\omega_A$  and layer distances as  $\omega_A \sim \frac{1}{h_{VDW}}$  and  $\omega_A \sim \frac{1}{h}$ . Furthermore, as the intralayer bonds are much stronger

compared to VDW interactions, therefore  $C_{VDW} < C_{intra}$ . The influence of  $h$  on  $\omega_{A_{1g}}$  is more prominent than  $h_{VDW}$ .

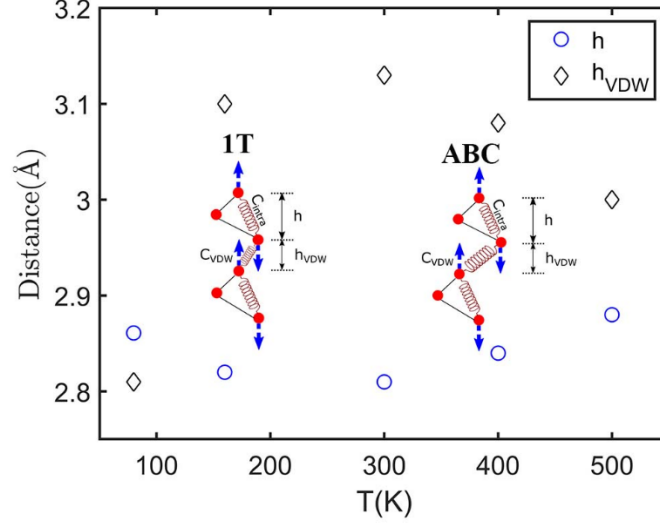


Figure 5.4. Temperature dependent intralayer distance  $h$  (vertical distance between S layers in a trilayer) and interlayer distance  $h_{VDW}$  (vertical distance between adjacent S layers) of  $\text{HfS}_2$ . The effective interaction dominating out-of-plane vibrational mode  $A_{1g}$  is represented by  $C_{VDW}$  and  $C_{intra}$ , respectively.

The contradicting temperature dependence of  $\omega_A$  below and above 300 K, is explained by the lattice structural change as a function of temperature. At  $T < 300$  K, as temperature increases,  $h$  decreases while  $h_{VDW}$  increases. As the effect of  $h$  on  $\omega_A$  overwhelms that of  $h_{VDW}$ , overall  $\omega_A$  increases as temperature is raised. At  $T > 300$  K, the trend of temperature dependence of  $h$  and  $h_{VDW}$  reverses. As a result,  $\omega_A$  decreases as temperature is raised.

## 5.5 Summary

In summary, we have examined temperature dependent lattice structural and phonon properties of  $\text{HfS}_2$  via QHA, CPMD, and experimental approaches. For the first

time, we identify the 3R phase above 300 K, which is characterized by the ABC stacking order different from AAA stacking order in its 1T phase below 300 K. In experiments, we observe a change in the first-order temperature coefficients of  $A_{1g}$  and  $E_g$  mode frequencies, and lattice parameters  $a$  and  $c$  at room temperature. An anomalous phonon stiffening of  $A_{1g}$  mode below 300 K is also observed in Raman spectroscopy measurements. However, this trend reverses to phonon softening above 300 K. The CPMD simulations discovers a phase transition at 300 K which is characterized by a change in the stacking order from AAA to ABC. The structural change at 300 K is validated by good agreements between CPMD simulations and experimental measurements on all the above temperature coefficients. By comparing the CPMD and QHA results, we attribute the phase change to be due to phonon anharmonicity. The anomalous  $A_{1g}$  phonon stiffening is due to decrease of the intralayer thickness of the  $\text{HfS}_2$  trailayer, as temperature increases.

## Chapter 6 Conclusions and outlook

### 6.1 Summary and contributions

In this thesis, we have studied phonon-mediated thermal transport in two TMDC materials – MoS<sub>2</sub> and HfS<sub>2</sub>.

In Chapter 2, we presented the theory of phonons and various computational approaches used to investigate thermal transport properties. Using LD method, we showed that the lattice phonon properties are decided by the derivatives of Hamiltonian with respect to atom displacements. The higher than 2<sup>nd</sup> order terms in the Taylor expansion of the Hamiltonian dominates the phonon anharmonicity. Different assumptions - the HA, QHA, and FAA - can be made to include of phonon anharmonicity to different levels. Following the discussions on phonons, we briefly described the theory behind computational approaches including MD, DFT, and CPMD. Finally, methodologies of applying these computational techniques to calculating different thermal transport properties components were presented.

In Chapter 3, the electronic and phonon transport properties of folded MoS<sub>2</sub> were investigated. This was the first theoretical study of how the electronic and thermal properties of MoS<sub>2</sub> can be modulated by folding. Previously, folding had been discovered only by experiments that measured optical and electronic properties of MoS<sub>2</sub> [70, 127]. We calculated the atomic structure of folded SLMoS<sub>2</sub> using a combination of MD and DFT methods. The atomic structure is composed of a racket shape folding edge and a bilayer region, as shown in Figure 3.5. The dimensional feature of the folded structure were found

to be independent of the wrapping length. Subsequent DFT calculations showed that the electronic bandgap exhibits a strong dependence on the wrapping length, monotonically converging (from below) to the bandgap value of the bilayer structure. On the other hand, MD calculations showed that the thermal conductivities are insensitive to the wrapping length and much smaller compared to the one of SL. These findings suggested a new route for designing MoS<sub>2</sub>-based electronic device where its electronic properties can be tuned without affecting the thermal aspect.

The key contributions are:

- The atomic structure of folded SLMoS<sub>2</sub> was discovered (see Sec. 3.3.1). This provides a theoretical understanding on the folded structure observed in experiments [70, 127].
- The structural, electronic, and phonon properties show different dependence on the wrapping length (see Sec. 3.3). As the wrapping length is varied, the configuration of the folding edge is unchanged. Such structural dependence on the wrapping length leads to different characteristics of the electronic and phonon properties. The electronic band gap increases (see Figure 3.7) while thermal conductivity does not change (see Figure 3.11), when the wrapping length is increased.
- Reduction in the thermal conductivity of folded SLMoS<sub>2</sub> as compared to the one of SLMoS<sub>2</sub> sheet is attributed to the increased anharmonic phonon scattering (see Sec. 3.3.3). This was supported by the evidence that the phonon RT of folded SLMoS<sub>2</sub> is only around half of the value for SLMoS<sub>2</sub> sheet (see

Table 3.3). Physically, the increase in the phonon scattering is due to the break of lattice symmetry introduced by folding.

In Chapter 4, we studied the temperature dependent phonon properties of 1T-HfS<sub>2</sub> under the QHA. For the first time, anisotropy and temperature dependence of full BZ phonons in bulk HfS<sub>2</sub> were determined by performing DFT calculations. The LO-TO splitting, namely breaking of the degeneracy between longitudinal and transverse optical phonon modes, were identified. The magnitude of splitting was calculated using the atom force constants. The mode dependent phonon RTs were estimated under the Klemens' theory. The obtained RTs were used in combination with group velocities and specific heat to calculate thermal conductivity, under the kinetic phonon theory (see Sec. 2.1.3). We identified contributions from different phonon modes towards the thermal conductivity where a surprisingly high portion (~80%) comes from the ZA phonons. The anisotropy and temperature dependence of the phonon transport components were analyzed.

The key contributions are:

- ZA phonons dominate thermal transport in HfS<sub>2</sub>. The ZA branch contributes almost 80% to the total thermal conductivity from 0 K to 500 K [see Figure 4.8(d)]. This is due to the larger specific heats [see Figure 4.3(c)], longer RTs [see Sec. 4.4.3], and considerable group velocities [see Figure 4.3(b)] of ZA modes compared to other modes.
- HfS<sub>2</sub> exhibits uncharacteristically strong VDW interaction relative to the in-plane bonds. The ratio between the VDW and in-plane interaction of HfS<sub>2</sub> is

order of magnitude larger than the values of other TMDCs including ZrS<sub>2</sub>, MoS<sub>2</sub>, WS<sub>2</sub>, and WSe<sub>2</sub> (see Table 4.4). This is due to weak in-plane atomic interactions. As a result, the in-plane thermal conductivity of HfS<sub>2</sub> is significantly smaller than other 2D materials (see Table 4.6).

- Effect of temperature on lattice structure and thermal transport components were examined (see Sec.4.4.4). The temperature dependence of thermal properties were illustrated by discussing the interplay between phonon scattering effect and thermally excited phonon population (see Sec. 4.4.4).

In Chapter 5, we examined the temperature dependent lattice structural and phonon properties of HfS<sub>2</sub> via QHA, CPMD, and experimental approaches. Anomalous phonon stiffening was observed in A<sub>1g</sub> mode via Raman spectroscopy measurements. XRD measurements were performed to probe the lattice structural properties. Interestingly, the first-order temperature coefficients of A<sub>1g</sub> and E<sub>g</sub> frequency, and lattice parameters  $a$  and  $c$  all change at room temperature. Subsequent QHA and CPMD calculations were carried out to explore the underlying mechanisms. From these calculations, all the above temperature coefficients are obtained and compared with experimental values. The CPMD simulations discovered a structural phase transition at 300 K, which is characterized by a change in the stacking order from AAA to ABC. The structural change at 300 K is validated by good agreements between the temperature coefficients obtained from CPMD simulations and experimental measurements. By comparing the CPMD and QHA results, we attribute the phase change to be due to anharmonicity effects. The anomalous A<sub>1g</sub>

phonon stiffening is due to the decrease of the intralayer thickness of the HfS<sub>2</sub> trilayer, as temperature increases.

The key contributions are:

- The 3R phase (>300 K) with ABC stacking order was discovered. This was enabled by the inclusion of full phonon anharmonicity in CPMD simulations (see Sec. 5.4.2).
- An anomalous phonon stiffening as temperature increases was found via Raman spectroscopy measurements. The mechanism is the decreasing thickness of trilayer as temperature is raised (see Sec. 5.4.3).

## **6.2 Future works**

### **6.2.1 Temperature dependence and anharmonicity of phonons**

Temperature plays a vital role in phonon mediated thermal transport. In studying the temperature dependence of phonon properties, how to account for phonon anharmonicity is a primary obstacle. Most previous work adopts the QHA [75, 76, 77, 78] or phonon BTE methods [117, 118], limiting the phonon scattering under consideration to at most the three-phonon processes. In Chapter 5, we have performed CPMD calculations to account for full anharmonic phonon scattering in examining the thermal properties of HfS<sub>2</sub>. As a result, a novel structural change at room temperature is discovered. On the other hand, the QHA (see Chapter 4) and BTE approaches [159, 160] fail to capture such a lattice

phase change. This approach by combining MD technique with SED method provides an effective route for determining accurate anharmonic phonon properties.

The details of applying above computational approach are:

- 1) Calculate the temperature dependent phonon RTs, MFPs, group velocities, and specific heat using the phonon BTE and QHA method. These are fundamental phonon components of thermal transport properties [see Sec. 2.1.3 and Eq.(2.19)].
- 2) Perform MD simulations at different temperature to relax the lattice to thermal equilibrium and collect thermodynamics data including lattice configuration, atomic trajectories, velocities, and so on.
- 3) Use the atomic trajectories and phonon eigenvectors as the input to the SED method and calculate phonon RTs.
- 4) Compare phonon RTs calculated from QHA, phonon BTE, and SED method. The difference among these RTs will reveal the effect of volume, three-phonon scattering, and higher than 3<sup>rd</sup> order scattering on the phonon properties. Contributions from the harmonic and anharmonic parts to the thermal conductivity can be quantified.

### **6.2.2 Thermal transport in HfS<sub>2</sub>**

The distinct anisotropy between c-axis and in-plane interactions (see Sec. 4.3.2), together with the structural change from 1T to 3R phase, lead to our belief that the thermal properties of HfS<sub>2</sub> are very unique. However, very little is known about the thermal

transport properties of  $\text{HfS}_2$ . Previous works only consider the 1T phase [159, 160], leaving the thermal transport in the higher temperature 3R phase unexplored. Using the various computation approaches introduced in Chapter 2, we could gain a deeper understanding of the phonon-mediated thermal transport in  $\text{HfS}_2$  at different temperature.

### 6.2.3 Folded $\text{MoS}_2$ and origami nanostructures

Due to its three-fold rotational symmetry, thermal conductivity of  $\text{SLMoS}_2$  is isotropic in all in-plane orientations [134, 211]. Folding will change the atomic structure of  $\text{SLMoS}_2$  into a 1D nanostructure, the question of whether the isotropy of thermal conductance will be preserved when  $\text{SLMoS}_2$  is folded along different lattice orientations needs to be answered. The effect of folding on phonon properties such as group velocity, RTs, and thermal conductivity as a function of lattice orientation can be studied. The dependence of electronic properties on lattice orientation also remains to be explored. These studies will permit application of folded  $\text{SLMoS}_2$  into devices where transport properties along certain lattice orientation is favored. An overview of proposed study on folding lattice orientations is shown in Figure 6.1.

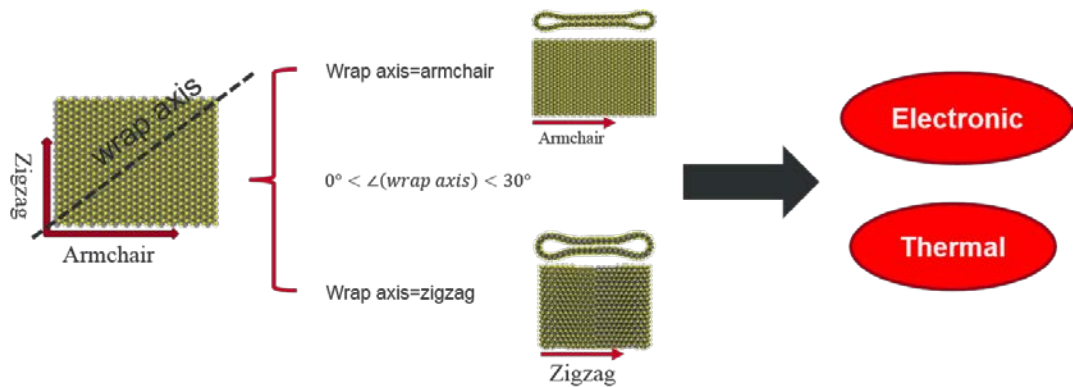


Figure 6.1. Schematics of proposed study on folding along different lattice orientations. Due to the hexagonal closed pack lattice structure, the angle between wrap axis and armchair orientation can vary between  $0^\circ$  to  $30^\circ$  to create different folds.

Building up upon the above studies, device application of origami MoS<sub>2</sub> nanostructures is promising. The origami graphene nanostructures have already been shown to possess interesting mechanical [122], spintronic [212], and optical [213] properties. Therefore, SLMoS<sub>2</sub> can potentially be folded to create novel origami nanostructures that possess promising properties.

## Bibliography

- [1] Q. H. Wang, K. Kalantar-Zadeh, A. Kis, J. N. Coleman and M. S. Strano, "Electronics and optoelectronics of two-dimensional transition metal dichalcogenides," *Nature nanotechnology*, vol. 7, no. 11, p. 699, 2012.
- [2] N. Choudhary, M. D. Patel, J. Park, B. Sirota and W. Choi, "Synthesis of large scale MoS<sub>2</sub> for electronics and energy applications," *Journal of Materials Research*, vol. 31, no. 7, pp. 824-831, 2016.
- [3] J. Peng, G. Zhang and B. Li, "Thermal management in MoS<sub>2</sub> based integrated device using near-field radiation," *Applied Physics Letters*, vol. 107, no. 13, p. 133108, 2015.
- [4] K. S. Novoselov, A. K. Geim, S. V. Morozov, Y. Z. D. Jiang, S. V. Dubonos, I. V. Grigorieva and A. A. Firsov., "Electric field effect in atomically thin carbon films," *science*, vol. 306, no. 5696, pp. 666-669, 2004.
- [5] A. C. Neto, F. Guinea, N. M. Peres, K. S. Novoselov and A. K. Geim, "The electronic properties of graphene," *Reviews of modern physics*, vol. 81, no. 1, p. 109, 2009.
- [6] A. S. Mayorov, R. V. Gorbachev, S. V. Morozov, L. Britnell, R. Jalil, L. A. Ponomarenko, P. Blake, K. S. Novoselov, K. Watanab, T. Taniguch and A. K.

- Geim, "Micrometer-Scale Ballistic Transport in Encapsulated Graphene at Room Temperature," *Nano letters*, vol. 11, no. 6, pp. 2396-2399, 2011.
- [7] A. A. Balandin, "Thermal properties of graphene and nanostructured carbon materials," *Nature materials*, vol. 10, no. 8, p. 569, 2011.
- [8] M.-W. Lin, C. Ling, Y. Zhang, H. J. Yoon, M. M.-C. Cheng, L. A. Agapito, N. Kioussis, N. Widjaja and Z. Zhou, "Room-temperature high on/off ratio in suspended graphene nanoribbon field-effect transistors," *Nanotechnology*, vol. 22, no. 26, p. 265201, 2011.
- [9] R. Balog, B. Jørgensen, L. Nilsson, M. Andersen, E. Rienks, M. Bianchi, M. Fanetti, E. Lægsgaard, A. Baraldi, S. Lizzit, Z. Sljivancanin, F. Besenbacher, B. Hammer, T. G. Pedersen, P. Hofmann and Liv, "Bandgap opening in graphene induced by patterned hydrogen adsorption," *Nature materials*, vol. 9, no. 4, p. 315, 2010.
- [10] Y. Zhang, T.-T. Tang, C. Girit, Z. Hao, M. C. Martin, A. Zettl, M. F. Crommie, Y. R. Shen and F. Wang, "Direct observation of a widely tunable bandgap in bilayer graphene," *Nature*, vol. 459, no. 7248, p. 820, 2009.
- [11] H. Shi, H. Pan, Y. W. Zhang and B. I. Yakobson, "Quasiparticle Band Structures and Optical Properties of Strained Monolayer MoS<sub>2</sub> and WS<sub>2</sub>," *Physical Review B*, vol. 87, p. 155304, 2013.

- [12] A. Kuc, N. Zibouche and T. Heine, "Influence of Quantum Confinement on The Electronic Structure of The Transition Metal Sulfide  $TS_2$ ," *Physical Review B*, vol. 83, p. 245213, 2011.
- [13] C. Gong, H. Zhang, W. Wang, L. Colombo, R. M. Wallace and K. Cho, "Band alignment of two-dimensional transition metal dichalcogenides: Application in tunnel field effect transistors," *Applied Physics Letters*, vol. 103, no. 5, p. 053513, 2013.
- [14] B. Radisavljevic, A. Radenovic, J. Brivio, I. V. Giacometti and A. Kis, "Single-layer  $MoS_2$  transistors," *Nature nanotechnology*, vol. 6, no. 3, p. 147, 2011.
- [15] Y. Cui, R. Xin, Z. Yu, Y. Pan, Z. Ong, X. Wei, J. Wang, H. Nan, Z. Ni, Y. Wu, T. Chen, Y. Shi, B. Wang, G. Zhang, Y. Zhang and X. Wang, "High-Performance Monolayer  $WS_2$  Field-Effect Transistors on High- $\kappa$  Dielectrics," *Advanced Materials*, vol. 27, no. 35, pp. 5230-5234, 2015.
- [16] J. Wilson and A. Yoffe, "The transition metal dichalcogenides discussion and interpretation of the observed optical, electrical and structural properties," *Advances in Physics*, vol. 18, no. 73, pp. 193-335, 1969.
- [17] K. S. Novoselov, D. Jiang, F. Schedin, T. J. Booth, V. V. Khotkevich, S. V. Morozov and A. K. Geim, "Two-dimensional atomic crystals," *Proceedings of the National Academy of Sciences*, vol. 102, no. 30, pp. 10451-10453, 2005.
- [18] X. Li, W. Cai, J. An, S. Kim, J. Nah, D. Yang, R. Piner, A. Velamakanni, I. Jung, E. Tutuc, S. K. B. L. Colombo<sup>3</sup> and R. S. Ruoff, "Large-Area Synthesis of High-

- Quality and Uniform Graphene Films on Copper Foils," *Science*, vol. 324, no. 5932, pp. 1312-1314, 2009.
- [19] J. W. Suk, A. Kitt, C. W. Magnuson, Y. Hao, S. Ahmed, J. An, A. K. Swan, B. B. Goldberg and R. S. Ruoff, "Transfer of CVD-grown monolayer graphene onto arbitrary substrates," *ACS nano*, vol. 5, no. 9, pp. 6916-6924, 2011.
- [20] S. Manzeli, D. Ovchinnikov, D. Pasquier, O. V. Yazyev and A. Kis, "2D transition metal dichalcogenides," *Nature Reviews Materials*, vol. 2, no. 8, p. 17033, 2017.
- [21] A. Splendiani, L. Sun, Y. Zhang, T. Li, J. Kim, C. Chim, G. Galli and F. Wang, "Emerging Photoluminescence in Monolayer MoS<sub>2</sub>," *Nano letters.*, vol. 10, pp. 1271-1275., 2010.
- [22] D. Braga, I. G. Lezama, H. Berger and A. F. Morpurgo, "Quantitative determination of the band gap of WS<sub>2</sub> with ambipolar ionic liquid-gated transistors," *Nano letters*, vol. 12, no. 10, pp. 5218-5223, 2012.
- [23] M. M. Ugeda, A. J. Bradley, Y. Zhang, S. Onishi, Y. Chen, W. Ruan, C. Ojeda-Aristizabal, H. Ryu, M. T. Edmonds, H.-Z. Tsai, A. Riss, S.-K. Mo, D. Lee, A. Zettl, Z. Hussain, Z.-X. Shen and M. F. Crommie, "Characterization of collective ground states in single-layer NbSe<sub>2</sub>," *Nature Physics*, vol. 12, no. 1, p. 92, 2016.
- [24] K. F. Mak, C. Lee, J. Hone, J. Shan and T. F. Heinz, "Atomically Thin MoS<sub>2</sub>: A New Direct-Gap Semiconductor," *Physical Review Letters.*, vol. 105, p. 136805., 2010.

- [25] J. A. Wilson, F. J. D. Salvo and S. Mahajan, "Charge-density waves and superlattices in the metallic layered transition metal dichalcogenides," *Advances in Physics*, vol. 24, no. 2, pp. 117-201, 1975.
- [26] E. Revolinsky, G. A. Spiering and D. J. Beerntsen, "Superconductivity in the niobium-selenium system," *Journal of Physics and Chemistry of Solids*, vol. 26, no. 6, pp. 1029-1034, 1965.
- [27] T. Valla, A. V. Fedorov, P. D. Johnson, J. Xue, K. E. Smith and F. J. DiSalvo, "Charge-density-wave-induced modifications to the quasiparticle self-energy in 2H-TaSe<sub>2</sub>," *Physical review letters*, vol. 85, no. 22, p. 4759, 2000.
- [28] M. Calandra, "2D materials: Charge density waves go nano," *Nature nanotechnology*, vol. 10, no. 9, p. 737, 2015.
- [29] S. Sim, J. Park, J.-G. Song, C. In, Y.-S. Lee, H. Kim and H. Choi, "Exciton dynamics in atomically thin MoS<sub>2</sub>: interexcitonic interaction and broadening kinetics," *Physical Review B*, vol. 88, no. 7, p. 075434, 2013.
- [30] M. A. Lukowski, A. S. Daniel, F. Meng, A. Forticaux, L. Li and S. Jin, "Enhanced hydrogen evolution catalysis from chemically exfoliated metallic MoS<sub>2</sub> nanosheets," *Journal of the American Chemical Society*, vol. 135, no. 28, pp. 10274-10277, 2013.
- [31] R. Yan, J. Simpson, S. Bertolazzi, J. Brivio, M. Watson, X. Wu, A. Kis, T. Luo, H. Walker, A.R. and H. Xing, "Thermal Conductivity of Monolayer

- Molybdenum Disulfide Obtained from Temperature-dependent Raman Spectroscopy," *ACS nano.*, vol. 8, pp. 986-993, 2014.
- [32] S. Sahoo, A. P. Gaur, M. Ahmadi, M. J. F. Guinel and R. S. Katiyar, "Temperature-Dependent Raman Studies and Thermal Conductivity of Few-Layer MoS<sub>2</sub>," *The Journal of Physical Chemistry C.*, vol. 117, pp. 9042-9047, 2013.
- [33] A. Taube, J. Judek, A. Łapińska and M. Zdrojek, "Temperature-dependent thermal properties of supported MoS<sub>2</sub> monolayers," *ACS applied materials & interfaces*, vol. 7, no. 9, pp. 5061-5065, 2015.
- [34] I. Jo, M. T. Pettes, E. Ou, W. Wu and L. Shi, "Basal-plane thermal conductivity of few-layer molybdenum disulfide," *Applied Physics Letters*, vol. 104, no. 20, p. 201902, 2014.
- [35] P. Jiang, X. Qian, X. Gu and R. Yang, "Probing Anisotropic Thermal Conductivity of Transition Metal Dichalcogenides MX<sub>2</sub> (M= Mo, W and X= S, Se) using Time-Domain Thermoreflectance," *Advanced Materials*, vol. 29, no. 36, p. 1701068, 2017.
- [36] J.-W. Jiang, X. Zhuang and T. Rabczuk, "Orientation dependent thermal conductance in single-layer MoS<sub>2</sub>," *Scientific reports*, vol. 3, p. 2209, 2013.
- [37] A. Cepellotti, G. Fugallo, L. Paulatto, M. Lazzeri, F. Mauri and N. Marzari, "Phonon hydrodynamics in two-dimensional materials," *Nature communications*, vol. 6, p. 6400, 2015.

- [38] X. Gu, B. Li and R. Yang, "Layer Thickness-Dependent Phonon Properties and Thermal Conductivity of MoS<sub>2</sub>," *Journal of Applied Physics.*, vol. 119, p. 085106, 2016.
- [39] W. Li, J. Carrete and N. Mingo, "Thermal Conductivity and Phonon Linewidths of Monolayer MoS<sub>2</sub> from First Principles," *Applied Physics Letters.*, vol. 103, p. 253103, 2013.
- [40] X. Wei, Y. Wang, Y. Shen, G. Xie, H. Xiao, J. Zhong and G. Zhang, "Phonon thermal conductivity of monolayer MoS<sub>2</sub>: A comparison with single layer graphene," *Applied Physics Letters*, vol. 105, no. 10, p. 103902, 2014.
- [41] Y. Cai, J. Lan, G. Zhang and Y.-W. Zhang, "Lattice vibrational modes and phonon thermal conductivity of monolayer MoS<sub>2</sub>," *Physical Review B*, vol. 89, no. 3, p. 035438, 2014.
- [42] D. O. Lindroth and P. Erhart, "Thermal transport in van der Waals solids from first-principles calculations," *Physical Review B*, vol. 94, no. 11, p. 115205, 2016.
- [43] N. Peimyoo, J. Shang, W. Yang, Y. Wang, C. Cong and T. Yu, "Thermal conductivity determination of suspended mono-and bilayer WS<sub>2</sub> by Raman spectroscopy," *Nano Research*, vol. 8, no. 4, pp. 1210-1221, 2015.
- [44] B. Peng, H. Zhang, H. Shao, Y. Xu, X. Zhang and H. Zhu, "Thermal conductivity of monolayer MoS<sub>2</sub>, MoSe<sub>2</sub>, and WS<sub>2</sub>: interplay of mass effect, interatomic bonding and anharmonicity," *Rsc Advances*, vol. 6, no. 7, pp. 5767-5773, 2016.

- [45] X. Zhang, D. Sun, Y. Li, G.-H. Lee, X. Cui, D. Chenet, Y. You, T. F. Heinz and J. C. Hone, "Measurement of lateral and interfacial thermal conductivity of single-and bilayer MoS<sub>2</sub> and MoSe<sub>2</sub> using refined optothermal raman technique," ACS applied materials & interfaces., vol. 7, pp. 25923-25929, 2015.
- [46] Y. Hong, J. Zhang and X. C. Zeng, "Thermal conductivity of monolayer MoSe<sub>2</sub> and MoS<sub>2</sub>," The Journal of Physical Chemistry C, vol. 120, no. 45, pp. 26067-26075, 2016.
- [47] W.-X. Zhou and K.-Q. Chen, "First-principles determination of ultralow thermal conductivity of monolayer WSe<sub>2</sub>," Scientific reports, vol. 5, p. 15070, 2015.
- [48] G. Yumnam, T. Pandey and A. K. Singh, "High temperature thermoelectric properties of Zr and Hf based transition metal dichalcogenides: A first principles study," The Journal of chemical physics, vol. 143, no. 23, p. 234704, 2015.
- [49] X. Gu and R. Yang, "Phonon transport in single-layer transition metal dichalcogenides: A first-principles study," Applied Physics Letters , vol. 105, no. 13, p. 131903, 2014.
- [50] G. A. Slack, "Nonmetallic crystals with high thermal conductivity," Journal of Physics and Chemistry of Solids, vol. 34, no. 2, pp. 321-335, 1973.
- [51] L. Lindsay, D. A. Broido and N. Mingo, "Flexural phonons and thermal transport in graphene," Physical Review B, vol. 82, no. 11, p. 115427, 2010.

- [52] A. Cingolani, M. Lugara, G. Scamarcio and F. Lévy, "The Raman scattering in hafnium disulfide," *Solid state communications*, vol. 62, no. 2, pp. 121-123, 1987.
- [53] Greenaway, D. L. and R. Nitsche, "Preparation and optical properties of group IV–VI<sub>2</sub> chalcogenides having the CdI<sub>2</sub> structure," *Journal of Physics and Chemistry of Solids*, vol. 26, no. 9, pp. 1445-1458, 1965.
- [54] G. Lucovsky, R. M. White, J. A. Benda and J. F. Revelli., "Infrared-reflectance spectra of layered group-IV and group-VI transition-metal dichalcogenides," *Physical Review B*, vol. 7, no. 8, p. 3859, 1973.
- [55] L. Roubi and C. Carlone, "Resonance Raman spectrum of HfS<sub>2</sub> and ZrS<sub>2</sub>," *Physical Review B*, vol. 37, no. 12, p. 6808, 1988.
- [56] F. VanGessel, "Phonon Modeling in Nano-and Micro-scale Crystalline Systems," 2018.
- [57] S. Najmaei, M. R. Neupane, B. M. Nichols, R. A. Burke, A. L. Mazzoni, M. L. Chin, D. A. Rhodes, L. Balicas, A. D. Franklin and M. Dubey., "Cross-Plane Carrier Transport in Van der Waals Layered Materials," *Small*, vol. 14, no. 20, p. 1703808, 2018.
- [58] T. Feng, L. Lindsay and X. Ruan, "Four-phonon scattering significantly reduces intrinsic thermal conductivity of solids," *Physical Review B*, vol. 96, no. 16, p. 161201, 2017.

- [59] A. Mobaraki, A. Kandemir, H. Yapicioglu, O. Gülseren and C. Sevik, "Validation of inter-atomic potential for WS<sub>2</sub> and WSe<sub>2</sub> crystals through assessment of thermal transport properties," Computational Materials Science, vol. 144, pp. 92-98, 2018.
- [60] P. Anees, M. C. Valsakumar and B. K. Panigrahi, "Anharmonicity of optic modes in monolayer MoS<sub>2</sub>," Applied Physics Letters, vol. 108, no. 10, p. 101902, 2016.
- [61] A. Mobaraki, C. Sevik, H. Yapicioglu, D. Çakır and O. Gülseren, "Temperature-dependent phonon spectrum of transition metal dichalcogenides calculated from the spectral energy density: Lattice thermal conductivity as an application," Physical Review B, vol. 100, no. 3, p. 035402, 2019.
- [62] G. Zhu, J. Liu, Q. Zheng, R. Zhang, D. Li, D. Banerjee and D. G. Cahill, "Tuning thermal conductivity in molybdenum disulfide by electrochemical intercalation," Nature communications, vol. 7, p. 13211, 2016.
- [63] A. Pisoni, J. Jacimovic, R. Gaál, B. Náfrádi, H. Berger, Z. Révay and L. Forró, "Anisotropic transport properties of tungsten disulfide," Scripta Materialia, vol. 114, pp. 48-50, 2016.
- [64] R. Cheng, S. Jiang, Y. Chen, Y. Liu, N. Weiss, H.-C. Cheng, H. Wu, Y. Huang and X. Duan, "Few-layer molybdenum disulfide transistors and circuits for high-speed flexible electronics," Nature communications, vol. 5, p. 5143, 2014.

- [65] S. Das and J. Appenzeller, "Screening and interlayer coupling in multilayer MoS<sub>2</sub>," *physica status solidi (RRL)*–Rapid Research Letters, vol. 7, no. 4, pp. 268-273, 2013.
- [66] A. Sood, F. Xiong, S. Chen, R. Cheaito, F. Lian, M. Asheghi, Y. Cui, D. Donadio, K. E. Goodson and E. Pop, "Quasi-Ballistic Thermal Transport Across MoS<sub>2</sub> Thin Films," *Nano letters*, vol. 19, no. 4, pp. 2434-2442, 2019.
- [67] Z. Gong, G.-B. Liu, H. Yu, D. Xiao, X. Cui, X. Xu and W. Yao, "Magnetoelectric effects and valley-controlled spin quantum gates in transition metal dichalcogenide bilayers," *Nature communications*, vol. 4, p. 2053, 2013.
- [68] B. Zhu, H. Zeng, J. Dai, Z. Gong and X. Cui, "Anomalously robust valley polarization and valley coherence in bilayer WS<sub>2</sub>," *Proceedings of the National Academy of Sciences*, vol. 111, no. 32, pp. 11606-11611, 2014.
- [69] A. M. Jones, H. Yu, J. S. Ross, P. Klement, N. J. Ghimire, J. Yan, D. G. Mandrus, W. Yao and X. Xu, "Spin–layer locking effects in optical orientation of exciton spin in bilayer WSe<sub>2</sub>," *Nature Physics*, vol. 10, no. 2, p. 130, 2014.
- [70] A. Castellanos-Gomez, H. S. van der Zant and G. A. Steele, "Folded MoS<sub>2</sub> Layers with Reduced Interlayer Coupling," *Nano Research.*, vol. 7, pp. 572-578, 2014.
- [71] T. Jiang, H. Liu, D. Huang, S. Zhang, Y. Li, X. Gong, Y.-R. Shen, W.-T. Liu and S. Wu, "Valley and Band Structure Engineering of Folded MoS<sub>2</sub> Bilayers," *Nature nanotechnology.*, vol. 9, pp. 825-829, 2014.

- [72] W. Yao, D. Xiao and Q. Niu, "Valley-dependent optoelectronics from inversion symmetry breaking," *Physical Review B*, vol. 77, no. 23, p. 235406, 2008.
- [73] N. D. M. Neil W. Ashcroft, *Solid State Physics*, Saunders College, 1976.
- [74] N. W. Ashcroft and N. D. Mermin, *Solid State Physics*, 1976.
- [75] M. T. Dove, *Introduction to lattice dynamics*, New York: Cambridge university press, 1993.
- [76] B. Pamuk, "Nuclear Quantum Effects in Ices Phases and Water from First Principles Calculations (Doctoral dissertation, State University of New York at Stony Brook)," 2014.
- [77] I. L. Locht, A. Fasolino and P. C. M. Christianen, "The effect of temperature on the phonon dispersion relation in graphene (Doctoral dissertation, Master thesis, Radboud University of Nijmegen: Nijmegen, Netherlands)," 2012.
- [78] N. Mounet and N. Marzari., "First-principles determination of the structural, vibrational and thermodynamic properties of diamond, graphite, and derivatives," *Physical Review B*, vol. 71, no. 20, p. 205214, 2005.
- [79] P. Mazur, E. W. Montroll, A. A. Maradudin, E. W. Montroll, G. H. Weiss and I. P. Ipatova, *Theory of Lattice Dynamics in the Harmonic Approximation*, New York: ACADEMIC PRESS INC, 1956.
- [80] J. Ziman, *Electrons and Phonons: the theory of transport phenomena in solids*, New York: Oxford University Press, 2006, pp. 264-267.

- [81] F. VanGessel, J. Peng and P. W. Chung, "A review of computational phononics: the bulk, interfaces, and surfaces," *Journal of materials science*, vol. 53, no. 8, pp. 5641-5683, 2018.
- [82] R. A. Escobar, S. S. Ghai, M. S. Jhon and C. H. Amon, "Multi-length and time scale thermal transport using the lattice Boltzmann method with application to electronics cooling," *International Journal of Heat and Mass Transfer*, vol. 49, no. 1, pp. 97-107, 2006.
- [83] J. A. McCammon, B. R. Gelin and M. Karplus, "Dynamics of folded proteins," *Nature*, vol. 267, no. 5612, p. 585, 1977.
- [84] A. Warshel and M. Levitt, "Theoretical studies of enzymic reactions: dielectric, electrostatic and steric stabilization of the carbonium ion in the reaction of lysozyme," *Journal of molecular biology*, vol. 103, no. 2, pp. 227-249, 1976.
- [85] X. Z. Jiang, M. Feng, K. H. Luo and Y. Ventikos, "Large-scale molecular dynamics simulation of flow under complex structure of endothelial glycocalyx," *Computers & Fluids* 140-146, vol. 173, pp. 140-146, 2018.
- [86] V. A. Voelz, G. R. Bowman, K. Beauchamp and V. S. Pande, "Molecular simulation of ab initio protein folding for a millisecond folder NTL9 (1– 39)," *Journal of the American Chemical Society*, vol. 132, no. 5, pp. 1526-1528, 2010.
- [87] J. Hu, X. Ruan and Y. P. Chen, "Thermal conductivity and thermal rectification in graphene nanoribbons: a molecular dynamics study," *Nano letters*, vol. 9, no. 7, pp. 2730-2735, 2009.

- [88] S. G. Volz and G. Chen, "Molecular dynamics simulation of thermal conductivity of silicon nanowires," *Applied Physics Letters*, vol. 75, no. 14, pp. 2056-2058, 1999.
- [89] J.-W. Jiang, H. S. Park and T. Rabczuk, "Molecular dynamics simulations of single-layer molybdenum disulphide ( $\text{MoS}_2$ ): Stillinger-Weber parametrization, mechanical properties, and thermal conductivity," *Journal of Applied Physics*, vol. 114, no. 6, p. 064307, 2013.
- [90] C. Sevik, A. Kinaci, J. B. Haskins and T. Çağın., "Characterization of thermal transport in low-dimensional boron nitride nanostructures," *Physical Review B*, vol. 84, no. 8, p. 085409, 2011.
- [91] L. Verlet, "Computer" experiments" on classical fluids. I. Thermodynamical properties of Lennard-Jones molecules," *Physical review*, vol. 159, no. 1, p. 98, 1967.
- [92] F. Aryasetiawan and O. Gunnarsson, "The GW method," *Reports on Progress in Physics*, vol. 61, no. 3, p. 237, 1998.
- [93] L. Hedin and S. Lundqvist, "Effects of electron-electron and electron-phonon interactions on the one-electron states of solids," *Solid state physics*, vol. 23, pp. 1-181, 1970.
- [94] P. Hohenberg and W. Kohn, "Inhomogeneous electron gas," *Physical review*, vol. 136, no. 3B, p. B864, 1964.

- [95] W. Kohn and L. J. Sham, "Self-consistent equations including exchange and correlation effects," *Physical review*, vol. 140, no. 4A, p. A1133, 1965.
- [96] D. M. Ceperley and B. J. Alder, "Ground state of the electron gas by a stochastic method," *Physical Review Letters*, vol. 45, no. 7, p. 566, 1980.
- [97] J. P. Perdew and A. Zunger, "Self-interaction correction to density-functional approximations for many-electron systems," *Physical Review B*, vol. 23, no. 10, p. 5048, 1981.
- [98] J. P. Perdew, "Density-functional approximation for the correlation energy of the inhomogeneous electron gas," *Physical Review B*, vol. 33, no. 12, p. 8822, 1986.
- [99] J. P. Perdew, "Erratum: Density-functional approximation for the correlation energy of the inhomogeneous electron gas," *Physical review B*, vol. 34, no. 10, p. 7406, 1986.
- [100] J. P. Perdew and W. Yue, "Accurate and simple density functional for the electronic exchange energy: Generalized gradient approximation," *Physical review B*, vol. 33, no. 12, p. 8800, 1986.
- [101] J. P. Perdew, K. Burke and M. Ernzerhof, "Generalized gradient approximation made simple," *Physical review letters*, vol. 77, no. 18, p. 3865, 1996.
- [102] J. Hutter, "Car–Parrinello molecular dynamics," *Wiley Interdisciplinary Reviews: Computational Molecular Science*, vol. 2, no. 4, pp. 604-612, 2012.

- [103] R. Car and M. Parrinello, "Unified approach for molecular dynamics and density-functional theory," *Physical review letters*, vol. 55, no. 22, p. 2471, 1985.
- [104] M. Bernasconi, G. L. Chiarotti, P. Focher, S. Scandolo, E. Tosatti and M. Parrinello, "First-principle-constant pressure molecular dynamics.," *Journal of Physics and Chemistry of Solids*, vol. 56, no. 3-4, pp. 501-505, 1995.
- [105] G. J. F. Kresse and J. Hafner, "Ab initio force constant approach to phonon dispersion relations of diamond and graphite," *EPL (Europhysics Letters)*, vol. 32, no. 9, p. 729, 1995.
- [106] S. Wei and M. Y. Chou, "Ab initio calculation of force constants and full phonon dispersions," *Physical review letters*, vol. 69, no. 19, p. 2799, 1992.
- [107] D. Alfè, G. D. Price and M. J. Gillan, "Thermodynamics of hexagonal-close-packed iron under Earth's core conditions," *Physical Review B*, vol. 64, no. 4, p. 045123, 2001.
- [108] P. Giannozzi, S. D. Gironcoli, P. Pavone and S. Baroni, "Ab initio calculation of phonon dispersions in semiconductors," *Physical Review B*, vol. 43, no. 9, p. 7231, 1991.
- [109] S. Baroni, P. Giannozzi and A. Testa, "Green's-function approach to linear response in solids," *Physical Review Letters*, vol. 58, no. 18, p. 1861, 1987.

- [110] S. Baroni, S. D. Gironcoli, A. D. Corso and P. Giannozzi, "Phonons and related crystal properties from density-functional perturbation theory," *Reviews of Modern Physics*, vol. 73, no. 2, p. 515, 2001.
- [111] P. G. Klemens and D. F. Pedraza, "Thermal conductivity of graphite in the basal plane," *Carbon*, vol. 32, no. 4, pp. 735-741, 1994.
- [112] P. G. Klemens, "Theory of the thermal conductivity of solids," in *Thermal conductivity*, vol. 1, Academic Press, 1969, pp. 17-25.
- [113] N. a. N. M. Mounet, "First-principles determination of the structural, vibrational and thermodynamic properties of diamond, graphite, and derivatives," *Physical Review B*, vol. 71, no. 20, p. 205214, 2005.
- [114] X.-H. Zha, J. Zhou, Y. Zhou, Q. Huang, J. He, J. S. Francisco, K. Luo and S. Du, "Promising electron mobility and high thermal conductivity in  $\text{Sc}_2\text{CT}_2$  (T= F, OH) MXenes," *Nanoscale*, vol. 8, no. 11, pp. 6110-6117, 2016.
- [115] X.-H. Zha, Q. Huang, J. He, H. He, J. Zhai, J. S. Francisco and S. Du, "The thermal and electrical properties of the promising semiconductor MXene  $\text{Hf}_2\text{CO}_2$ ," *Scientific reports*, vol. 6, p. 27971, 2016.
- [116] R. Peierls, "Zur kinetischen theorie der wärmeleitung in kristallen," *Annalen der Physik*, vol. 395, no. 8, pp. 1055-1101, 1929.

- [117] W. Li, J. Carrete, N. A. Katcho and N. Mingo, "ShengBTE: A solver of the Boltzmann transport equation for phonons," *Computer Physics Communications*, vol. 185, no. 6, pp. 1747-1758, 2014.
- [118] D. A. Broido, A. Ward and N. Mingo, "Lattice thermal conductivity of silicon from empirical interatomic potentials," *Physical Review B*, vol. 72, no. 1, p. 014308, 2005.
- [119] J. M. Larkin and A. J. McGaughey, "Vibrational Mode Properties of Disordered Solids from High-Performance Atomistic Simulations and Calculations," Pittsburgh, PA, 2013.
- [120] A. J. McGaughey and J. M. Larkin, "Predicting phonon properties from equilibrium molecular dynamics simulations," *Annual Review of Heat Transfer*, vol. 17, 2014.
- [121] J. P. W. C. M. D. a. R. R. N. Peng, "Tunable electron and phonon properties of folded single-layer molybdenum disulfide," *Nano Research*, vol. 11, no. 3, pp. 1541-1553, 2018.
- [122] S. Zhu and T. Li, "Hydrogenation-assisted graphene origami and its application in programmable molecular mass uptake, storage, and release," *ACS nano*, vol. 8, no. 3, pp. 2864-2872, 2014.
- [123] P. M. Ajayan, "Nanotubes from carbon," *Chemical reviews*, vol. 99, no. 7, pp. 1787-1800, 1999.

- [124] B. Radisavljevic, A. Radenovic, J. Brivio, I. V. Giacometti and A. Kis, "Single-layer MoS<sub>2</sub> Transistors.," *Nature nanotechnology.*, vol. 6, pp. 147-150, 2011.
- [125] Z. Jin, Q. Liao, H. Fang, Z. Liu, W. Liu, Z. Ding, T. Luo and N. Yang, "A Revisit to High Thermoelectric Performance of Single-layer MoS<sub>2</sub>," *Scientific reports.*, vol. 5, pp. 18342-18342, 2014.
- [126] E. S. Kadantsev and P. Hawrylak, "Electronic Structure of A Single MoS<sub>2</sub> Monolayer," *Solid State Communications.*, vol. 152, pp. 909-913, 2012.
- [127] F. Crowne, M. Amani, A. Birdwell, M. Chin, T. O'Regan, S. Najmaei, Z. Liu, P. Ajayan, J. Lou and M. Dubey, "Blueshift of The A-Exciton Peak in Folded Monolayer 1H-MoS<sub>2</sub>," *Physical Review B.*, vol. 88, p. 235302, 2013.
- [128] S. Huang, X. Ling, L. Liang, J. Kong, H. Terrones, V. Meunier and M. S. Dresselhaus, "Probing The Interlayer Coupling of Twisted Bilayer MoS<sub>2</sub> Using Photoluminescence Spectroscopy," *Nano letters.*, vol. 14, pp. 5500-5508., 2014.
- [129] H. J. Conley, B. Wang, J. I. Ziegler, R. F. Haglund Jr, S. T. Pantelides and K. I. Bolotin, "Bandgap Engineering of Strained Monolayer and Bilayer MoS<sub>2</sub>," *Nano letters.*, vol. 13, pp. 3626-3630, 2013.
- [130] P. Koskinen, I. Fampiou and A. Ramasubramaniam, "Density-Functional Tight-Binding Simulations of Curvature-Controlled Layer Decoupling and Band-Gap Tuning in Bilayer MoS<sub>2</sub>," *Physical review letters.*, vol. 112, p. 186802, 2014.

- [131] Z. Ding, Q. X. Pei, J. W. Jiang and Y. W. Zhang, "Manipulating the Thermal Conductivity of Monolayer MoS<sub>2</sub> via Lattice Defect and Strain Engineering," The Journal of Physical Chemistry C., vol. 119, pp. 16358-16365., 2015.
- [132] S. Plimpton, "Fast Parallel Algorithms for Short-Range Molecular Dynamics," Journal of computational physics., vol. 117, pp. 1-19, 1995.
- [133] J. D. Gale, "GULP: A Computer Program for the Symmetry-adapted Simulation of Solids," Journal of the Chemical Society, Faraday Transactions., vol. 93, pp. 629-637., 1997.
- [134] J. W. Jiang, H. S. Park and T. Rabczuk, "Molecular Dynamics Simulations of Single-Layer Molybdenum Disulphide (MoS<sub>2</sub>): Stillinger-Weber Parametrization, Mechanical Properties, and Thermal Conductivity," Journal of Applied Physics., vol. 114, p. 064307, 2013.
- [135] T. Liang, S. R. Phillpot and S. B. Sinnott, "Parametrization of a Reactive Many-Body Potential for Mo–S Systems," Physical Review B., vol. 79, p. 245110., 2009.
- [136] P. Giannozzi, S. Baroni, N. Bonini, M. Calandra, R. Car, C. Cavazzoni, D. Ceresoli, G. Chiarotti, M. Cococcioni, I. Dabo and A. Dal Corso, "QUANTUM ESPRESSO: A Modular and Open-Source Software Project for Quantum Simulations of Materials," Journal of physics: Condensed matter., vol. 21, p. 395502, 2009.

- [137] S. Grimme, "Semiempirical GGA-Type Density Functional Constructed with a Long-Range Dispersion Correction," *Journal of computational chemistry.*, vol. 27, pp. 1787-1799., 2006.
- [138] B. J. Cox, D. Baowan, W. Bacsa and J. M. Hill, "Relating Elasticity and Graphene Folding Conformation," *RSC Advances.*, vol. 5, pp. 57515-57520., 2015.
- [139] J. Jiang, Z. Qi, H. Park and T. Rabczuk, "Elastic Bending Modulus of Single-Layer Molybdenum Disulfide ( $\text{MoS}_2$ ): Finite Thickness Effect," *Nanotechnology.*, vol. 24, p. 435705, 2013.
- [140] S. Xiong and G. Cao, "Bending Response of Single Layer  $\text{MoS}_2$ ," *Nanotechnology.*, vol. 27, p. 105701, 2016.
- [141] T. Böker, R. Severin, A. Müller, C. Janowitz, R. Manzke, D. Voß, P. Krüger, A. Mazur and J. Pollmann, "Band Structure of  $\text{MoS}_2$ ,  $\text{MoSe}_2$ , and  $\alpha\text{-MoTe}_2$ : Angle-resolved Photoelectron Spectroscopy and Ab initio Calculations," *Physical Review B.*, vol. 64, p. 235305, 2001.
- [142] S. Ahmad and S. Mukherjee, "A Comparative Study of Electronic Properties of Bulk  $\text{MoS}_2$  and Its Monolayer Using DFT Technique: Application of Mechanical Strain on  $\text{MoS}_2$  Monolayer," *Graphene.*, vol. 3, p. 52., 2014.
- [143] Q. Liu, L. Li, Y. Li, Z. Gao, Z. Chen and J. Lu, "Tuning Electronic Structure of Bilayer  $\text{MoS}_2$  by Vertical Electric Field: A First-Principles Investigation," *The Journal of Physical Chemistry C.*, vol. 116, pp. 21556-21562, 2012.

- [144] S. Lebegue and O. Eriksson, "Electronic Structure of Two-Dimensional Crystals from Ab Initio Theory," *Physical Review B.*, vol. 79, p. 115409, 2009.
- [145] R. C. McLaren, "Thermal Conductivity Anisotropy in Molybdenum Disulfide Thin Films," pp. (Doctoral dissertation, University of Illinois at Urbana-Champaign), 2009.
- [146] J. Y. Kim, S. M. Choi, W. S. Seo and W. S. Cho, "Thermal and Electronic Properties of Exfoliated Metal Chalcogenides," *Bulletin of the Korean Chemical Society.*, vol. 31, pp. 3225-3227, 2010.
- [147] J. Liu, G. M. Choi and D. G. Cahill, "Measurement of The Anisotropic Thermal Conductivity of Molybdenum Disulfide by The Time-resolved Magneto-Optic Kerr Effect," *Journal of Applied Physics.*, vol. 116, p. 233107, 2014.
- [148] C. Muratore, V. Varshney, J. J. Gengler, J. Hu, J. E. Bultman, A. K. Roy and A. A. Voevodin, "Thermal anisotropy in nano-crystalline MoS<sub>2</sub> thin films," *Physical Chemistry Chemical Physics.*, vol. 16, no. 3, pp. 1008-1014, 2014.
- [149] A. N. Gandi and U. Schwingenschlögl, "Thermal Conductivity of Bulk and Monolayer MoS<sub>2</sub>," *EPL (Europhysics Letters).*, vol. 113, p. 36002, 2016.
- [150] Y. Cai, J. Lan, G. Zhang and Y. W. Zhang, "Lattice Vibrational Modes and Phonon Thermal Conductivity of Monolayer MoS<sub>2</sub>," *Physical Review B.*, vol. 89, no. 3, p. 035438., 2014.

- [151] X. Liu, G. Zhang, Q. X. Pei and Y. W. Zhang, "Phonon Thermal Conductivity of Monolayer MoS<sub>2</sub> Sheet and Nanoribbons," *Applied Physics Letters.*, vol. 103, p. 133113, 2013.
- [152] J. Peng, S. Najmaei, M. Dubey and P. W. Chung, "Dominant ZA phonons and thermal carriers in HfS<sub>2</sub>," *Journal of Applied Physics*, vol. 126, no. 16, p. 164302, 2019.
- [153] A. Pospischil, M. M. Furchi and T. Mueller, "Solar-energy conversion and light emission in an atomic monolayer pn diode," *Nature nanotechnology*, vol. 9, no. 4, pp. 257-261, 2014.
- [154] D. Kong, H. Wang, J. J. Cha, M. Pasta, K. J. Koski, J. Yao and Y. Cui, "Synthesis of MoS<sub>2</sub> and MoSe<sub>2</sub> films with vertically aligned layers," *Nano letters*, vol. 13, no. 3, pp. 1341-1347, 2013.
- [155] S. Kim, A. Konar, W.-S. Hwang, J. H. Lee, J. Lee, J. Yang and C. J. e. al., "High-mobility and low-power thin-film transistors based on multilayer MoS<sub>2</sub> crystals," *Nature communications*, vol. 3, p. ncomms2018, 2012.
- [156] X. Cui, G.-H. Lee, Y. D. Kim, G. Arefe, P. Y. Huang, C.-H. Lee and D. A. C. e. al., "Multi-terminal transport measurements of MoS<sub>2</sub> using a van der Waals heterostructure device platform," *Nature nanotechnology*, vol. 10, no. 6, p. 534, 2015.

- [157] W. Zhang, Z. Huang, W. Zhang and Y. Li, "Two-dimensional semiconductors with possible high room temperature mobility," *Nano Research*, vol. 7, no. 12, pp. 1731-1737, 2014.
- [158] G. Fiori, F. Bonaccorso, G. Iannaccone, T. Palacios, D. Neumaier, A. Seabaugh, S. K. Banerjee and L. Colombo, "Electronics based on two-dimensional materials," *Nature nanotechnology*, vol. 9, no. 10, p. 768, 2014.
- [159] K. Xu, Z. Wang, F. Wang, Y. Huang, F. Wang, L. Yin, C. Jiang and J. He, "Ultrasensitive Phototransistors Based on Few-Layered  $\text{HfS}_2$ ," *Advanced Materials*, vol. 27, no. 47, pp. 7881-7887, 2015.
- [160] T. Kanazawa, T. Amemiya, A. Ishikawa, V. Upadhyaya, K. Tsuruta, T. Tanaka and Y. Miyamoto, "Few-layer  $\text{HfS}_2$  transistors," *Scientific reports*, vol. 6, p. 22277, 2016.
- [161] A. Togo, L. Chaput and I. Tanaka, "Distributions of phonon lifetimes in Brillouin zones," *Physical Review B*, vol. 91, no. 9, p. 094306, 2015.
- [162] P. Giannozzi, S. Baroni, N. Bonini, M. Calandra, R. Car, C. Cavazzoni, D. Ceresoli and e. al., "QUANTUM ESPRESSO: a modular and open-source software project for quantum simulations of materials," *Journal of physics: Condensed matter*, vol. 21, no. 39, p. 395502, 2009.
- [163] N. Troullier and J. L. Martins, "Efficient pseudopotentials for plane-wave calculations," *Physical review B*, vol. 43, no. 3, p. 1993, 1991.

- [164] J. P. Perdew, K. Burke and M. Ernzerhof, "Generalized gradient approximation made simple," *Physical review letters*, vol. 77, no. 18, p. 3865, 1996.
- [165] S. Goedecker, M. Teter and J. Hutter, "Separable dual-space Gaussian pseudopotentials," *Physical Review B*, vol. 54, no. 3, p. 1703, 1996.
- [166] S. Grimme, "Semiempirical GGA-type density functional constructed with a long-range dispersion correction," *Journal of computational chemistry*, vol. 27, no. 15, pp. 1787-1799, 2006.
- [167] C. K. Gan and Y. Y. F. Liu, "Direct calculation of the linear thermal expansion coefficients of MoS<sub>2</sub> via symmetry-preserving deformations," *Physical Review B*, vol. 94, no. 13, p. 134303, 2016.
- [168] A. Kokalj, "XCrySDen—a new program for displaying crystalline structures and electron densities," *Journal of Molecular Graphics and Modelling*, vol. 17, no. 3-4, pp. 176-179, 1999.
- [169] M. Traving, T. Seydel, L. Kipp, M. Skibowski, F. Starrost, E. E. Krasovskii, A. Perlov and W. Schattke, "Combined photoemission and inverse photoemission study of HfS<sub>2</sub>," *Physical Review B*, vol. 63, no. 3, p. 035107, 2001.
- [170] R. Murray, R. Bromley and A. Yoffe, "The band structures of some transition metal dichalcogenides. II. Group IVA; octahedral coordination," *Journal of Physics C: Solid State Physics*, vol. 5, no. 7, p. 746, 1972.

- [171] H. Jiang, "Structural and electronic properties of  $\text{ZrX}_2$  and  $\text{HfX}_2$  ( $\text{X} = \text{S}$  and  $\text{Se}$ ) from first principles calculations," *The Journal of chemical physics*, vol. 134, no. 20, p. 204705, 2011.
- [172] C. Kreis, S. Werth, R. Adelung, L. Kipp, M. Skibowski, E. E. Krasovskii and W. Schattke, "Valence and conduction band states of  $\text{HfS}_2$ : From bulk to a single layer," *Physical Review B*, vol. 68, no. 23, p. 235331, 2003.
- [173] L. Mattheiss, "Band structures of transition-metal-dichalcogenide layer compounds," *Physical Review B*, vol. 8, no. 8, p. 3719, 1973.
- [174] T. Iwasaki, N. Kuroda and Y. Nishina, "Anisotropy of Lattice Dynamical Properties in  $\text{ZrS}_2$  and  $\text{HfS}_2$ ," *Journal of the Physical Society of Japan*, vol. 51, no. 7, pp. 2233-2240, 1982.
- [175] J. Chen, "Phonons in bulk and monolayer  $\text{HfS}_2$  and possibility of phonon-mediated superconductivity: A first-principles study," *Solid State Communications*, vol. 237, pp. 14-18, 2016.
- [176] X. Gonze, "First-principles responses of solids to atomic displacements and homogeneous electric fields: Implementation of a conjugate-gradient algorithm," *Physical Review B*, vol. 55, no. 16, p. 10337, 1997.
- [177] P. Giannozzi, S. D. Gironcoli, P. Pavone and S. Baroni, "Ab initio calculation of phonon dispersions in semiconductors," *Physical Review B*, vol. 43, no. 9, p. 7231, 1991.

- [178] S. Mañas-Valero, V. García-López, A. Cantarero and M. Galbiati, "Raman spectra of ZrS<sub>2</sub> and ZrSe<sub>2</sub> from bulk to atomically thin layers," *Applied sciences*, vol. 6, no. 9, p. 264, 2016.
- [179] A. Molina-Sanchez and L. Wirtz, "Phonons in single-layer and few-layer MoS<sub>2</sub> and WS<sub>2</sub>," *Physical Review B*, vol. 84, no. 15, p. 155413, 2011.
- [180] W. Zhao, Z. Ghorannevis, K. K. Amara, J. R. Pang, M. Toh, X. Zhang, C. Kloc, P. H. Tan and G. Eda, "Lattice dynamics in mono-and few-layer sheets of WS<sub>2</sub> and WSe<sub>2</sub>," *Nanoscale*, vol. 5, no. 20, pp. 9677-9683, 2013.
- [181] G. A. Slack, "Anisotropic thermal conductivity of pyrolytic graphite," *Physical Review*, vol. 127, no. 3, p. 694, 1962.
- [182] A. N. Gandi and U. Schwingenschlögl, "Thermal conductivity of bulk and monolayer MoS<sub>2</sub>," *EPL (Europhysics Letters)*, vol. 113, no. 3, p. 36002, 2016.
- [183] Z.-Y. Ong and E. Pop, "Effect of substrate modes on thermal transport in supported graphene," *Physical Review B*, vol. 84, no. 7, p. 075471, 2011.
- [184] X.-J. Ge, K.-L. Yao and J.-T. Lü, "Comparative study of phonon spectrum and thermal expansion of graphene, silicene, germanene, and blue phosphorene," *Physical Review B*, vol. 94, no. 16, p. 165433, 2016.
- [185] L.-F. Huang, P.-L. Gong and Z. Zeng, "Phonon properties, thermal expansion, and thermomechanics of silicene and germanene," *Physical Review B*, vol. 91, no. 20, p. 205433, 2015.

- [186] L. F. Huang, P. L. Gong and Z. Zeng, "Correlation between structure, phonon spectra, thermal expansion, and thermomechanics of single-layer MoS<sub>2</sub>," *Physical Review B*, vol. 90, no. 4, p. 045409, 2014.
- [187] P. G. Klemens and D. F. Pedraza, "Thermal conductivity of graphite in the basal plane," *Carbon*, vol. 32, no. 4, pp. 735-741, 1994.
- [188] J. P. Freedman, J. H. Leach, E. A. Preble, Z. Sitar, R. F. Davis and J. A. Malen, "Universal phonon mean free path spectra in crystalline semiconductors at high temperature," *Scientific reports*, vol. 3, p. 2963, 2013.
- [189] B. Peng, H. Zhang, H. Shao, Y. Xu, X. Zhang and H. Zhu, "Towards intrinsic phonon transport in single-layer MoS<sub>2</sub>," *Annalen der Physik*, vol. 528, no. 6, pp. 504-511, 2016.
- [190] S. Chen, A. L. Moore, W. Cai, J. W. Suk, J. An, C. Mishra, C. A. Magnuson, C.W., J. Kang, L. Shi and R. Ruoff, "Raman measurements of thermal transport in suspended monolayer graphene of variable sizes in vacuum and gaseous environments," *ACS nano*, vol. 5, no. 1, pp. 321-328, 2010.
- [191] A. A. Maradudin, E. W. Montroll, G. H. Weiss and I. P. Ipatova, *Theory of lattice dynamics in the harmonic approximation*, vol. 3, New York: Academic press, 1963, pp. 45-46.
- [192] J. M. Karanikas, R. Sooryakumar, C. Carlone and M. Aubin, "Elastic properties of trigonal laminar systems: Brillouin scattering study of Hf<sub>1-x</sub>Zr<sub>x</sub>S<sub>2</sub>," *Physical Review B*, vol. 41, no. 3, p. 1516, 1990.

- [193] Q. Zhao, Y. Guo, K. Si, Z. Ren, J. Bai and X. Xu, "Elastic, electronic, and dielectric properties of bulk and monolayer ZrS<sub>2</sub>, ZrSe<sub>2</sub>, HfS<sub>2</sub>, HfSe<sub>2</sub> from van der Waals density-functional theory," *physica status solidi (b)*, vol. 254, no. 9, p. 1700033, 2017.
- [194] F. A. S. Al-Alamy, A. A. Balchin and M. White, "The expansivities and the thermal degradation of some layer compounds," *Journal of Materials Science*, vol. 12, no. 10, pp. 2037-2042, 1977.
- [195] L. C. Towle, V. Oberbeck, B. E. Brown and R. E. Stajdohar, "Molybdenum diselenide: rhombohedral high pressure-high temperature polymorph," *Science*, vol. 157, no. 3751, pp. 895-896, 1966.
- [196] R. J. Toh, Z. Sofer, J. Luxa, D. Sedmidubský and M. Pumera, "3R phase of MoS<sub>2</sub> and WS<sub>2</sub> outperforms the corresponding 2H phase for hydrogen evolution," *Chemical Communications*, vol. 53, no. 21, pp. 3054-3057, 2017.
- [197] D. Yang, X. Hu, M. Zhuang, Y. Ding, S. Zhou, A. Li, Y. Yu, H. Li, Z. Luo, L. Gan and T. Zhai, "Inversion Symmetry Broken 2D 3R-MoTe<sub>2</sub>," *Advanced Functional Materials*, vol. 28, no. 26, p. 1800785, 2018.
- [198] R. Suzuki, M. Sakano, Y. J. Zhang, R. Akashi, D. Morikawa, A. Harasawa, K. Yaji, K. Kuroda, K. Miyamoto, T. Okuda, K. Ishizaka, R. Arita and Y. Iwasa, "Valley-dependent spin polarization in bulk MoS<sub>2</sub> with broken inversion symmetry," *Nature nanotechnology*, vol. 9, no. 8, p. 611, 2014.

- [199] T. Jiang, H. Liu, D. Huang, S. Zhang, Y. Li, X. Gong, Y.-R. Shen, W.-T. Liu and S. Wu, "Valley and band structure engineering of folded MoS<sub>2</sub> bilayers," *Nature nanotechnology*, vol. 9, no. 10, p. 825, 2014.
- [200] Y. Li, Y. Rao, K. F. Mak, Y. You, S. Wang, C. R. Dean and T. F. Heinz, "Probing symmetry properties of few-layer MoS<sub>2</sub> and h-BN by optical second-harmonic generation," *Nano letters*, vol. 13, no. 7, pp. 3329-3333, 2013.
- [201] D. Xiao, G.-B. Liu, W. Feng, X. Xu and W. Yao, "Coupled spin and valley physics in monolayers of MoS<sub>2</sub> and other group-VI dichalcogenides," *Physical review letters*, vol. 108, no. 19, p. 196802, 2012.
- [202] Y. Oba, T. Tadano, R. Akashi and S. Tsuneyuki, "First-principles study of phonon anharmonicity and negative thermal expansion in ScF<sub>3</sub>," *Physical Review Materials*, vol. 3, no. 3, p. 033601, 2019.
- [203] C. W. Li, X. Tang, J. A. Munoz, J. B. Keith, S. J. Tracy, D. L. Abernathy and B. Fultz, "Structural relationship between negative thermal expansion and quartic anharmonicity of cubic ScF<sub>3</sub>," *Physical review letters*, vol. 107, no. 19, p. 195504, 2011.
- [204] D. Bansal, J. Hong, C. W. Li, A. F. May, W. Porter, M. Y. Hu, D. L. Abernathy and O. Delaire, "Phonon anharmonicity and negative thermal expansion in SnSe," *Physical Review B*, vol. 94, no. 5, p. 054307, 2016.
- [205] M. Keshavarz, M. Ottesen, S. Wiedmann, M. Wharmby, R. Küchler, H. Yuan, E. Debroye, J. A. Steele, J. Martens, N. E. Hussey, M. Bremholm, M. B. J.

- Roeffaers and J. Hofkens, "Tracking Structural Phase Transitions in Lead-Halide Perovskites by Means of Thermal Expansion," *Advanced Materials*, vol. 31, no. 24, p. 1900521, 2019.
- [206] K. Takenaka, "Progress of research in negative thermal expansion materials: paradigm shift in the control of thermal expansion," *Frontiers in chemistry*, vol. 6, p. 267, 2018.
- [207] D. a. J. H. Marx, *Ab initio molecular dynamics: basic theory and advanced methods*, Cambridge University Press, 2009.
- [208] C. H. Lui, Z. Li, Z. Chen, P. V. Klimov, L. E. Brus and T. F. Heinz, "Imaging stacking order in few-layer graphene," *Nano letters*, vol. 11, no. 1, pp. 164-169, 2010.
- [209] C. Cong, T. Yu, R. Saito, G. F. Dresselhaus and M. S. Dresselhaus, "Second-order overtone and combination Raman modes of graphene layers in the range of 1690– 2150  $\text{cm}^{-1}$ ," *Acs Nano*, vol. 5, no. 3, pp. 1600-1605, 2011.
- [210] X. Luo, X. Lu, C. Cong, T. Yu, Q. Xiong and S. Y. Quek, "Stacking sequence determines Raman intensities of observed interlayer shear modes in 2D layered materials—A general bond polarizability model," *Scientific reports*, vol. 5, p. 14565, 2015.
- [211] Y. Hong, J. Zhang and X. C. Zeng, "Thermal Conductivity of Monolayer  $\text{MoSe}_2$  and  $\text{MoS}_2$ ," *The Journal of Physical Chemistry C*, vol. 120, no. 45, pp. 26067-26075, 2016.

- [212] A. T. Costa, M. S. Ferreira, T. Hallam, G. S. Duesberg and A. C. Neto, "Origami-based spintronics in graphene," EPL (Europhysics Letters), vol. 104, no. 4, p. 47001, 2013.
- [213] J. Cho, M. D. Keung, N. Verellen, L. Lagae, V. V. Moshchalkov, P. V. Dorpe and D. H. Gracias, "Nanoscale origami for 3D optics," Small, vol. 7, no. 14, pp. 1943-1948, 2011.